Platinum Group Metal-Free Catalyst and Catalyst Layer Design for PEM Fuel Cells

by

Pan Xu

A thesis

presented to the University of Waterloo

in fulfillment of the

thesis requirement for the degree of

Doctor of Philosophy

in

Chemical Engineering

Waterloo, Ontario, Canada, 2019

Examining Committee Membership

The following served on the Examining Committee for this thesis. The decision of the Examining Committee is by majority vote.

External Examiner   Dr. Yuyan Shao

                                                Senior Scientist, Technical Team Lead

Supervisor   Dr. Zhongwei Chen

                                                Professor

Internal Member   Dr. Qinqin Zhu

                                                Assistant Professor

Internal Member   Dr. Ali Elkamel

                                                Professor

Internal-external Member   Dr. Zhongchao Tan

                                                Professor

Author's Declaration

This thesis consists of material all of which I authored or co-authored: see Statement of Contributions included in the thesis. This is a true copy of the thesis, including any required final revisions, as accepted by my examiners.

I understand that my thesis may be made electronically available to the public.

Statement of Contributions

The body of this thesis is based upon a combination of published work and work drafted for submission. Various chapters are adapted from the following list.

Chapter 3 of this thesis consists of a paper that was co-authored by myself, my supervisor, five post-doctoral fellows, Drs. J. Zhang, G. Jiang, F. Hassan, J. Choi, X. Fu, one PhD student, P. Zamani, and three collaborators, Drs. L. Yang, D. Banham and S. Ye. My supervisor, Dr. Z. Chen, directed the research. Dr. J. Zhang and I designed the experiment. I carried out the experiment, collected and analyzed the data, as well as the writing of the manuscript. Drs. G. Jiang, X. Fu and P. Zamani assisted with material synthesis. Drs. L. Yang, D. Banham, S. Ye and J. Choi assisted with battery and fuel cell testing. Dr. F. Hassan assisted with the writing of the manuscript. All authors reviewed the manuscript.

"Embellished hollow spherical catalyst boosting activity and durability for oxygen reduction reaction", Nano Energy, 2018, 51, 745.

Chapter 4 of this thesis consists of a work that was contributed by myself, my supervisor, three post-doctoral fellows, Drs. J. Zhang, J. Zhu and X. Fu, and two collaborators, Drs. J. Choi and A. Yong. My supervisor, Dr. Z. Chen, directed the research. Dr. J. Zhang and I designed the experiment. I carried out the experiment, collected and analyzed the data, as well as the writing of the manuscript. Drs. J. Zhu and X. Fu assisted with material synthesis. Drs. J. Choi and A. Yong assisted with fuel cell testing. All authors reviewed the manuscript.

Chapter 5 of this thesis consists of a work that was contributed by myself, my supervisor, one post-doctoral fellow, Dr. J. Zhang, and three collaborators, Drs. J. Choi, Y. Zhou and A. Yong. My supervisor, Dr. Z. Chen, directed the research. Dr. J. Zhang and I designed the experiment. I carried out the experiment, collected and analyzed the data, as well as the writing of the manuscript. Drs. J. Choi, Y. Zhou and A. Yong assisted with fuel cell testing. All authors reviewed the manuscript.

Abstract

Facing the crises of energy shortage and climate change, it becomes increasingly urgent to find renewable and low carbon emission replacements for fossil fuels. Renewable energy such as wind power, hydropower, solar energy, geothermal energy, and bioenergy has been applied as power sources, mostly converted to electric power. In the area of transportation, gasoline and diesel are still the most widely used fuels, which are eco-unfriendly because of CO_2, SO_X and NO_X emissions as the exhaust. In order to electrify the transportation process, electric power needs to be stored within appropriate media in the form of chemical energy, which must be able to easily transfer to electricity to power cars, buses, trains, cruises, airplanes, and other transportation modes. Lithium and hydrogen are the most promising candidates for transportation applications as the energy carrier, which puts the lithium-ion battery and hydrogen fuel cell into the dominance in the market. Restricted by the energy density of the lithium-ion battery, the driving range of a battery electric vehicle (BEV) is very limited. Comparing to BEV, Fuel cell electric vehicle (FCEV) has a much higher driving range benefit from the high energy density of compressed hydrogen.

There are challenges that FCEVs are confronting as well, among which the high cost of PEM fuel cell is one of the biggest challenges. The major reason that makes proton exchange membrane (PEM) fuel cell expensive is the platinum used to catalyze the anode and cathode reactions, mainly the cathode. The primary goal of the works for this thesis is to prepare catalysts that are: (1) highly active; (2) durable; (3) cost-effective; (4) scalable. The catalysts prepared will not only be tested in the "half-cell" simulated by the three-electrode system to verify their oxygen reduction reaction activity, but also be incorporated to the PEM fuel cell to see their performance in real applications. In the first work of this thesis, we prepared an ultra-high surface area hollow

carbon sphere as the carbon support. By using the aminothiophenol as the N, S co-doping precursor, the hollow sphere structure was successfully retained in the final catalyst HCS-A, which also has a high surface area. HCS-A was also found to have high activity, especially in the alkaline medium. In the second work of this thesis, the heteroatom doping is restricted with nitrogen. However, we applied a secondary nitrogen doping precursor to enhance the nitrogen doping and boost the oxygen reduction reaction (ORR) activity. In order to meet the requirements for larger-scale applications, we have successfully scaled up the catalyst from milligram-scale to gram-scale, without any diminishment in the ORR activity. The scale-up catalyst with secondary nitrogen doping SU-PAU has demonstrated the state of art half-cell activity and PEM fuel cell performance. The last work of this thesis focuses on operating condition study and membrane electrode assembly (MEA) design optimization. Through a systematic study, we were able to obtain in-depth knowledge of how the operating parameters and design parameters may affect the performance. After careful optimization, the highest H_2-air performance to date was achieved with a commercial size MEA.

Acknowledgments

I would like to thank my advisor Professor Zhongwei Chen who gave me the opportunity to pursue my Ph.D. degree, and who guided and encouraged me throughout my Ph.D. studies. He gave me the freedom to pursue various research ideas; without his support, I would never have accomplished so much. Also, I want to thank my Ph.D. thesis examining committee, including Professor Yuyan Shao as my external examiner from Pacific Northwest National Laboratory, Professor Zhongchao Tan, Professor Ali Elkamel, and Professor Qinqin Zhu from the University of Waterloo for their time and contributions through this important process. I would also like to thank Professor Zhongchao Tan for his participation in my comprehensive proposal examining committee.

I would like to thank my colleagues at the University of Waterloo, especially those who have worked on oxygen reduction reaction catalyst and PEM fuel cells with me. The knowledge and ideas we shared and exchanged at the healthy and encouraging atmosphere give me hints to tackle challenges from the projects.

I would like to thank my colleagues at Ballard Power Systems: my supervisor Ja-Yeon Choi and Lijun Yang, my manager Alan Young, R&D department director Shanna Knights, and all the other colleagues that I have been and will be working with. I deeply appreciate the mentorship, scientific knowledge and mental support I was given throughout my last year of Ph.D. studies.

Moreover, I would like to express my gratitude to my friends, my parents, and my wife for their unconditional support and encouragement. Dedicated to my parents, my wife, and my son for their love and caring.

Table of Contents

List of Figures

List of Tables

List of Abbreviations

Accelerated degradation test (ADT)

Aminothiophenol (ATP)

Ammonium persulfate (APS)

Area-specific resistance (ASR)

Battery electric vehicle (BEV)

Beginning of life (BOL)

Beginning of test (BOT)

Brunauer-Emmett-Teller (BET)

Carbon nanotube (CNT)

Catalyst coated membrane (CCM)

Cathode catalyst layer (CCL)

Direct methanol fuel cell (DMFC)

Double-layer capacitance (DLC)

Electrochemical impedance spectroscopy (EIS)

End of test (EOT)

Energy dispersive X-ray (EDX)

Equivalent weight (EW)

Fuel cell electric vehicle (FCEV)

Gas diffusion layers (GDL)

High-frequency resistance (HFR)

Hollow carbon spheres (HCS)

Hydrogen oxidation reaction (HOR)

Internal combustion engine (ICE)

Linear sweep voltammetry (LSV)

Membrane electrode assembly (MEA)

Microporous layer (MPL)

Molten carbonate fuel cell (MCFC)

Oxygen reduction reaction (ORR)

Phosphoric acid fuel cell (PAFC)

Platinum group metal (PGM)

Poly(aminothiophenol) (PATP)

Proton exchange membrane (PEM)

Proton-exchange membrane fuel cell (PEMFC)

Reactive oxygen species (ROS)

Relative humidity (RH)

Reversible hydrogen electrode (RHE)

Rotating disk electrode (RDE)

Rotating ring disk electrode (RRDE)

Scanning electron microscopy (SEM)

Solid oxide fuel cell (SOFC)

Standard hydrogen electrode (SHE)

Transmission electron microscopy (TEM)

Triple-phase boundarie (TPB)

X-ray diffraction (XRD)

X-ray photoelectron spectroscopy (XPS)

Chapter 1 Introduction

1.1 Motivation

The world has witnessed rapid growth in energy consumption and raising awareness of the global warming issue. Sustainable and environmentally friendly energy technology is attracting the attention of the government, industry, and academia. The world's primary energy consumption is expected to increase by 39% from 2011 to 2030[1, 2]. Besides, studies have indicated that the reserve for fossil fuel, like crude oil and gas, will be exhausted within the next 50 years.[3, 4] Different types of technologies, such as lithium batteries, metal-air batteries, flow batteries, and et al. have been developed to address the twin challenges of energy crisis and global warming. The fuel cell has been regarded as one of the most promising renewable energy technologies to resolve global energy issues. The fuel cells can be divided into several types, such as solid oxide fuel cell (SOFC), Molten carbonate fuel cell (MCFC), Phosphoric acid fuel cell (PAFC), Proton-exchange membrane fuel cells (PEMFCs) and so on.[5, 6] The division is based on the electrolyte that is used for the ion conduction between the anode and cathode. The application of these fuel cells varies from each other because the operation conditions, fuel types and power output capability are different. The SOFC and MCFC are mostly applied for large scale applications such as power plants, backup power for industry, marine and so on.[7] Proton exchange membrane (PEM) fuel cells are mostly used for transportation applications, such as vehicles, trucks, buses, trains, and forklifts, and becoming increasingly popular benefits from its high energy conversion efficiency, high power density, and environmental benignity.[8, 9] PEM fuel cells are increasingly attracting attention because fuel cell electric vehicle (FCEV) is becoming popular as a substitute for internal combustion engine vehicle. Even though there are many advantages, the cost of existing PEM fuel cells is still very high due to the component materials that are essential. A large part of the fuel

cell stack cost comes from the catalysts,[10, 11] which present at each electrode to facilitate the electrochemical reactions. By scaling up the production of fuel cells, the cost of other components is possible to be significantly reduced. However, the cost of Pt would likely to increase because of the limited reserve of platinum in the earth. The high cost and limited reserve of Pt have been one of the major barriers hindering the large-scale commercialization of fuel cells.[12-15]

Compared to the hydrogen oxidation reaction (HOR) at the anode, the oxygen reduction reaction at the cathode is known to be prone to high overpotential and slow reaction kinetics.[16-18] The platinum loading at the cathode is normally five times higher than that of the anode to facilitate the cathode reaction. Hence research efforts have been focusing on reducing or even eliminating the platinum at the cathode of the PEM fuel cell. Two approaches have widely been proposed to rectify the issue regarding the cost of the cathode catalyst: (1) increase the utilization or effectiveness of platinum catalysts to reduce the platinum loading, or (2) completely replace platinum catalysts with platinum group metal-free (PGM-free) catalysts.[19-22]

The second approach to completely replace platinum with PGM-free catalysts is far more desirable for the long term consideration, as the first approach does not fully address the issue of the limited world supply of platinum. Since the evolution of this type of catalyst began in 1964 by Jasinski, several breakthroughs have led to significant advances in the activity of PGM-free catalysts, boosting its potential from a scientific curiosity to a commercially viable option.[23-26] Start with Jasinski's work, macrocyclic compounds that contain metal-N_x chelate was initially proven to be ORR active. Later on, the pyrolyzed non-macrocyclic material demonstrated high activity towards ORR, greatly broaden the selectivity of nitrogen-containing precursors.[27-29] Since the precursors shifted from macrocyclic material to non-macrocyclic material, many varieties of nitrogen precursors have emerged in recent years,[30-33] as well as other types of heteroatom (boron,

2

sulfur, phosphorus, etc.) doping and dual doping precursors.[34-37] Another heteroatom was found to be able to modify the electron density of the iron center, thus affect the oxophilicity of the active sites, as well as the overall oxygen reduction reaction (ORR) activity.

Bringing in another heteroatom can be beneficial, but it is also risky sometimes because it is possible to decrease the catalytic activity as the mechanism of the secondary doping effect is still vague. Another way to enhance the catalyst is to introduce an additional nitrogen precursor to achieve dual nitrogen-doped in the catalyst. Fu et al.[38] used polyaniline and phenanthroline as dual nitrogen sources and obtained an abundance of 3D porous graphene-like structures. The unique structure could host a high population of reactant-accessible active sites for the ORR and facilitate mass transport as well. In another work,[39] they used polyaniline and NH_4Cl as the dual nitrogen precursor and found the NH_4Cl assisted the formation of both $Fe-N_4$ sites and porosity. It was found that the edges that are created by the NH_4Cl boost the ORR activity. Leonard and coworkers[40] used cyanamide, melamine, urea, and nicarbazin as the secondary nitrogen precursors, and demonstrated that the intrinsic activity of active site and the utilization of the active site compensate each other. The additional doping of nitrogen not only increases the population of active sites but also enhances the intrinsic activity of each site.

The goal for catalyst synthesis is not just running half-cell testings with these catalysts. Instead, they have to demonstrate good performance in the membrane electrode assembly to prove their capability to boost fuel cell performance. Unlike the half-cell, the full cell is much more complicated because there are more processes involved in the fuel cell reactions. Aside from the activity of the catalyst, there are other factors that have unneglectable impacts on the performance, such as proton transfer and mass transport issues.[41-44] For PGM-free catalysts, these issues become more critical because the catalyst loading for PGM-free catalysts are generally much higher than

Pt-based catalysts, leading to thicker catalyst layer and poorer transportability for both protons and oxygen.

In this thesis, the first work focuses on the synthesis of PGM-free catalysts with unique structure by nitrogen and sulfur co-doping. In the second work, we prepared a dual doped nitrogen catalyst and successfully scaled-up the catalyst. In the last work, we have done systematic optimization of the fuel cell performance and catalyst layer design optimization to achieve the best performance based on the PGM-free catalyst that is discussed in the second work.

1.2 Proton-exchange Membrane Fuel Cell (PEMFC) Working Mechanism

1.2.1 General overview

PEM fuel cell is a type of energy conversation system that converts chemical energy directly to electrical energy. Just like a battery, the fuel cell generates electrical energy relying on electrochemical reactions at both electrodes of the "cell": anode and cathode. However, the reactants, fuel, and oxidant at both electrodes in a fuel cell are not reserved in the "cell"; instead, they are continuously supplied from the external supply system. From this perspective, it is more of a "chemical factory" that consumes raw material and produces the final product, but itself is not consumed while working. The oxidant at the cathode side of a PEM fuel cell can be either pure oxygen or air, which contains 21% oxygen in it. The fuel at the anode side of a PEM fuel cell has a variety of choices such as hydrogen, methanol, ethanol, and ammonia. Among these fuels, hydrogen is optimal for not only PEM fuel cells but all types of fuel cells.

A typical operation mechanism of a hydrogen-oxygen fuel cell is illustrated in Figure 1-1. The anode half-cell reaction is hydrogen oxidation, described as Equation 1.1:

$$H_2 \leftrightarrow 2H^+ + 2e^- \qquad\qquad E^0 = 0 \text{ V vs. RHE} \qquad (1.1)$$

E^0 is the standard reversible potential of the reaction, and also the standard half-cell potential. Hydrogen gas molecule disassociates to become two protons, in the meantime, two electrons escape from hydrogen. The electrons travel from anode to cathode through the external circuit whereas the protons migrate through the polymer electrolyte membrane to the same destination. After protons and electrons reach the cathode, they react with the oxygen gas molecule to form water, following cathode half-cell reaction as Equation 1.2:

$$2H^+ + \tfrac{1}{2}O_2 + 2e^- \leftrightarrow H_2O \qquad\qquad E^0 = 1.229 \text{ V vs. RHE} \quad (1.2)$$

A combination of the two half-reactions give the overall reaction in Equation 1.3:

$$2H^+ + \tfrac{1}{2}O_2 \leftrightarrow H_2O + heat \qquad\qquad E^0 = 1.229 \text{ V} \qquad (1.3)$$

If hydrogen is applied as the fuel of a fuel cell, the only emission of this technique will be water and heat. If widely applied for stationary, transportation and portable devices, the fuel cell can greatly reduce the global greenhouse gas and pollutant emissions.
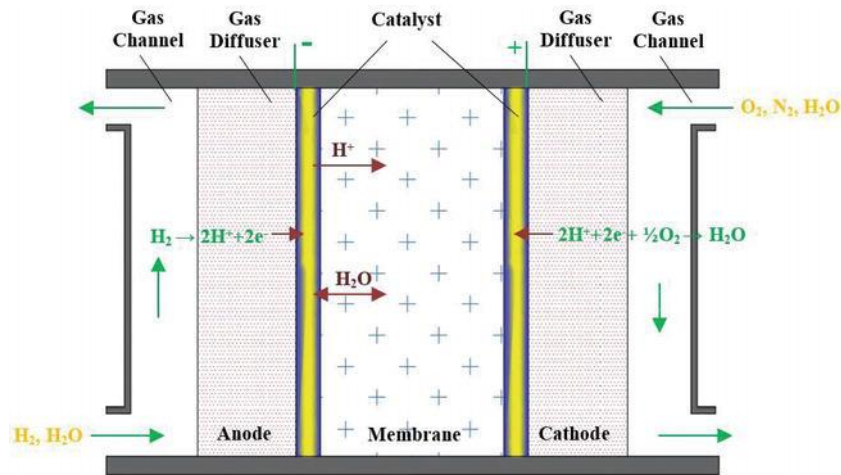
Figure 1- 1. A typical operation mechanism of a hydrogen-oxygen fuel cell.

1.2.2 PEM fuel cell fuel efficiency

Based on the thermodynamics of the overall cell reaction, maximum electrical work available from a fuel cell is limited by ΔG, which also limits the ideal efficiency of a fuel cell. The efficiency (ε) of an energy conversion process can be expressed as:

$$\varepsilon = \frac{useful\ energy}{total\ energy} \tag{1.4}$$

For a fuel cell that extracts work from a chemical reaction, the thermal efficiency is:

$$\varepsilon = \frac{\Delta G}{\Delta H} \tag{1.5}$$

In which ΔH is the total energy change between the reactants and the product. At standard condition, the H_2-O_2 fuel cell has $\Delta G^0 = -237.17 KJ/mol$ and $\Delta H^0 = -285.83 KJ/mol$, resulting in an ideal thermal efficiency of:

$$\varepsilon_{thermo} = \frac{-237.17}{-285.83} = 0.83 \tag{1.6}$$

This is fairly impressive in contrast to an internal combustion engine which is limited by the Carnot cycle. Note that both ΔG and ΔH are dependent on temperature and pressure. If not at standard condition, ε_{thermo} will change accordingly.

In reality, fuel efficiency is always lower than the ideal efficiency because of extra voltage losses and fuel utilization losses during operation. The real efficiency for a fuel cell can be calculated as:

$$\varepsilon_{real} = (\varepsilon_{thermo}) \times (\varepsilon_{voltage}) \times (\varepsilon_{fuel}) \tag{1.7}$$

The voltage efficiency $\varepsilon_{voltage}$ is determined by kinetic loss, ohmic loss and mass transport loss (will be discussed in the next section) that can be captured in the i-V polarization curve. $\varepsilon_{voltage}$ is the ratio of the operating voltage (V) over thermodynamically reversible voltage (E).

$$\varepsilon_{voltage} = \frac{V}{E} \tag{1.8}$$

Based on a polarization curve, the operating voltage is always dependent on the current drawn from the fuel cell. With the current goes higher, the losses increase and the voltage becomes lower. For this reason, fuel cells are more efficient at low load region and less efficient at high load region.

The fuel utilization efficiency ε_{fuel} describes the level of fuel utilization. Some of the fuel supplied to the fuel cell flow through the system and discharged before been reacted. Some of the fuel participates in side-reactions that are not beneficial to power output. ε_{fuel} is the ratio of the fuel that has been utilized to generate electric current versus the total fuel supplied to the fuel cell.

$$\varepsilon_{fuel} = \frac{i/nF}{\upsilon_{fuel}} \tag{1.9}$$

In which i (A) is the current generated from the fuel cell, and υ_{fuel} (mol/s) is the fuel supply rate. An overflow of fuel can cause low efficiency of fuel utilization. Fuel cells are typically operated in a constant flowrate mode or a constant stoichiometry mode. In the former mode, a constant rate of fuel is supplied to the fuel cell regardless of how much fuel is needed at a certain operating load. Sufficient fuel is generally provided to ensure fuel starvation doesn't happen at the maximum load. However, a large amount of fuel will be wasted at lower loads. The fuel can be also supplied as constant stoichiometry, in which manner the fuel can be supplied according to the load applied to the fuel cell. The fuel is typically provided slightly more than what would be required to ensure sufficient fuel supply.

1.2.3 PEM fuel cell voltage losses

Thermodynamic ideal potential (E): As discussed in the previous section, the voltage efficiency $\varepsilon_{voltage}$ is determined by kinetic loss, ohmic loss and mass transport loss. In order to better understand the voltage losses of a fuel cell, it would be helpful to study from an i-V polarization curve (Figure 1-2).

In Figure 1.2, the blue dot line represents the thermodynamic ideal potential (Nernst potential) that can be calculated from ΔG through the Nernst equation. Under standard condition, $\Delta G^0 = -237.17 KJ/mol$.

$$E^0 = \frac{\Delta G^0}{nF} = \frac{-237170\ J/mol}{2 \times 96485\ C/mol} = 1.229\ V \tag{1.10}$$

Under nonstandard conditions, ΔG can be calculated from the ΔG^0 trough equation:

$$\Delta G = \Delta G^0 + RT\ ln\ Q \tag{1.11}$$

Where R is the ideal gas constant 8.314 J/mol K, T is the temperature in Kelvin, and Q is the reaction quotient. For a reaction $a\text{A} + b\text{B} = c\text{C} + d\text{D}$, Q is calculated from equation 1.9:

$$Q_{gas} = \frac{(P_C)^c(P_D)^d}{(P_A)^a(P_B)^b}\ \ or\ \ Q_{solute} = \frac{[C]^c[D]^d}{[A]^a[B]^b} \tag{1.12}$$

From equation 1.11 and 1.12, ΔG can be affected by temperature, pressure, and concentration. Because the thermodynamic ideal potential (E) is determined by ΔG, it also differs according to different temperatures, pressures, and concentrations.
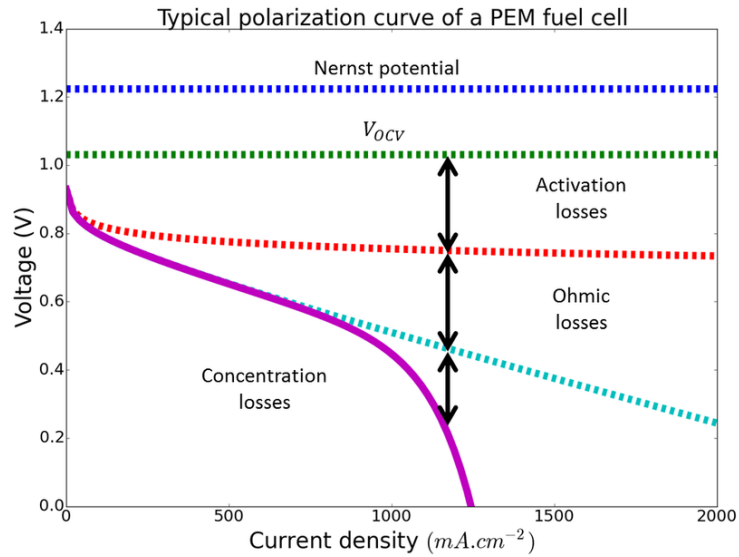
Figure 1- 2. Typical PEMFC polarization curve.

Kinetic loss: Due to the voltage losses, the operation cell voltage (V) is always lower than thermodynamic ideal potential (E), and voltage drops with the increment of current density. At low current density region, activation overpotential (η_{act}) also known as the kinetic loss is the dominant cause for voltage loss. The red dot line represents the cell voltage after considering activation overpotential. Kinetic loss is related to the reaction kinetics. For example, the reduction reaction at the fuel cell cathode side is thermal dynamical favorable (ΔG < 0), however, the reaction is super slow at the equilibrium potential. An energy barrier called activation energy hinders the reaction form move forward, thus there must be overpotential to drive the reaction faster.

Butler-Volmer (B-V) equation nicely describes the relationship between reaction current and overpotential:

$$j = j_0(e^{\frac{\alpha nF\eta}{RT}} - e^{-\frac{(1-\alpha)nF\eta}{RT}})$$ (1.13)

Where j_0 is the exchange current density at a "standard concentration". α is the transfer coefficient. The value of α is always between 0 and 1. For "symmetric" reactions, $\alpha = 0.5$. For most electrochemical reactions, α ranges from about 0.2 to 0.5. n is the number of electrons transferred in the electrochemical reaction. F is the faradic constant. η is the activation overpotential. From Butler–Volmer we know that if more electricity needs to be drawn from a fuel cell, the price of voltage loss must be paid.

Butler–Volmer equation is often considered unwieldy when dealing with fuel cell reaction kinetics. It can be simplified through reasonable approximations. The two simplifications apply when activation overpotential (η_{act}) is either very small (<15 mV, $j \ll j_0$) or very large (>50 mV, $j \gg j_0$).

When η_{act} is very small, a Taylor series expansion ($e^x = 1+x$ for small x) of the exponential term produces

$$j = j_0 \frac{nF\eta}{RT}$$ (1.14)

The equation tells that for small deviation from equilibrium, the current and overpotential are linearly related. Theoretically, j_0 can be calculated from the slope of j versus η (η_{act}). However, when j is too small, it is most likely to be covered by impurity currents or measurement noise. Instead, j_0 is usually obtained from a higher overpotential region.

When η_{act} is large, the second exponential term in the B-V equation is neglectable. This also represents that the backward reaction rate is neglectable comparing to forward reaction. The B-V equation can be simplified to

$$j = j_0 e^{\frac{\alpha n F \eta}{RT}} \tag{1.15}$$

Solving the equation for η yields

$$\eta = -\frac{RT}{\alpha n F} \ln j_0 + \frac{RT}{\alpha n F} \ln j \tag{1.16}$$

In equation 1.15, R, T, n, and F are either constant or measurable value. Both α and j_0 are possible to be determined by fitting η versus ln j or log j. The fit should persist for at least one order of magnitude for reliable results. This equation is also known as the Tafel equation in the form of

$$\eta = a + b \log j \tag{1.17}$$

After approximation of the B-V equation, we are able to get a more simplified form (Tafel equation) to describe the relationship between activation overpotential and current density. Tafel equation is a powerful tool to extract the part of kinetic loss within the total losses from a polarization curve.

Ohmic loss: As shown in Figure 1.2, there is a linear region in the polarization curve when the current density becomes higher. This region is known as the ohmic polarization region, where the ohmic loss becomes more significant. It should be kept in mind that the kinetic loss also grows, and it is still a big part of total voltage loss in the ohmic polarization region. Ohmic loss is due to the ohmic resistance in the movement of charged particles including both electrons and protons. More specifically, it includes cell electric resistance, membrane resistance, and catalyst layer

ionomer resistance. In a single cell, nitrogen-doped resistance includes the resistance in bipolar plates, gas diffusion layers (GDL), connection wires and all the other components that electrons have to pass through. Membrane resistance and catalyst layer ionomer resistance are both proton transfer resistance.

Because the current produced in a fuel cell flows serially through all the components, the total ohmic resistance is actually the sum of all the individual resistance from each component and the connections between these components. Unfortunately, even though it is possible to measure the total resistance, it is experimentally very difficult to resolve the individual resistance of the various sources.

Because the movability of proton in the membrane or ionomer is much slower compared to the movability of electrons in metals and carbon materials, the ionic resistance usually is the dominant party in a fuel cell. For instance, the conductivity of a Nafion membrane can be up to 0.2 $S \cdot cm^{-1}$ depending on temperature and hydration state.[45] At a membrane thickness of 20 μm, the area-specific resistance (ASR) is 0.01 $\Omega \cdot cm^2$. On the other hand, a 20 μm thick carbon cloth electrode would have an ASR of less than 2×10^{-6} $\Omega \cdot cm^2$. This clearly shows ionic resistance from the membrane and catalyst layer dominates the overall fuel cell resistance.

Mass transport loss: This type of loss is also called concentration loss, defined as the loss in performance of the fuel cell due to limitations in mass transport processes. It occurs mostly when the cell is producing a large current, where the reactants can't be supplied efficiently and a drop appears in output-voltage as a result. In a PEM fuel cell, mass transport includes hydrogen transport at the anode, oxygen transport at the cathode, water transport, and other reaction intermediate product transport. Compared to hydrogen, oxygen transport is more sluggish (also more sluggish in reaction), because oxygen molecule has a bigger size than hydrogen, besides,

oxygen is often supplied by air which contents only 21% of oxygen. When talking about mass transport issues, we mostly refer to the oxygen transport issue.

There are generally two forms of mass transport in a fuel cell – convection and diffusion. The former refers to species transported by bulk motion of the fluid. The latter refers to species transported due to the concentration gradient. Convection transport in a fuel cell is driven by gas pressure that pushes gas to move. Anode and cathode gases travel through gas supplying system and fuel cell flow channels with a certain flow rate. When they come to the electrodes, convection transport no more applies because of the high porosity of the electrodes. The electrodes, which have many micrometer-scale and nanometer-scale poles, are the final destination of hydrogen gas and oxygen gas. Within the electrodes, diffusion becomes the dominant way for gas transport. Compare to convection, diffusion has much less gas transport efficiency; thus oxygen diffusion problem causes the mass transport voltage drop at high current density.

Water is generated constantly when a fuel cell is working. Because water is generated in the liquid phase under the PEMFC operation temperature, it can cause flooding issues if not managed well. It must be effectively removed from the system during operation, to prevent it from blocking the gas transport channels. Severe flooding can bring a rapid voltage drop in the polarization curve. Water management is another topic, and most problems that arise from water management are also related to oxygen transport.

Mixed potential loss: If look back to Figure 1.2, it can be found that there is still a portion of the loss between the blue and green dot lines not been discussed yet. This portion of the loss was often attributed to kinetic loss and rarely been studied in previous researches. This part of potential loss is caused by parasitic reactions that introduce mixed potential. The most popular

explanation is the hydrogen crossover and its reaction with oxygen resulting in mixed potential. Another explanation is that the catalyst surface oxidation can result in a mixed potential.[46]

From equation 1.2 in section 1.2.1, we know fully oxygen reduction to water has a standard reaction potential of 1.229 V. However, if oxygen is not fully reduced to water, it can produce H_2O_2 as a by-product and the reaction potential is much lower:

$$2H^+ + O_2 + 2e^- \leftrightarrow H_2O_2 \qquad E^0 = 0.7 \text{ V vs. RHE} \qquad (1.18)$$

The third explanation is that the incomplete reduction of oxygen to hydrogen peroxide resulting in the mixed potential that is lower than 1.229V under standard condition.[47]

1.3 Catalysis of the oxygen reduction reaction

As we discussed in section 1.2.3, the fuel cell suffers from kinetic loss. The loss mainly comes from oxygen reduction reaction (ORR) at the cathode, because oxygen reduction is much more sluggish than hydrogen oxidation. Oxygen reduction reaction has a slow reaction rate because it has an energy barrier to overcome, which is called activation energy. The reactant must overcome that barrier to an activated state in order to undergo the transition from reactant to product. The conversion rate of reactants to products depends on the probability of a reactant species in the activated state. The probability of finding one species in the activated state is exponentially dependent on the scale of activation energy:

$$P_{act} = e^{-\Delta G_1^{\ddagger}/(RT)} \qquad (1.19)$$

Where P_{act} is the probability of a reactant species in the activated state, $\Delta G_1^{\ddagger}$ is the activation energy of a reactant, R is the ideal gas constant and T is the temperature (K). From this probability, it is possible to describe the reaction rate as a statistical process:

$$J_1 = C_R^* \times f_1 \times P_{act} = C_R^* f_1 \, e^{-\Delta G_1^{\ddagger}/(RT)} \qquad\qquad (1.20)$$

Where J_1 is the forward reaction rate, C_R^* is the reactant surface concentration (mol/cm^2) and f_1 is the decay rate of the activated species to the product.

From equation 1.19 we know that the reaction rate is also exponentially dependent on activation energy. In order to boost the reaction, the catalyst can be applied to reduce the activation energy that is required to reach the activated state. Instead of directly reacts with proton, oxygen can be firstly bonded to the catalyst surface, resulting in weakened O-O bond. Thus, further reduction of oxygen and O-O bond-breaking becomes easier. One example of the catalysis process of ORR can be as follows:

$$* + O_2 \leftrightarrow * O_2 \qquad\qquad \text{Step 1}$$

$$* O_2 + H^+ + e^- \leftrightarrow * OOH \qquad\qquad \text{Step 2}$$

$$* OOH + H^+ + e^- \leftrightarrow * O + H_2O \qquad\qquad \text{Step 3}$$

$$* O + H^+ + e^- \leftrightarrow * OH \qquad\qquad \text{Step 4}$$

$$* OH + H^+ + e^- \leftrightarrow * + H_2O \qquad\qquad \text{Step 5}$$
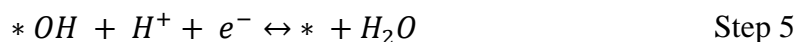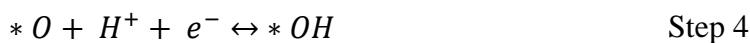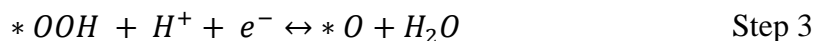
The symbol $*$ represents an active site. In this process, only one active site is involved in the reaction and the oxygen bond breaks after one water molecule is formed. In another possible reaction process, the oxygen bond breaks right after it is bonded to the active site. This process involves two active sites for two oxygen atoms in one oxygen molecule:

$$2 * + O_2 \leftrightarrow * OO * \qquad\qquad \text{Step 1}$$

$$* OO * \leftrightarrow 2 * O \qquad\qquad \text{Step 2}$$

$$2 * O + 2 H^+ + 2 e^- \leftrightarrow 2 * OH \qquad\qquad \text{Step 3}$$

$$2 * OH + 2 H^+ + 2 e^- \leftrightarrow 2 * + 2 H_2O \qquad\qquad \text{Step 4}$$
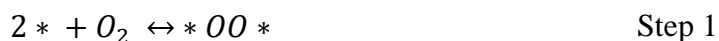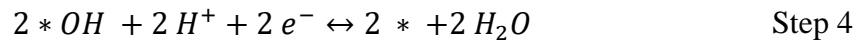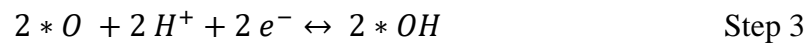
The full reaction of both examples is $O_2 + 4H^+ + 4e^- = 2H_2O$. These are just two simple examples of the catalyzed ORR process. In reality, the process can be more complicated, and there can be by-products like H_2O_2 generated from ORR.

1.4 Oxygen reduction reaction catalysts/catalyst layer

Since the sluggish oxygen reduction reaction needs to be catalyzed to reduce the kinetic loss, catalyst selection becomes a vital task for PEM fuel cells. There are several aspects to evaluate a catalyst, and the major requirements for a good catalyst include:

- High selectivity (low by-product yields)
- High catalytic activity (high j_0)
- High electrical conductivity
- High accessible surface area
- High active site density
- High mechanical strength
- Low corrosion
- Easy to manufacture

The most effective and popular catalysts for PEMFC are platinum and platinum-based alloys. More broadly to say, the Pt-based catalyst includes Pt, Pt alloy/dealloy, core-shell, shape-controlled nanocrystals, and nonoframes.[48] Pt black was firstly selected as the ORR catalyst at the

very early stage of fuel cell development. Thereafter, nano-sized Pt particles supported on carbon was employed, because Pt particles can be controlled to be much smaller with carbon support than without. To further enhance the catalyst activity and Pt utilization, varieties of other methodologies have been applied, such as alloy, core-shell, facet control, nanoframes and so on. For example, the first generation of Toyota Mirai PEMFC car uses PtCo alloy as the fuel cell catalyst.

The most challenging problems that Pt-based catalyst is facing are the high Pt price and limited Pt reserves on earth. That is the ultimate motivation for platinum group metal-free (PGM-free) catalyst development. Many types of PGM-free materials, such as transition metal oxide, transition metal sulfide, transition metal nitride, nitrogen-doped carbon and Fe-N/C material, have shown electrocatalytic activity toward ORR.

1.5 Fe-N/C ORR catalysts

1.5.1 Understand the active sites

Among the PGM-free ORR catalysts, Fe-N/C is the most promising one in terms of its high activity. Many of this category of materials was biologically inspired, such as iron phthalocyanine,[49-52] metalloenzymes,[53-55] and other enzymes.[56-58] Similar to the biological process, lab synthesized catalysts function as an intermediate that facilitates the oxygen reduction reaction without consuming itself. An intractable problem with the bio-inspired ORR catalyst is that they are not stable enough for long term applications. Later, it was found that after the pyrolysis of these catalysts, both the ORR activity and durability got improved.[59] It was then proposed that the transition metal center that coordinates to nitrogen in the nitrogen-doped carbon matrix is the active site for ORR. Other than that, researchers have also proposed different hypothesizes for the configuration of the active sites, but no consensus has been reached yet.

The most representative family of active sites of Fe-N/C catalysts was proposed by J.P. Dodelet et al. from the year 2002. They prepared several catalysts through heat treatment between 400 to 1000 °C, followed by surface analysis by ToF SIMs. It was found that one iron atom coordinates to two (Fe-N_2/C) or four nitrogen atoms (Fe-N_4/C) in carbon matrix are the active sites.[60] They also claimed that between these two types of active sites, Fe-N_2/C is the more abundant and more active one. In 2009, the same research group proposed that one iron atom bridging two graphite sheets with a Fe-N_{2+2}/C configuration is the active site (Figure 1-3 (a)).[61, 62] It was later proposed that the fifth nitrogen located at the vertical of the plan coordinates with the iron center and forms an N-Fe-N_{2+2}/C configuration, which acts as the active site.[63, 64] Zelenay and co-workers have directly visualized FeN_4 structure with aberration-corrected scanning transmission electron microscopy (Figure 1-3 (b)).[65]
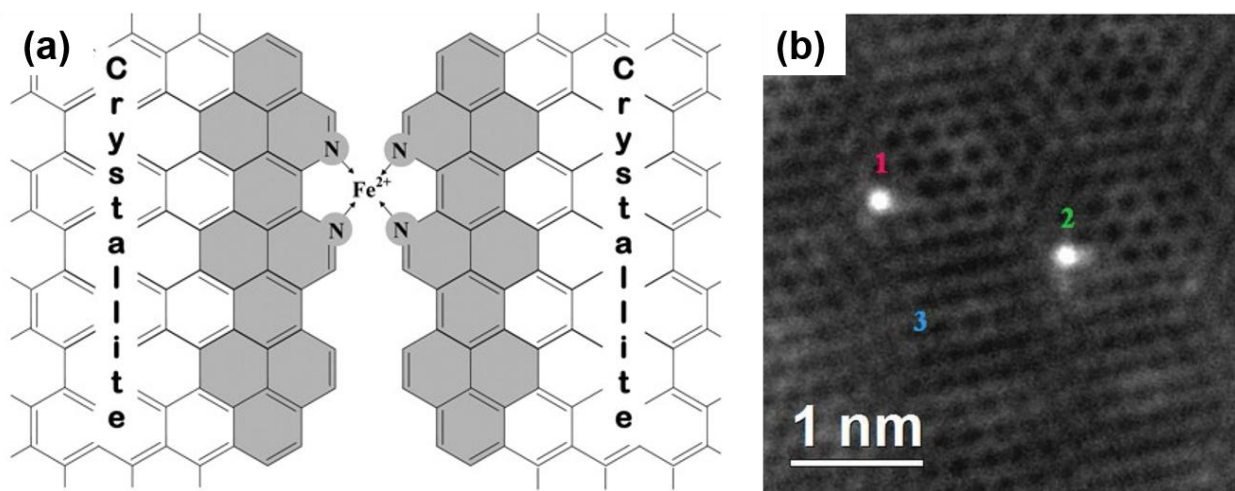
Figure 1- 3. (a) Plan view of the presumed catalytic site Fe-N_{2+2} and graphitic sheet growth (shaded aromatic cycles) between two crystallites; (b) HAADF-STEM image of individual Fe atoms in the active sites.

Besides iron-nitrogen coordination, there are some other types of active sites brought up by other groups. Bao and coworkers synthesized pea-pod like carbon nanotubes (CNTs) that encapsulates iron particles. In the active site, they proposed, iron was protected by a few layers of

CNTs to prevent it from the attacking of acids and oxidants. In the meantime, iron particles can provide electrons to the carbon shell, resulting in lower local work functions of the CNTs (Figure 1-4 (a)).[66] Sanjeev and his group proposed the synergistic effect between Fe-N$_4$/C sites and metallic iron particles. The synergistic effect happens in the way that the peroxide species formed on Fe-N$_4$/C sites can be further reduced to water on a second active site of metallic iron (Figure 1-4 (b)).[67] Li's Group proposed Fe$_3$C/C as the active site for ORR in both acidic and alkaline media. Similar to Bao's hypothesis, Fe$_3$C was also encapsulated in graphitic carbon shells, so that Fe$_3$C particle and carbon shell can synergistically catalyze the oxygen reduction (Figure 1-4 (c)).[68] Similar to the Fe-N$_4$/C model, Wu's group proposed dual-metal sites that Fe and Co adjacent to
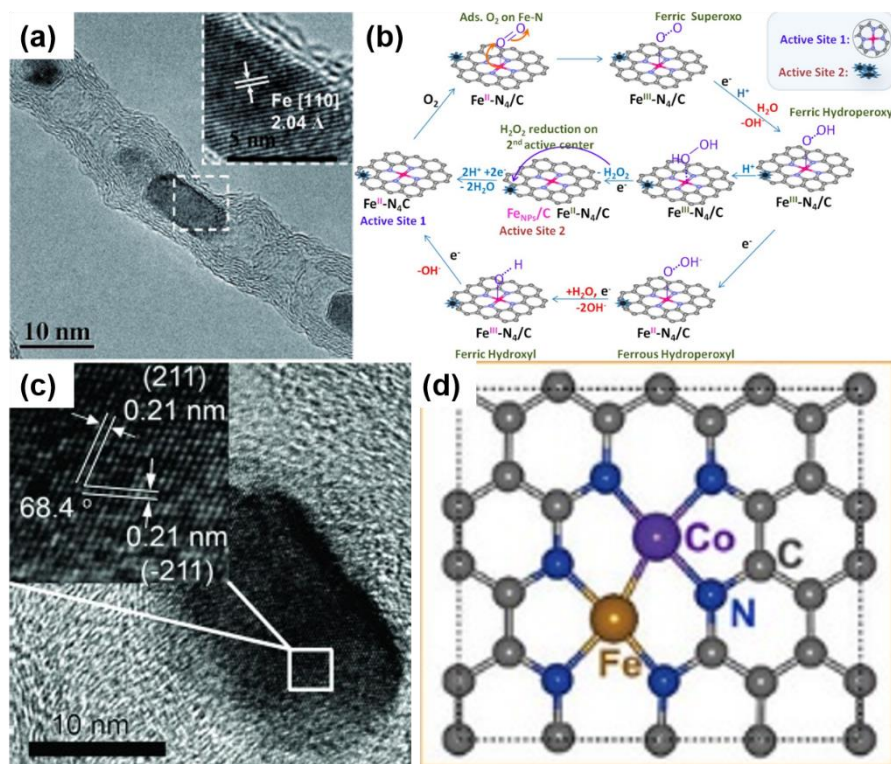
Figure 1- 4. (a) HRTEM image of Pod-Fe with the inset showing the [110] crystal plane of the Fe particle; (b) ORR mechanistic pathways on Fe-N$_4$/C and adjacent Fe nanoparticles; (c) HRTEM image of a Fe$_3$C nanoparticle and the index crystal plane shown in the inset; (d) Proposed architectures of Fe-Co dual sites.

each other are each bonded to three nitrogen atoms, leading to a (Fe, Co)-N_6/C active site (Figure 1-4 (d)).[69] The dual-metal active site was proved by both experiment and DFT calculation that it is more active than the single-metal active site, and it is comparable to commercial Pt/C. The dual-metal active site also proved excellent durability as it showed negligible degradation after100 hours of single-cell operation.

The above discussion just gives a few typical examples of the ORR active sites that have been proposed by researchers. It is impossible to summarize all types of active site hypothesis here, but the two broad categories (transition metal-nitrogen coordination and metallic particles) cover the vast majority of the hypothesis that has ever been proposed.

1.5.2 Catalyst degradation mechanisms

Since there are different understandings of PGM-free catalyst active sites, their degradation mechanisms have also been proposed differently. The metallic type of active site can be leached away due to the acidic medium and relatively high voltage. However, in some synthesis processes, the catalysts have been acid washed one or more times under harsh conditions until the crystalline metal species are totally removed from the surface of the catalyst. After acid washing, the atomic metal (Fe-N_X/C) is still remaining and is stable under acidic medium. Some other PGM-free catalysts are initially synthesized with atomic metal as the only species in the catalyst. Either after effective acid washing or initially synthesized as single-atom active sites, the atomic iron is stable under acidic medium. Still, these types of PGM-free catalysts suffer from poor stability and durability. The catalyst degradation mechanism can be divided into three categories: protonation,[70] demetallation,[71] and carbon oxidation.[72]

Protonation: Many studies have been performed to study the degradation mechanisms. The protonation mechanism for performance loss was described by Liu et al.[73] They proposed that

the lone pair of electrons on the pyridinic N can be protonated in the acidic environment. Once protonated, the pyridinic N become inactive towards the ORR, because it no longer possesses a lone pair of electrons to facilitate oxygen adsorption. This mechanism was used to explain the stability difference observed in the same work. Two PGM-free catalysts were synthesized in the same way but were heat-treated at different temperatures. Trough XPS spectra, it was shown that the PGM-free catalyst heat-treated at 800 °C (NMCC-800) has two types of ORR active sites (pyridinic N and graphitic N), while the PGM-free catalyst heat-treated at 1100 °C (NMCC-1100) has only one type of ORR active site (graphitic N). According to protonation mechanism, because the graphitic N does not possess any lone pair electrons, it cannot be protonated and deactivated. That explains why NMCC-1100 has higher stability than NMCC-800.

Electrochemical carbon oxidation: Surface oxide generation of catalyst in acidic electrolytes involves the general steps of the oxidation of carbon followed by hydrolysis and gasification of oxidized carbon to CO_2.[74-76] The detailed mechanism is not yet fully understood but is presumed to include parallel formation of surface and gaseous carbon oxides by disproportionate formation of oxygen functional groups. One proposed generic stepwise mechanism of surface oxide formation and CO_2 evolution is shown schematically by Borup et al.[74, 77, 78] as:

$$R\text{-}C_S\text{-}H \rightarrow R\text{-}C_S\text{-}OH \rightarrow R\text{-}CS=O \rightarrow R\text{-}C_S\text{-}OOH \rightarrow R\text{-}H + CO_2$$
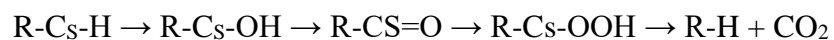
The incomplete carbon oxidation brings the oxygen-containing groups, such as hydroxyl, carboxyl, epoxy groups and et al, to the surface of carbon material. The incomplete oxidation might be able to recover through the electrochemical reduction process. However, if the carbon gets fully oxidized to carbon dioxide, it will cause physical corrosion and permanently damage the catalyst. The full oxidation is thermodynamically allowable at the potentials at which the ORR reaction takes place (equation 1.21).

$$C + H_2O \leftrightarrow CO_2 + 4H^+ + 4e^- \qquad\qquad E^0 = 0.207 \text{ V vs. RHE} \qquad (1.21)$$

Even though it is thermodynamically possible, the reaction is very slow and negligible under low potentials, because it is kinetically difficult due to the high reaction activation energy. That is why Pt-based catalysts can use carbon as its support material. At higher potentials, the oxidation/corrosion becomes more severe and catalysts can get damaged very quickly.

H_2O_2 (reactive oxygen species) induced carbon oxidation: We have discussed in section 1.3, that the incomplete reduction of ORR produces H_2O_2 as the by-product. Schulenburg et al. proposed that H_2O_2 can directly attack the N functionalities that coordinate with the transition metal active center.[79] H_2O_2 is also able to attack the surface carbon via Fenton reagent with the surface FeNxCy moieties. As a well-understood mechanism, Fe^{2+} and Fe^{3+} promote the H_2O_2 to split into highly reactive free radicals:

$$Fe^{2+} + H_2O_2 \leftrightarrow Fe^{3+} + HO\cdot + OH^- \qquad\qquad (1.22)$$

$$Fe^{3+} + H_2O_2 \leftrightarrow Fe^{2+} + HOO\cdot + H^+ \qquad\qquad (1.23)$$
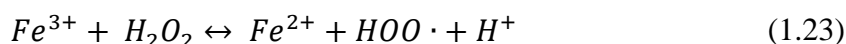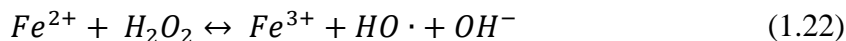
Comparing to the carboxyl radical, the hydroxyl radical is much more powerful and poses more threat to the catalyst. It should be mentioned that free radicals also attack ionomer and membrane, but we won't be discussing ionomer and membrane, because the catalyst is the only focus of our discussion here. It was reported that the radicals keep the iron center untouched, instead, it oxidizes the carbon.[72] Similar to electrochemical oxidation, the reactive oxygen species (ROS) can oxidize the surface carbon to C-OH, C=O, and C-OOH. The oxidation can be more severe, that the ROS is able to fully oxidize the surface carbon CO_2 and physically corrode the catalyst. In the latter case, if the carbon is bonded to an active site, the site will be destroyed. Even if in the former case

that carbon is incompletely oxidized, oxygen-containing groups on carbon surface not only decreasing iron oxophilicity but also deplete the carbon support of p-electrons, thereby elevating the work function.[80]

Demetalation: Transition metal has been regarded as an essential part of the PGM-free catalyst. Initially, metallic species have been regarded as active sites by some researchers. Later the metallic species are found to be thermodynamically unstable in the PEMFC environment.[79, 81, 82] Besides, vigorous acid washing has been applied to the PGM-free catalyst synthesis in many works. The catalysts showed very high activity after completely removal of metallic species by acid washing, implying metallic species may not be the active sites.

It is then believed that metallic species remaining in the PGM-free catalyst are encapsulated by protective graphite layers that prevent the otherwise inevitable dissolution of the metallic species.[66] However, even though the encapsulated metallic species is stable in the catalyst, it is not considered as the active site after single-atom catalysts were reported.[83, 84] The Fe-N structure is believed to be stable in PEMFC environment and unlikely to be leached out under normal conditions. Chenitz et al. proposed the rapid water flow in micropores could take the iron away according to the Le Chatelier principle, and such demetalation caused the rapid initial loss in the fuel cells.[71] H_2O_2 attacks may cause demetalation as well. As is discussed in the last section, H_2O_2 can directly attack the N functionalities that coordinate with the transition metal active center.[79] The oxidized N species was hypothesized to dissolve into the surrounding environment, which can cause the metal ion center to dissolve as well. This hypothesis is not supported by many other works and the detailed mechanism is still left vague.

1.6 Organization of Thesis

The main objectives of this thesis are to i) develop effective methodologies for PGM-free catalyst heteroatom doping, ii) understand the mechanism of activity enhancement by favorable catalyst morphology and heteroatom doping, iii) scale up the catalysts for larger-scale applications, iv) understand PEM fuel cell voltage losses at different current density regions, v) optimize the catalyst layer and MEA design to improve the fuel cell performance. Therefore, in this work we applied different methods to enhance the catalytic activity of the catalysts we prepared. We were also able to scale up the catalyst from milligram-scale to gram-scale and applied it in 50 cm^{-2} MEAs. Testing parameters were studied, and the MEAs were optimized based on the 50 cm^{-2} fuel cell. Figure 1-5 depicts a breakdown of work conducted throughout this thesis.

This thesis is organized into six chapters. **Chapter 1** introduces the general background, motivation, PEM fuel cell working mechanism and voltage losses, the status of PGM-free ORR catalyst development, and the scope of the thesis. **Chapter 2** presents some key electrochemical measurement and physicochemical characterization techniques employed throughout the thesis, with in-depth details provided within subsequent Chapter 3 through Chapter 5. **Chapter 3** deals with the unique hollow spherical carbon support development and preparation of the N, S co-doping catalyst with retention of the unique structure. **Chapter 4** focuses on enhancing the PGM-free catalyst activity by dual nitrogen precursor doping, and the catalyst scale-up. **Chapter 5** describes the fuel cell testing parameter study and optimizing the MEA design to improve overall PEM fuel cell performance based on the scaled-up catalyst discussed in Chapter 4. Chapter 6 summarizes the important results and some discussions on the future direction that the work may take.
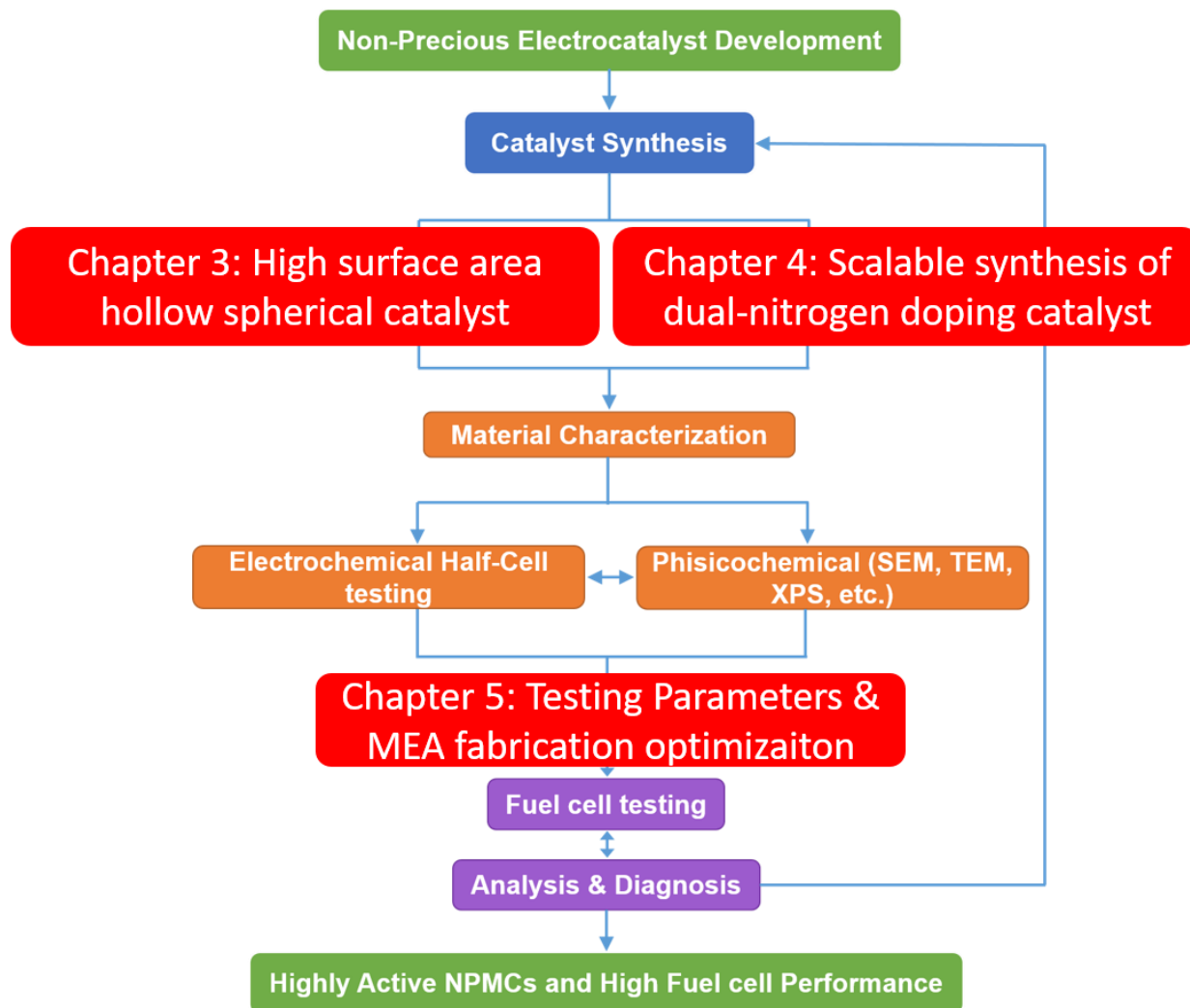
Figure 1- 5. Schematic illustration of the research topics throughout this thesis.

Chapter 2 Characterization Techniques

Developed electrocatalyst materials are extensively characterized by a variety of physicochemical and electrochemical techniques with the results correlated to gain insightful understanding. This will allow elucidation of the important factors governing catalytic activity and PEMFC performance, providing fundamental scientific knowledge and guiding the optimization of developed catalyst materials. This section will illustrate the details regarding several electrochemical and physical characterization techniques that are applied in the research present in this thesis.

2.1 Electrochemical Characterization Techniques

To verify the functionality and to investigate the performance of synthesized catalysts, electrochemical measurements are required. The following two sections explain about half-cell measurement and a fuel cell test.

2.1.1 Rotating disk and ring disk electrode

The rotating disc electrode (RDE) experiment and rotating ring disk electrode (RRDE) experiment are the most widely applied electrochemical characterization techniques to test oxygen reduction reaction activity and other reactions that involve diffusion process. The major difference between the two is that the RRDE is able to test hydrogen peroxide generation during the test. A portion of the H_2O_2 generated by the disk will be oxidized on the ring and generate a current. By calculating the relationship between disk and ring current, the ratio of O_2 reduction to H_2O_2 can be determined. RDE and RRDE work in the three electrodes system to simulate the fuel cell anode/cathode depending on the supplied gas. Because cathode catalyst is of our interest, the oxygen reduction reaction occurs at the working electrode (tip of the RDE) with the purging of

oxygen, resulting in a mimicked half-cell. The counter electrode is necessary to complete the circuit and the reference electrode is used to determine the absolute potential of the working electrode. All three electrodes are immersed in the electrolyte and oxygen is continuously supplied to the system to keep the electrolyte saturated. The three-electrode system is a simple method to quickly verify the as-prepared catalyst, and it saves cost and time compared to assembling and testing a full cell. The schematic illustration for the complete RDE/RRDE system is shown in Figure 2-1.
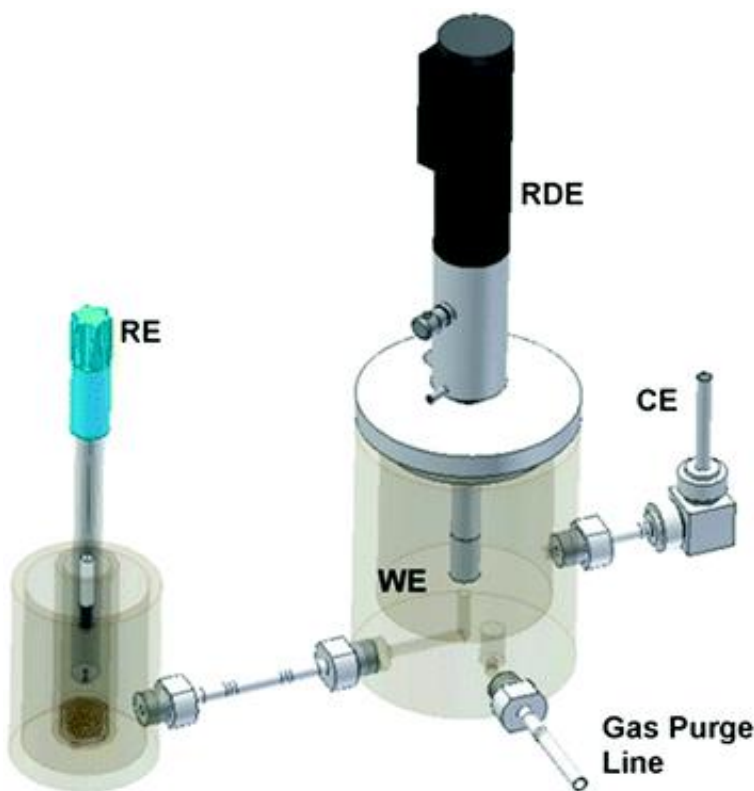
Figure 2- 1. An illustration of an electrochemical three-electrode half-cell RDE setup.

The RDE is made of PTFE and has a round disc made of glassy carbon at the tip, where the catalyst ink will be deposited and form a thin catalyst layer once dried. The rotation feature of this electrode is important because it helps the diffusion of oxygen and reaction products between the electrode surface and electrolyte by creating a laminar flow near the electrode surface. While

RDE is able to carry out most electrochemical measurements on the catalyst that is currently being practiced, RRDE has another ring-type working electrode surrounding the glassy carbon disc. The ring electrode is able to capture a portion of the hydrogen peroxide being generated and determine the selectivity of the catalyst. The surface schematic of the RRDE vs. RDE is shown in Figure 2-2.
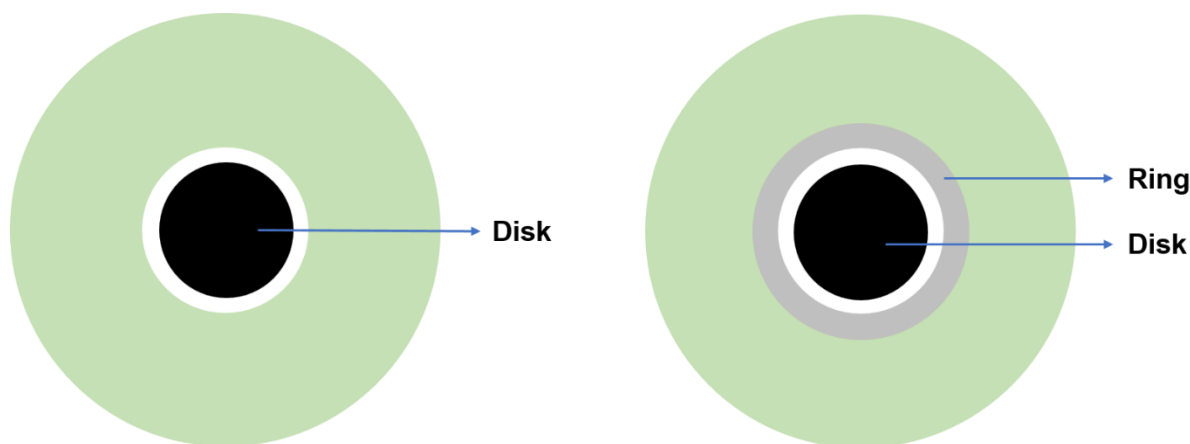
Figure 2- 2. Schematic representation of RRDE and RDE head from a top view.

Reduction of oxygen by two different pathways generates H_2O and H_2O_2 simultaneously at the working electrode, and due to the laminar flow, all the products are pushed away from the glassy carbon towards the ring. When the ring electrode is held at a relatively high voltage, it can oxidize the H_2O_2 to O_2 and the oxidation current is monitored by the second working electrode. With this information, it is possible to calculate the portions of O_2 that is reduced to H_2O_2 (*%H_2O_2*) and H_2O (*%H_2O*), respectively. Since O_2 reduction to H_2O is through a 4-electron pathway, and the reduction to H_2O_2 is through a 2-electron pathway. The overall number (*n*) of electrons transferred during ORR can also be determined. The selectivity of catalyst can be represented by any of the three parameters (*n*, *%H_2O_2*, *%H_2O*), and they are correlated to each other. In the literature, *n* and *H_2O_2%* are most frequently used.

$$n = 4|I_D|/\left(|I_D| + (|I_R|/N)\right) \tag{2.1}$$

$$\%H_2O_2 = 100(4 - n)/2 \tag{2.2}$$

$$\%H_2O = 100 - \%H_2O_2 \tag{2.3}$$

Where n is the electron transfer number, I_D is the current from the disc electrode, I_R is the current from the ring electrode, N is the collection efficiency, $\%H_2O_2$ is the selectivity of H_2O_2 and $\%H_2O$ is the selectivity of H_2O.
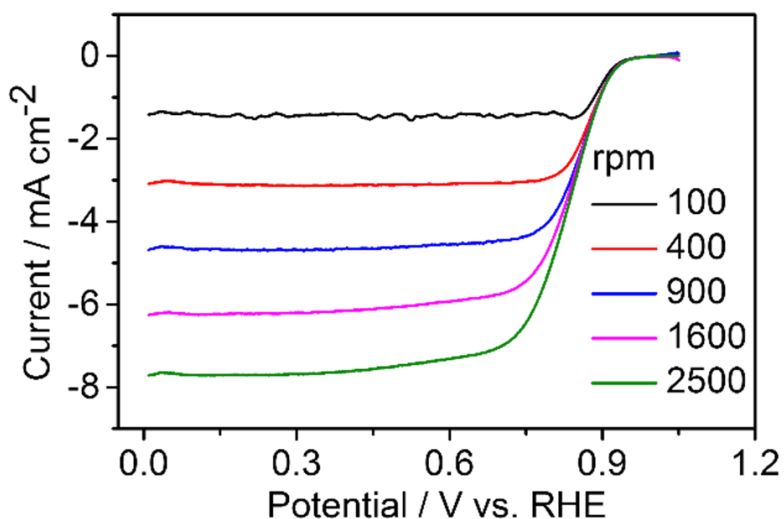
Figure 2- 3. A set of ORR curves with different rotation speeds.

The electrode rotation rate changes the current of the laminar flow which is correlated to the amount of saturated solution to reach the catalyst surface in a given time. An increase in the rotation speed means a higher rate of fuel being supplied at the reaction site. A typical RDE test is done by scanning the potential of the working electrode in a selected range while monitoring the current behavior as plotted in Figure 2-3. A plot of current density versus the potential for a certain range is called the ORR curve, and these curves are usually obtained at a set of rotation speeds of 100, 400, 900, 1600, 2500 rpm or higher in O_2 saturated electrolyte.

At a point where the oxygen reduction reaction initiates, this potential is called onset potential. From this potential to the point where the overpotential of the reaction does not increase the current density, the reaction is governed by its kinetics.[9] The current density in this kinetically limited region is modeled by Equation 2.4:

$$|i_k| = nFAk_fC \tag{2.4}$$

Where i_k is the reaction kinetics controlled current density, n is the electron transfer number, F is the Faraday constant, A is the area of the electrode, k_f is a rate constant as a function of the overpotential, and C is the reactant concentration in the bulk solution.

The current obtained at the region in which the current density does not increase upon changing potential is called the limiting current, where the mass transfer is the limiting factor. The model that describes this steady-state diffusion-controlled system is called the Levich equation and is shown in Equation 2.5.

$$|i_d| = 0.620nFAD^{2/3}\omega^{1/2}v^{-1/6}C \tag{2.5}$$

Where i_d is the diffusion-controlled current density, n is the electron transfer number, F is the Faraday constant, A is the area of the electrode, D is the diffusion coefficient of reactant in the bulk solution, ω is the angular rate of rotation, v is the kinematic viscosity, and C is the reactant concentration.

When the catalyst is deposited on the glassy carbon electrode, the ink usually contains Nafion which forms a layer binding the catalyst. The model that describes the diffusion behavior of reactant through the Nafion binding film is shown in Equation 2.6:

$$\left| i_f \right| = nFAC_f D_f / \delta \tag{2.6}$$

Where if is the diffusion current density of the reactant through the Nafion, n is the electron transfer

number, F is the Faraday's constant, A is the area of the electrode, C_f is the concentration of

reactant in the Nafion film, D_f is the diffusion coefficient of the reactant through the film, and δ is

the thickness of the Nafion layer.

The above three equations can be combined to model the overall current density at a

specific potential in the diffusion layer near the surface of the electrode. This overall expression

for current density is called the Koutecky-Levich equation and is described in Equation 2.7:

$$\frac{1}{|i|} = \frac{1}{|i_d|} + \frac{1}{|i_k|} + \frac{1}{|i_f|} \tag{2.7}$$

Where i is the overall or total current density, i_d is the diffusion-controlled current density, i_k is the

reaction kinetics controlled current density, and if is the diffusion current density of the reactant

through the Nafion.

The durability of catalysts can be investigated by applying accelerated degradation test

(ADT) using a half-cell RDE setup. ADT protocols typically involve subjecting catalyst materials

to repeated cycles and then measuring the ORR activity. These transient conditions will induce

catalyst deactivation and upon comparison to the initial activities, a gauge of catalyst stability can

be provided.

In this work, RDE and RRDE were utilized to characterize the onset potential, half-way

potential, limiting current density, and/or H_2O/H_2O_2 selectivity of the synthesized catalysts. RDE

was also used to investigate the durability of catalysts by repeated cyclic tests.

2.1.2 Membrane Electrode Assembly Testing

Although the half-cell measurement using the RRDE system is an effective way to test the electrocatalytic activity of catalysts, the information given by the half-cell is limited. The actual fuel cell performance can be quite different than the half-cell test due to many other factors. To verify and confirm the actual fuel cell performance of the catalyst, membrane electrode assemblies (MEA) can be fabricated and tested in a full fuel cell. An MEA consists of a polymer electrolyte membrane contained between the anode and the cathode. The electrode is fabricated by depositing the catalyst onto the GDL, which can be accomplished by a variety of different techniques.[85-88] Painting, spraying, filtering or electrodepositing the catalyst materials directly onto the GDL are several examples of electrode fabrication. The catalyst coated GDLs are then combined together with the electrolyte membrane. The MEA must be secured, ensuring uniform contact and adhesion. Catalysts can also be coated directly onto the proton exchange membrane and secured by hot pressing. Using different electrode and MEA fabrication techniques can result in variable electrode architectures and resultant performance and durability. The techniques utilized need to be optimized for the specific catalyst materials under investigation.

After assembling the MEA stack, a polarization curve can be obtained by potential sweep which is similar to that of the half-cell test. The performance evaluation will be done by cycling the cell current/voltage from open-circuit conditions to high current densities. During this testing, the cell voltage/current density is continuously monitored, resulting in an MEA polarization curve similar to the one provided previously in Figure 1-2. Generally, several cycles will be run before recording the actual performance in order to ensure adequate hydration of the electrolytic membrane and activation of the catalyst materials. Many operating parameters can be adjusted including the flow rate for the hydrogen and oxygen, cell temperature, pressure, relative humidity

(RH) and etc. A typical polarization curve along the power density versus current density plot is shown in Figure 2-4, using platinum supported on carbon catalyst for both electrodes.

2.2 Physical Characterization Techniques

The types of physical characterization techniques discussed in the following sections are scanning electron microscopy (SEM), energy dispersive X-ray (EDX), transmission electron microscopy (TEM), X-ray diffraction (XRD), X-ray photoelectron spectroscopy (XPS), and Brunauer-Emmett-Teller (BET) analysis.
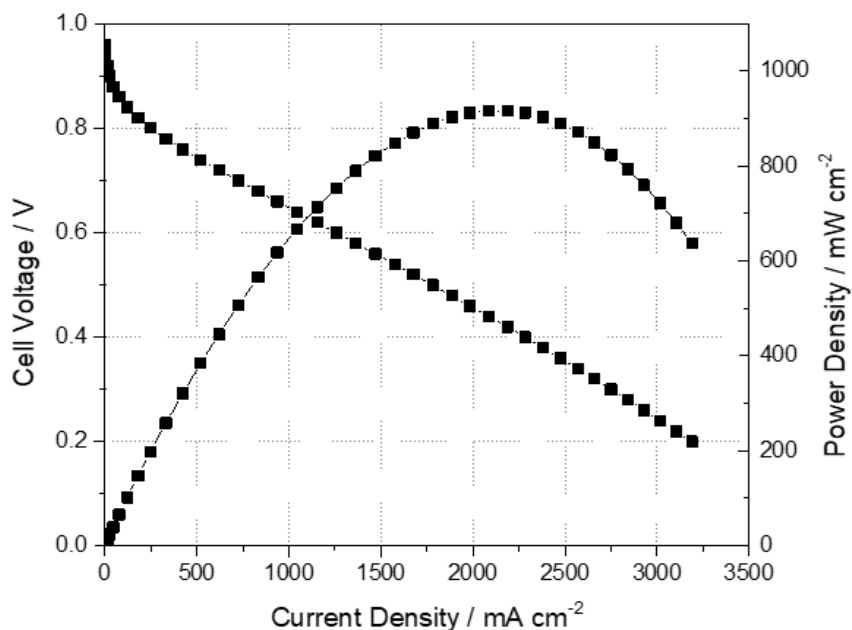
Figure 2- 4. Typical MEA polarization curve with a power density versus current density plot.

2.2.1 Scanning Electron Microscopy/Energy Dispersive X-Ray

Scanning Electron Microscopy (SEM) is one of the most reliable methods for analyzing solid materials.[89] It is a type of electron microscopy that captures images of the surface of the sample by scanning it with a high-energy beam of electrons. Since the emitted electrons have a smaller wavelength than photons, SEM can achieve higher magnification than optical microscopes and is very sensitive. The operation requires the sample to be placed under an ultra-high vacuum.

The emitted electrons hit the surface atoms of the sample and their bombardment and interactions with the sample will produce various types of signals, including secondary electrons, backscattered electrons, and auger electrons. This happens due to the varying energy levels of the incident electrons. They all contain useful information about the sample's morphology, surface topography, compositions, and other important physical properties. In the proposed project, SEM will be applied to investigate the nanostructures of the fabricated electrocatalyst materials. The samples for SEM imaging are prepared by spreading the powder sample onto a conductive carbon tape that is fixed on a sample holder stub. This stub can then be placed into the SEM machine, followed by evacuation of the sample chamber and subsequent imaging. The schematic representation of a typical SEM is illustrated in Figure 2-5.[90]
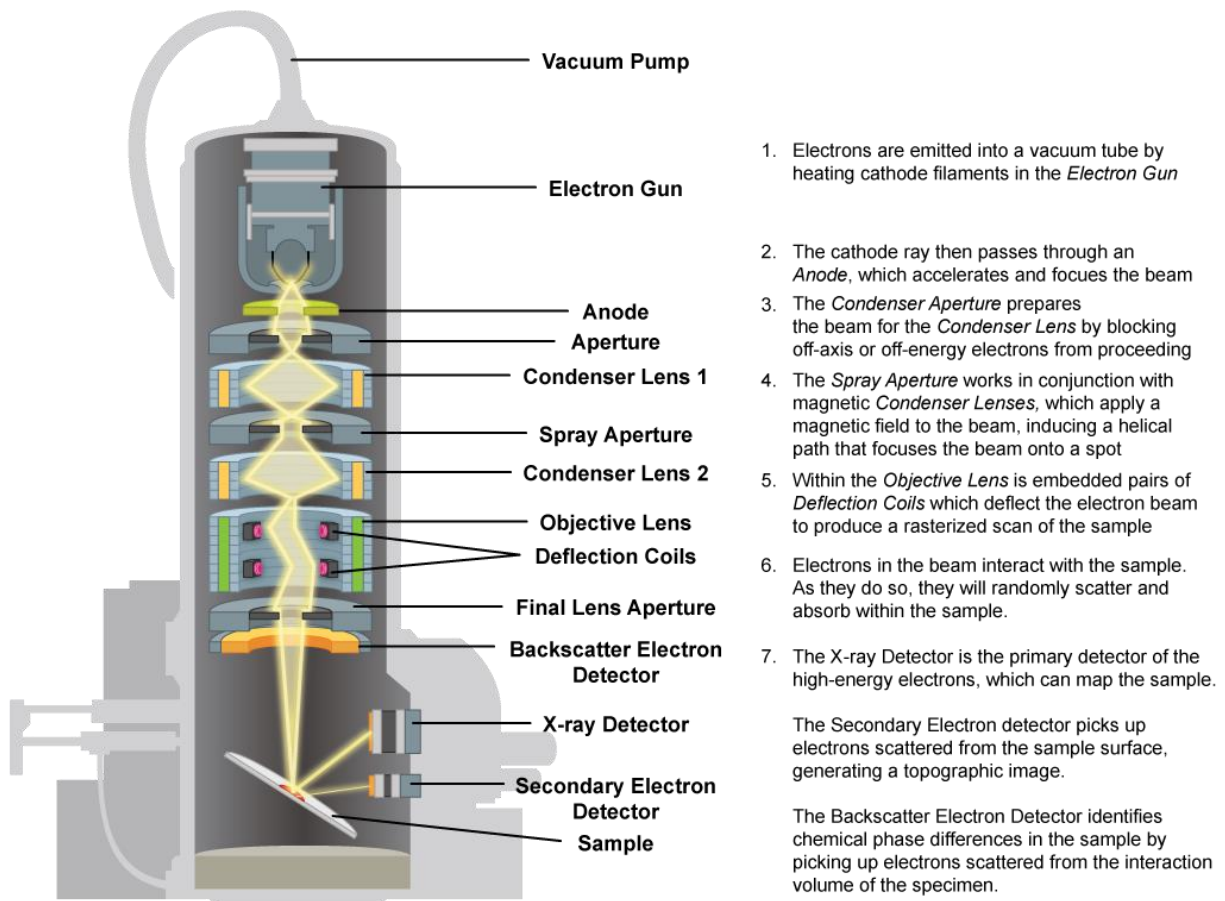
Figure 2- 5. Schematic of a typical scanning electron microscope and imaging process.

2.2.2 Transmission Electron Microscopy

Transmission electron microscopy (TEM) is a technique where a beam of electrons is transmitted through and interacts with an ultra-thin specimen.[91] The schematic showing the inner structure of a TEM machine is shown in Figure 2-6.[90] The electrons are generated by thermionic emission process from a tungsten filament and are aligned and accelerated as they pass through numerous intermediate and projector lenses.[92] An image will be formed from the electrons transmitted through the specimen and it will be magnified and focused by an objective lens. The image produced is the result of beam electrons that are scattered by the specimen versus those that are not.

The major difference between TEM and SEM is the structural information about the sample material they can provide. While TEM is mainly used to study the underlying inner structures of the sample material, SEM is widely used to visualize the surface topography and morphology of the sample material.

TEM is also capable of getting a much better resolution than SEM due to the small de Broglie wavelength of electrons. Equation 2.8 gives the maximum resolution achieved by an optical microscope.

$$d = \frac{\lambda}{2n \sin \alpha} \tag{2.8}$$

Where λ is the wavelength of the photon, n is a positive integer, and d is the theoretical maximum resolution. If we apply the de Brogile wavelength of electrons, this maximum resolution will increase to a degree that the instrument can distinguish objects in a few nanometer ranges.

In this study, TEM was utilized to view the inner morphology of the catalyst materials and to verify the presence of any metallic particles.
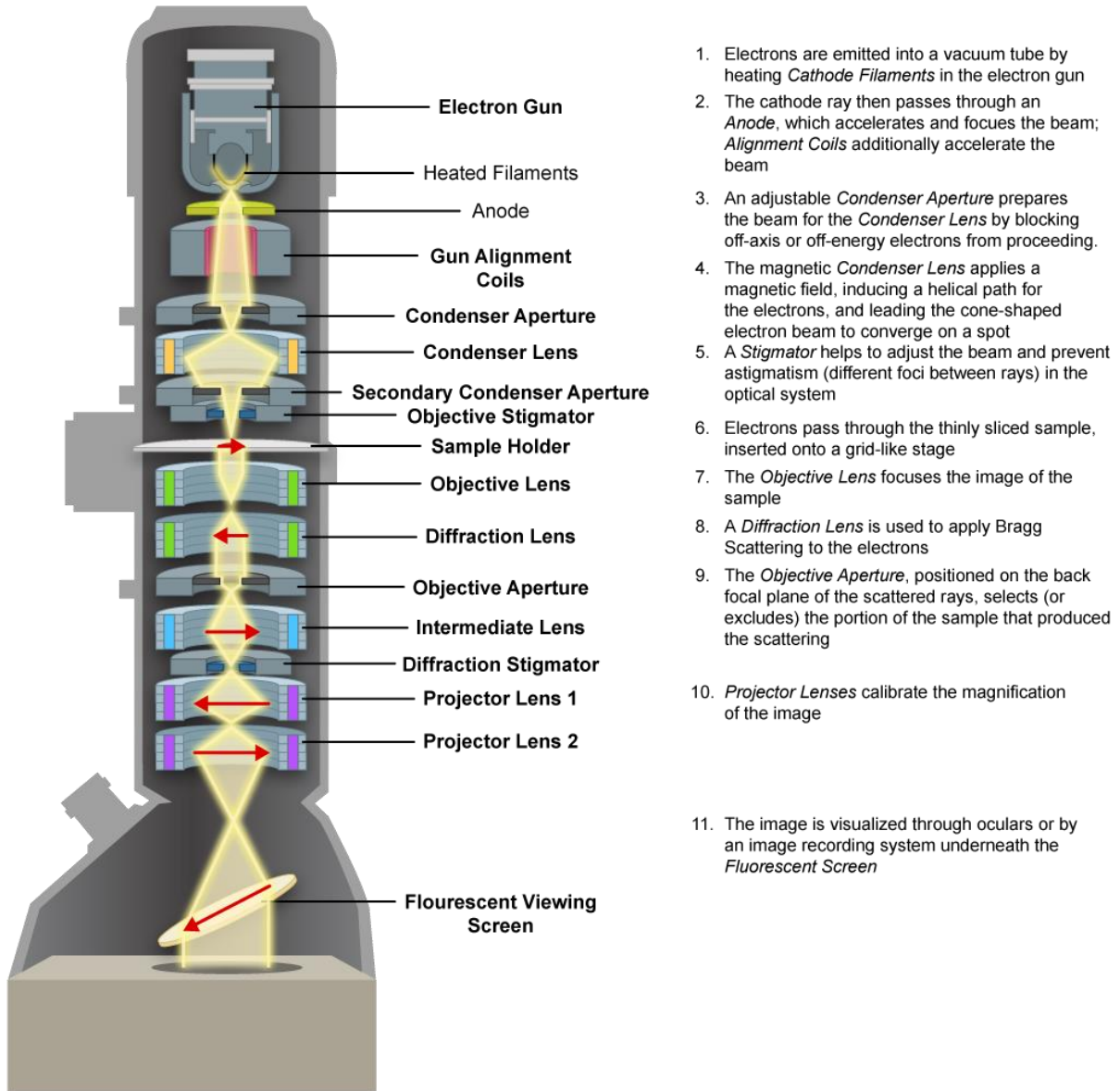
Figure 2- 6. Schematic representation of a column in a transmission electron microscope.

2.2.3 X-Ray Diffraction

X-ray Diffraction (XRD) is a non-destructive characterization technique that identifies the crystalline phases in materials and measures the structural properties such as chemical composition, grain size, and etc.[93] It also determines the thickness of thin films and atomic arrangements in amorphous materials. There are several types of X-ray diffraction such as single-crystal X-ray diffraction, powder diffraction, thin-film diffraction, and high-resolution XRD.

A beam of monochromatic X-rays of known wavelength will be generated by the filament X-ray tubes, by striking an anode (Cu in this case) of a particular metal with high-energy electrons. The incident X-Rays will pass through divergence limiting slit, bombard the sample at a certain angle and reach the detector through a receiving slit. Interaction of X-rays with sample creates secondary diffracted beams of X-rays that are related to interplanar spacings in the powder, according to Bragg's Law (Equation 2.9):

$$n \lambda = 2d \sin \theta \qquad (2.9)$$

Where n is an integer, λ is the wavelength of X-rays, d is the interplanar spacing, and θ is the diffraction angle. The information given by the reflected X-rays is based on the atomic structure of the sample materials which is caused by the elastic scattering of X-rays from the electron clouds of the species within the sample.[94]

From XRD spectra, the mean platinum particle size can be easily estimated from Scherrer's equation (Equation 2.10)

$$d = K\lambda / (B \cos\theta) \qquad (2.10)$$

Where d is the particle diameter (nm), K is the shape factor, λ is the wavelength of the x-rays (0.154 nm for Cu-Ka), B is the full width at half-maximum (FWHM) of the peak of the interest in radian and θ is the Bragg angle of the peak in degrees. In this study, XRD was applied to obtain the morphology and crystallinity of the carbon materials and to identify the presence and state of the metal.

2.2.4   X-Ray Photoelectron Spectroscopy

X-ray photoelectron spectroscopy (XPS) is a quantitative technique that measures elemental composition, chemical states, and electronic states existing in the sample material. The XPS spectra are obtained by irradiating the sample with a beam of X-rays while measuring the number of electrons and the kinetic energy from material.[95]

Conventional XPS instruments utilize a highly focused 20 to 200 μm beams of monochromatic aluminum K-alpha X-rays. Due to the sensitivity of the instrument and to accurately detect the number of electrons, the device must be operated in an ultra-high vacuum to minimize any source of error. XPS can only analyze materials with their atomic numbers equal to or greater than three since the orbitals in hydrogen or helium are too small. This spectroscopy technique is commonly used for materials such as inorganic compounds, metal alloys, semiconductors, polymers, ceramics and etc.

In this work, XPS was utilized to analyze the surface concentrations of various elements, including iron, nitrogen, and carbon in the catalysts. It was also used to quantify the different types of nitrogen-carbon bonds existing on the catalysts to see which structure is mostly related to the electrocatalytic active sites.

2.2.5 Gas (Nitrogen) Sorption Analysis

Gas sorption analysis utilizes the physical adsorption of gases onto solid materials to measure the specific surface area of the solid. The theory works based on following assumptions: adsorption occurs only on well-defined sites of the sample; the only molecular interaction considered is the following one: a molecule can act as a single adsorption site for a molecule of the upper layer; the uppermost molecule layer is in equilibrium with the gas phase; the desorption is a kinetically-limited process; at the saturation pressure, the molecule layer number tends to infinity. Gas sorption analysis is useful for obtaining structural information on the catalyst, especially for the porous materials. The principle of nanotechnology is to increase the reaction sites by increasing the specific surface area to achieve superior activity, thus the specific surface area measured by nitrogen adsorption-desorption can be a significant source of evidence. In this work, Gas sorption analysis was utilized to measure the specific surface areas and pore size distributions in the catalysts synthesized in this study.

Chapter 3 Embellished Hollow Spherical Catalyst Boosting Activity and Durability for Oxygen Reduction Reaction

3.1 Introduction

Increasing consumption of energy and the rising rate of carbon dioxide emissions have caused the twin challenges of energy shortage and climate change. To address these problems, researchers have developed various electrochemical technologies including fuel cells,[96-98] lithium-ion batteries,[99-101] metal-air batteries,[102-104] metal-sulfur batteries,[105-107] flow batteries,[108-110] and so on. In principle, these electrochemical devices generate electricity through the integration of two separate half-reactions. For fuel cells and metal-air batteries with the air electrodes, the oxygen reduction reaction (ORR) is the crucial half-reaction that limits overall power performance.[111-113] In order to overcome the sluggish kinetics of the oxygen reduction reaction, a catalyst accelerating the ORR process is essential at the air electrode. Up to now, platinum group metal-based electrocatalysts are the most active and stable catalysts for ORR. However, the widespread use of these precious metals is impeded by the high cost and limited reserves. A considerable alternative is to search for cost-effective and earth-abundant PGM-free catalysts.

Along with the development of PGM-free catalysts, the understanding of their ORR active sites has been evolving over the past few decades. To date, some scientists think that transition metals are directly involved in the active sites by metal-nitrogen coordination.[63, 114, 115] On the other hand, some others believe that the active sites stay in the carbon and nitrogen frameworks, and transition metals only catalyze the formation of these active sites.[116, 117] Even though the academia holds different opinions on the nature of active sites, it is conclusive that the PGM-free catalysts prepared with transition metals are superior to the transition metal-free catalysts,

especially in an acidic medium. One of the joint efforts made by scientists in the past few decades is to find proper precursors to achieve higher electrocatalytic activity. Metal-N_x chelate was initially proven to be ORR active,[118] and then pyrolyzed non-macrocyclic material demonstrated high activity towards ORR several years later.[28] Since the precursors shifted from macrocyclic material to non-macrocyclic material, many varieties of nitrogen precursors have emerged in recent years,[119-121] as well as other types of heteroatom (boron, sulfur, phosphorus, etc.) doping and dual doping precursors.[122, 123] An additional heteroatom dual doping is believed to not only increase the active site density but also the activity of the active sites.[124] When selecting heteroatom precursors, researchers normally focus on factors like heteroatom content and molecular configuration, but little attention has been paid to the effect of molecular size. Although many different monomers and polymers have been used individually as heteroatom precursors in numerous researches, no work has been done to specifically study the difference between a monomer and its polymer as heteroatom precursors. Therefore, considering the component similarity and the molecular size imparity between a monomer and its polymer, it is worthwhile to investigate the similarities and differences between the two types of catalysts derived from monomers and their polymer counterparts, respectively.

Therefore, inspired by the discussion above, we have designed PGM-free catalysts which are heat-treated composites of an iron precursor together with poly(aminothiophenol) (PATP) and its monomer aminothiophenol (ATP), respectively. Particularly, ultra-high surface area nitrogen-doped hollow carbon spheres (HCS) was successfully achieved for supporting the catalytically active materials. The spherical morphology was purposely targeted because the void spaces among the spheres are sufficient for oxygen permeation, and the ultra-high surface area allows the catalyst to carry more accessible active sites. Accordingly, several interesting findings were observed for

HCS-supported Fe-N/C catalyst derived from ATP (HCS-A) compared to the catalyst derived from PATP (HCS-PA). Firstly, HCS-A is able to maintain the hollow spherical structure and high surface area from activated HCS, while HCS-PA transforms into large carbon particles coexisting with carbon spheres and sacrifices most of the surface area. Secondly, elemental surface composition and chemical states of each element are quite similar for HCS-A and HCS-PA, indicating that similar chemical bonding and active sites were formed. Thirdly, HCS-A shows better ORR activity than HCS-PA in terms of both kinetic and mass transport processes.

3.2 Materials and Methods

3.2.1 Material synthesis

Preparation of activated hollow carbon sphere (HCS): Firstly, polyaniline-co-polypyrrole nanospheres were synthesized through the emulsion polymerization method with Triton X-100 as the surfactant.[125, 126] The obtained copolymer was pre-carbonized at 400 °C to get HCS. After that, the HCS was mixed with KOH at a mass ratio of 1:3. The mixture was heated to 800 °C under the protection of argon at a ramp rate of 5 °C/min and held for 1 hour to get activated HCS. The activated HCS was then washed with DDI to neutral pH and dried in a vacuum oven for later use.

Preparation of HCS-PA: In a typical protocol, 120 mg 2-aminothiophenol and 20 mg ferrous acetate were dissolved in 20ml ethanol, respectively. The 2-aminothiophenol solution was added to the ferrous acetate solution dropwise with vigorous stirring. Then, a certain amount of ammonium persulphate solution was added. The mixed solution was heated to 60 °C to allow for polymerization. After polymerizing for 8 hours, 60 mg activated HCS powder was added to the solution. After 1 hour of sonication and stirring overnight, the mixture was dried at 80 °C and

ground into a fine powder. HCS-PA was obtained after pyrolysis of the dry powder at 900 °C for 1 hour.

Preparation of HCS-A: In a typical protocol, 120 mg 2-Aminothiophenol and 20 mg ferrous acetate were dissolved in 20ml ethanol, respectively. The 2-aminothiophenol solution was added to the ferrous acetate solution dropwise with vigorous stirring. The mixed solution turned black after 2-aminothiophenol was added and back to brown after stirring for several minutes. Then, 60 mg of activated HCS powder was added to the solution. After sonication for 1 hour and stirring overnight, the mixture was dried at 80 °C and ground into a fine powder. HCS-A was obtained after pyrolysis of the dry powder at 900 °C for 1 hour.

3.2.2 Physicochemical characterizations

The catalyst morphology was investigated by scanning electron microscopy (SEM) with an LEO FESEM 1530 microscope, and transmission electron microscopy (TEM) with a JEOL 2010F TEM/STEM field emission microscope. Brunauer-Emmett-Teller (BET) surface area was measured by the nitrogen adsorption and desorption technique through a Micromeritics ASAP 2010M system. X-ray photoelectron spectroscopy (XPS) was performed ith a Thermal Scientific K-alpha XPS spectrometer to collect the lemental composition of the catalyst materials.

3.2.3 Electrochemical measurements

RDE and RRDE measurements were performed using a CHI Electrochemical Station (Model 750b) in a standard three-electrode cell. For RDE, a 5.0 mm diameter glassy carbon disk (disk geometric area 0.196 cm^2) was used. The RRDE has an extra Pt electrode with an inner diameter and outer diameter of 6.5 mm and 7.5 mm (ring geometric area 0.110 cm^2). To avoid any potential contamination of the catalyst by Pt, all experiments were carried out with a graphite rod

as a counter electrode. Ag/AgCl (filled with 3M KCl) electrode and SCE electrode were used as the reference electrode in acidic medium (0.5 M H_2SO_4) and alkaline medium (0.1 M KOH), respectively. All potentials initially measured against the Ag/AgCl electrode and SCE electrode were converted to an RHE scale. The catalyst ink was prepared by adding 5 mg of the catalyst to 1 ml isopropanol and ultrasonically blending for 30 min. 20 μl of the ink and 3 μl of 0.25 wt.% Nafion solution was applied to the 0.196 cm^2 disk in sequence, resulting in a catalyst loading of ca. 0.5 mg cm^{-2}. RDE polarization plots were recorded in both O2-saturated and N2-saturated electrolyte at a scan rate of 5 mV s^{-1}. The results shown in this paper have subtracted the N_2 background. RDE cycling stability tests of the HCS-A catalyst were performed in N2-saturated electrolyte in the potential range from 0.6 to 1.0 V at room temperature. The RRDE collection efficiency N was measured using the reversible $[Fe(CN)_6]^{4-}/[Fe(N)_6]^{3-}$ system. The electrolyte was deaerated 0.1 M KCl with 0.01 M $K_3Fe(N)_6$ and the electrode was rotated under the rotation rates of 400, 900, 1600, and 2500 rpm. Disk potential (E_d) was scanned from 0.8 V to 0.1 V vs. RHE at a scan rate of 10 mV s^{-1} to reduce $[Fe(N)_6]^{3-}$ to $[Fe(CN)_6]^{4-}$. The ring was set at a constant potential (E_r) of 1.5 V vs. RHE to oxidize $[Fe(CN)_6]^{4-}$ back to $[Fe(N)_6]^{3-}$. The collection efficiency can be determined by I_d and I_r: N = - I_r/I_d. The collection efficiency remains a constant value of 0.28 ± 0.2 under various ω.

Fuel cell testing: HCS-A catalyst was tested in the fuel cell cathode to evaluate its activity under PEMFC operating conditions. The catalyst ink was prepared by ultrasonically mixing the catalyst powder with Nafion suspension for 1 hour. Then, the catalyst "ink" was brush-painted to the gas diffusion layer (GDL, 29 BC, Ion Power) until the cathode catalyst loading reached ca. 4 mg cm^{-2}. The Nafion content in the catalyst layer was maintained at ca. 35 wt%. Commercial Pt deposited carbon cloth GDE (0.2 mg cm^{-2} Pt, Fuel Cell Etc) was used at the anode. The cathode

and anode were hot-pressed onto two sides of a Nafion® 211 membrane to form a three-layer membrane-electrode assembly (MEA). The geometric MEA area was 5.0 cm^2. Fuel cell testing was carried out in a single cell with serpentine flow channels. Pure hydrogen and oxygen, humidified at 80°C, were supplied to the anode and cathode at a flow rate of 200 sccm. Both electrodes were maintained at the same absolute pressure of 20 psi. Fuel cell polarization plots were recorded using fuel cell test stations (Scribner 850e).

Zinc-air battery testing: The single-cell battery was tested using a home-made practical zinc-air battery and a multichannel potentiostat (Princeton Applied Research, VersaSTAT MC) at room temperature. A polished zinc plate (Zinc Sheet EN 988, OnlineMetals) and gas diffusion layer (GDL, ELAT LT 1400W, E-TEK) sprayed with the HCS-A loading of ca. 2 mg cm^{-2} was used as the anode and cathode, respectively. The cathode was exposed to completely ambient air with no O_2 pre-bubbling or continuous O_2 supply. A microporous membrane (25 μm polypropylene membrane, Celgard 5550) and 6.0 M KOH were used as the separator and electrolyte, respectively. The area of the active material layer exposed to the electrolyte and ambient air was 0.785 cm^2.

3.3 Results and Discussion

3.3.1 Physicochemical properties

The catalyst preparation process is shown in Fig. 1. Hollow carbon sphere (HCS) structure was first prepared by pre-carbonization of the polyaniline-co-polypyrrole copolymer, followed by KOH etching to obtain activated HCS with ultra-high surface area (Figure 3-1 (a)). In order to obtain a highly active ORR catalyst, we used Poly-aminothiophenol (PATP), a sulfur-containing analog of polyaniline, as the heteroatom precursor, ferric chloride as the metal precursor and HCS

as carbon support to prepare the final HCS-PA catalyst (Figure 3-1 (b)). As a result, PATP agglomerated and destroyed the uniform structure of HCS. Then, we tested another strategy by using aminothiophenol (ATP) as the heteroatom precursor to prepare HCS-A with the same
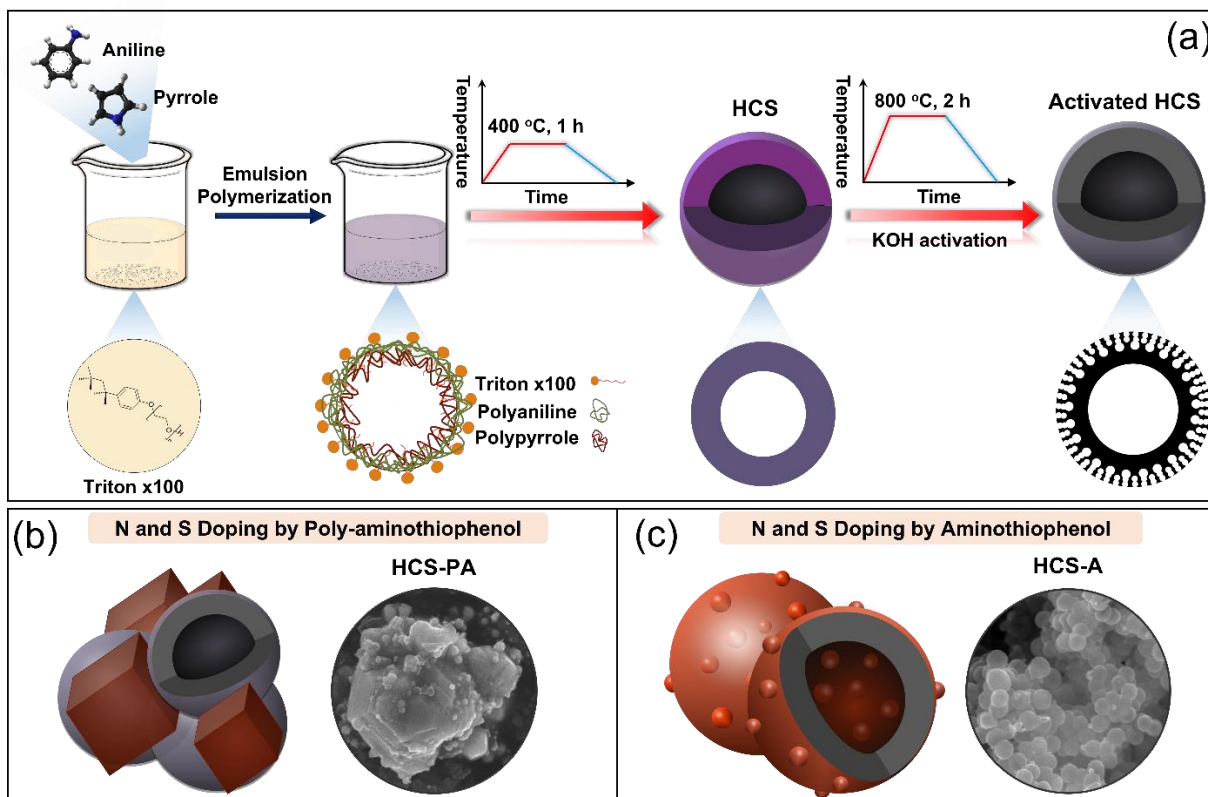
Figure 3- 1. (a) The synthesis process of Activated HCS; Schematic illustration and SEM image of (b) HCS-PA and (c) HCS-A.

synthesis procedure (Figure 3-1 (c)). Catalyst morphology, surface area, and surface composition were further characterized to study HCS-A and HCS-PA, and conclude the factors that contribute to the ORR activity.

The pre-carbonized HCS exhibited well-defined spherical morphology with a uniform particle size distribution as shown in SEM images (Figure 3-2 (a)). When we look at the TEM images (Figure 3-2 (b)), a highly organized hollow structure with a uniform shell thickness can be observed. The outer and inner diameters of the hollow sphere are ca. 110 nm and 60 nm,

respectively. After KOH activation at 800 °C, most of the HCS spheres were able to maintain their spherical structure. Additionally, small wrinkles can be observed on the edge of the spheres, indicating that the surface layer has been etched during activation. It is also found that some of the spheres were broken, becoming open-shell spheres, which exposes the inner surface. As KOH
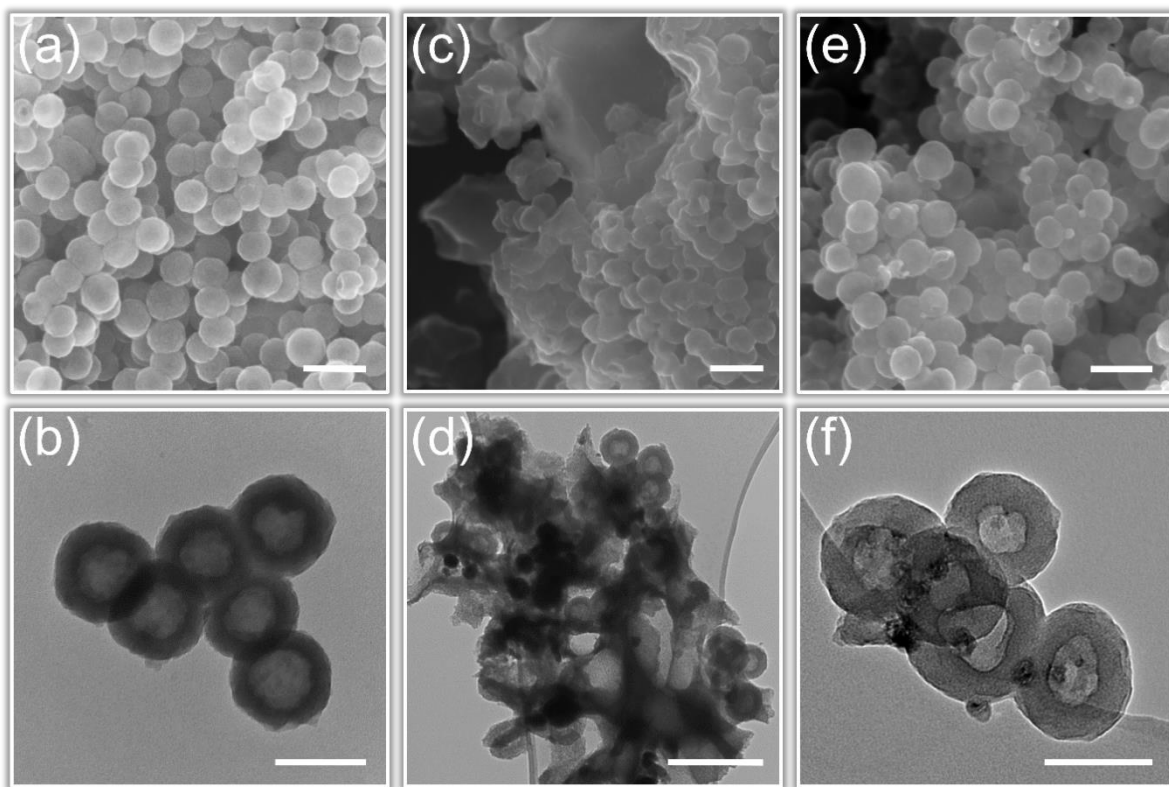
Figure 3- 2. SEM images of (a) HCS, (c) HCS-PA, (e) HCS-A, and TEM images of (b) HCS, (d) HCS-PA, (f) HCS-A. Scale bar:(a), (c) 200 nm, (d), (e) 300 nm and (b), (f) 100 nm.

activation is a well-established method to produce micropores,[127] the holes which are large enough to penetrate the shell were probably created by agglomerated large KOH particles during high-temperature treatment.

From Figure 3-2 (c-f), hollow spheres can be observed in both HCS-PA and HCS-A after heteroatom doping and secondary annealing at 900 °C under the protection of argon. For HCS-PA, PATP was carbonized and became large pieces of bulk carbon material, coexisting with

nanospheres (Figure 3-2 (c), (d)). However, benefiting from the small molecular size of ATP, HCS-A largely retained the original spherical structure from HCS with granular additions, becoming nano-sized bumpy balls (Figure 3-1). Also, as shown in the TEM images (Figure 3-2 (f)), the surface of HCS-A is much smoother than that of activated HCS. This can be attributed to the ATP molecules adsorbing on the surface of activated HCS and filling the cavities of activated HCS. It was verified by N_2 adsorption-desorption isotherm BET surface area (Fig. S5 and Table S1) that HCS-A has a specific surface area of 1531 m^2 g^{-1}, which is less than that of activated HCS with a specific surface area of 2487 m^2 g^{-1}, illustrating that the surface area of activated HCS was partially covered by ATP. In comparison to the HCS-PA (BET surface area of 987 m^2 g^{-1}), HCS-A shows a much higher surface area because ATP is easier to volatilize and decompose under high temperatures than PATP, and ATP does not form large non-porous particles after high-temperature treatment. During pyrolysis, the volatilization and decomposition of ATP could also help increase the porosity of HCS-A. However, for HCS-PA, the polymerization could cause both the formation of large particles and HCS agglomeration (Figure 3-2 (c), (d)), hence sacrificing most of the surface area.

Table 1. BET specific surface area of activated HCS, HCS-PA and HCS-A.

Sample name	BET specific surface area (m^2/g)
Activated HCS	2486.6
HCS-PA	998.7
HCS-A	1531.7

As HCS-A and HCS-PA show different morphologies, it is important to study the final elemental composition and the chemical states of each element in these two catalysts. The atomic ratios of nitrogen, sulfur, and iron are shown in Figure 3-3 (a). HSC-A shows lower nitrogen content than HCS-PA, indicating that more ATP moieties have volatilized and decomposed during

pyrolysis. The bonding configurations of nitrogen in HCS-A and HCS-PA are shown by the N1s core level spectra (Figure 3-3 (b)). Both of the nitrogen spectra can be divided into three categories: pyridinic nitrogen (398.2 eV ± 0.2 eV), graphitic nitrogen (401.0 eV ± 0.2 eV), and oxidic nitrogen (404.0 eV ± 0.2 eV). Among these categories, pyridinic nitrogen and graphitic nitrogen are generally considered to be most active for ORR.[128] The peaks with lower binding energy, located at about 398.2 eV, can be attributed to pyridinic nitrogen, in which a pair of p-electrons appears in the π-conjugated system of the graphene layers. Pyridinic N is able to create a Lewis basic site, thus O_2 can be adsorbed at the carbon atom next to the pyridinic N. This is followed by protonation of the oxygen molecule and further reduction. When carbon atoms within the graphene layers are substituted by nitrogen atoms in the form of "graphitic" nitrogen, the corresponding peak in the high-resolution N1s spectra is located at 400.8eV. The high energy peak at 404.0 eV is commonly attributed to the nitrogen oxide groups, which are considered inert in the oxygen reduction reaction. Pyridinic nitrogen and graphitic nitrogen dominate in both HCS-A and HCS-PA. From the N1s peaks, we know quaternary N and pyridinic N are the dominating nitrogen species in both HCS-A and HCS-PA, which are likely to make the main contribution to the activity of the catalysts.

In addition to nitrogen, HCS-A and HCS-PA were simultaneously doped with sulfur as ATP and PATP contain both nitrogen and sulfur. The high-resolution S 2p spectra are shown in Figure 3-3 (c), all of which came from the spin-orbit coupling, S $2p_{3/2}$, and S $2p_{1/2}$, with 1.2 eV energy splitting and 1:2 intensity ratio.[129] For both HCS-A and HCS-PA, the S 2p core level doublet centered at 163.8/165.0 shows the presence of C-S-C species,[130] revealing successful S doping into the carbon matrix. The two minor doublets located between 161.4 to 163.8 eV are attributed to FeS_x species, indicating that a very small amount of S has combined with iron to form iron sulfides. Other minor doublets between 165.2 to 169.5 eV are attributed to SO_x species, which
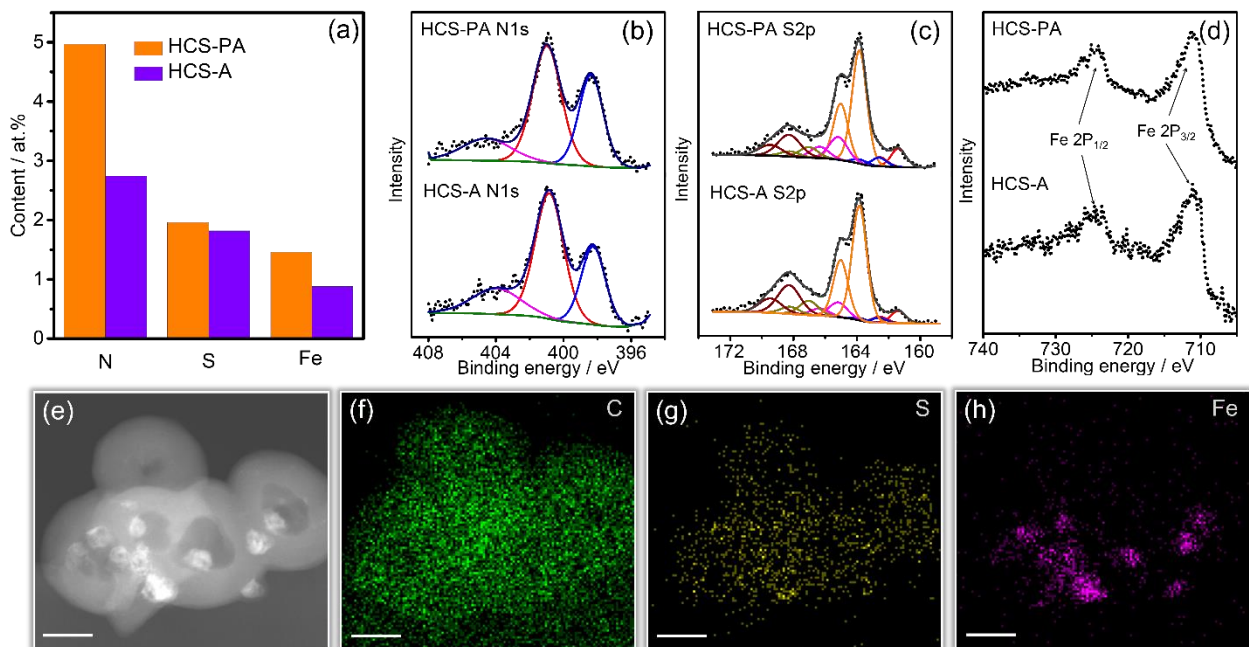
Figure 3- 3. Elemental analysis of HCS-PA and HCS-A. a) N 1s, b) S 2p and c) Fe 2P XPS spectra, d) N, S, and Fe content. e-h) STEM dark field image and the corresponding EDX element mapping for the C, S and Fe atoms for HCS-A, Scale bar: 50 nm.

is reasonable as the activated HCS surface contains abundant oxygen-containing groups after KOH activation. The doublet centered at 163.8/165.0 accounts for 54% of the total S species, the majority of sulfur is doped into the carbon framework for both HCS-A and HCS-PA, and may positively modify the catalytic properties as reported by some other sulfur-doped materials.[131] Sulfur doping could increase the spin density of the adjacent carbon atoms as well as the number of active atoms, which means that both activity and density of the active sites could be enhanced by sulfur doping. It also must be noted that although the activity of S-C moieties may be inferior to Fe-N moieties, the existence of S-C moieties broadens the potential range for oxygen reduction. In Figure 3-3 (d), the XPS Fe 2p core-level spectra show the same peak positions for HCS-A and HCS-PA. The Fe $2P_{3/2}$ peaks are located at 711.2 eV and Fe $2P_{1/2}$ peaks are located at 724.1 eV, which are due to the coexistence of ferrous and ferric states.[132] Overall, it is very interesting to

learn from the XPS spectra that independent of the precursors that have been used, the doped elements for HCS-A and HCS-PA appear in similar elemental composition and nearly identical chemical states for each element.

Energy-dispersive X-ray spectroscopy (EDX) element mapping has been done to study the elemental distribution on the surface of HCS-A. Figure 3-3 (f) and g show that the mapping images of carbon and sulfur overlap with each other, indicating uniform S doping in the carbon matrix. This uniform sulfur distribution could benefit from the homogeneous absorption of ATP on HCS surface before pyrolysis. Figure 3-3 (h) shows that parts of Fe elements gather together at certain spots where iron particles are located. Other than the iron particles, Fe atoms were also uniformly distributed on the HCS-A surface, which could be attributed to the effects of N and S tethering with Fe.[49]

Physicochemical characterization demonstrates that the catalysts prepared from ATP and PATP (i.e. HCS-A and HCS-PA) show similar elemental composition. Moreover, all the elements that closely relate to active sites (e.g. iron, nitrogen, and sulfur) are almost of the same chemical states for the two materials, indicating that the same types of chemical bonds are formed among those elements within HCS-A and HCS-PA. Interestingly, HCS-A and HCS-PA show quite considerable differences in terms of morphology (Figure 3-2 (c-f)) and surface area (Table 1). HCS-A preserved the morphology of HCS with a few iron particles decorating on the sphere surface, while large (>500 nm) particles of carbon and small (~110 nm) spheres co-exist in HCS-PA. Accordingly, HCS-A inherited more of the surface area from activated HCS than HCS-PA did. Structure and composition are the two key factors impacting activity, and any differences within these two factors could have an impact on the catalytic activity of HCS-A and HCS-PA.

3.3.2 Electrochemical ativities

To evaluate the electrocatalytic ORR activity, linear sweep voltammetry (LSV) was carried out in both acidic (0.5 M H_2SO_4) and alkaline (0.1 M KOH) media. The catalysts were tested in both O_2 and N_2, and all the LSV curves for ORR were plotted after subtracting the N_2 background (Figure 3-4 (a), (b)). HCS-mf is a metal-free catalyst prepared from only HCS and aminothiophenol, with the same synthesis procedure as HCS-A. Both HCS-A and HCS-PA show much higher activities compared to the metal-free catalyst, testifying to the significance of the iron species to ORR activity. In the acidic medium, HCS-A and HCS-PA reached the mass transport limiting current at a potentially less than ca. 0.7 V vs. RHE. The mixed kinetic and mass transport controlled region was reached within the potential range from 0.7 V to 0.8 V vs. RHE. Both HCS-A and HCS-PA show higher activity in the alkaline medium as seen in Figure 3-4 (b). The mass transport limiting current was reached at around 0.8 V vs. RHE and the mixed control region is located between 0.8 V and 0.9 V vs. RHE. Compared to HCS-PA, HCS-A demonstrated superior ORR activity in both media in terms of half-wave potential and limiting current. At a current density of 2 mA cm^{-2}, HCS-A surpasses HCS-PA by 45 mV and 36 mV in 0.5 M H_2SO_4 and 0.1 M KOH, respectively (Table 2).

Table 2. Electrochemical performance measured for HCS-PA and HCS-A.

Catalyst	Acidic medium		Alkaline medium	
	$E_{1/2}$ (V vs. RHE)	j_d @ 0.3 V (mA cm^{-2})	$E_{1/2}$ (V vs. RHE)	j_d @ 0.3 V (mA cm^{-2})
HCS-A	0.751	4.3	0.866	4.7
HCS-PA	0.718	3.9	0.830	4.3

Compared to other catalysts in literature, HCS-A has also one of the best ORR activities reported so far, especially in alkaline medium. HCS-A exhibited slightly lower onset potential than commercial TKK Pt/C catalyst in 0.1 M KOH, which means the active sites on HCS-A have intrinsically lower activity than Pt-based active sites. However, the half-wave potential of HCS-A is slightly higher than that of Pt/C catalyst. There are two main reasons for the higher half-wave potential: one is that the active sites on HCS-A are distributed more uniformly and closely, allowing for the involvement of more active sites to facilitate the reaction, and thus current density is able to increase faster at the kinetic region. The other reason is that the void spaces in HCS-A facilitated mass transport and made it easier and faster to reach the diffusion limiting current plateau. HCS-A shows a slightly higher limiting current density in both acid and base than HCS-PA, suggesting that the oxygen reduction pathways for HCS-A and HCS-PA could be slightly different in the two media. The overall multielectron reaction of oxygen reduction has two main pathways. One is a $2e^-$ reduction pathway that produces a peroxide species (HO_2^-), and the other is a direct $4e^-$ pathway which produces H_2O. The $2e^-$ transfer pathway can be represented as:

$$O_2 + H^+ + 2e^- \rightarrow HO_2^- \text{ (Acidic medium)} \quad (1)$$

$$O_2 + H_2O + 2e^- \rightarrow HO_2^- + OH^- \text{ (Alkaline medium)} \quad (2)$$
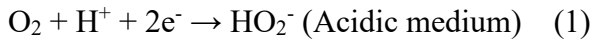
The direct $4e^-$ transfer pathway can be represented as:

$$O_2 + 4H^+ + 4e^- \rightarrow 2H_2O \text{ (Acidic medium)} \quad (3)$$

$$O_2 + 2H_2O + 4e^- \rightarrow 4OH^- \text{ (Alkaline medium)} \quad (4)$$
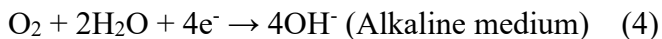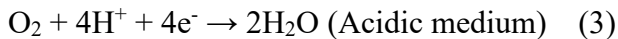
To clarify the reduction pathways for HCS-A and HCS-PA, we performed rotating ring disk electrode (RRDE) measurements to monitor the formation of peroxide species (HO_2^-) during the oxygen reduction process (Figure 4 (c), (d)). The disk electrode was scanned cathodically at a

scanning rate of 5 mV s^{-1}, and the ring electrode was set at a 1.3 V vs. RHE to oxidize HO$_2^-$. The electron transfer number (n) and yield of peroxide species (%HO$_2^-$) were calculated by the following equation:

$$n = 4 \times \frac{I_d}{I_d + I_r/N} \quad (5)$$

$$HO_2^- \% = 200 \times \frac{I_r/N}{I_d + I_r/N} \quad (6)$$

In which I$_d$ is the disk current, I$_r$ is the ring current and N is the current collection efficiency of the ring electrode. N was determined to be 0.28 based on the reduction of K$_3$Fe[CN]$_6$. Since oxygen can be either fully reduced to H$_2$O through the 4e$^-$ pathway, or reduced to HO$_2^-$ through the 2e$^-$ pathway, the calculated electron transfer number is an apparent value which represents the mixture of the 2e$^-$ and 4e$^-$ pathways in a certain ratio. As observed in Figure 3-5, HCS-A shows a lower ring current density in both media, showing less HO$_2^-$ was detected on the ring electrode. Electron transfer number and hydrogen peroxide production are calculated and shown in Figure 3-4 (c), (d). Both HCS-A and HCS-PA show lower yields of HO$_2^-$ in 0.1 M KOH, which is well in accordance with the polarization curve, demonstrating that both catalysts show higher activity in 0.1 M KOH. If we compare HCS-A and HCS-PA, it is easy to discover that HCS-A catalyzes the oxygen reduction with a higher electron transfer number in both media, which means HCS-A has better selectivity of the 4e$^-$ pathway to directly reduce O$_2$ to H$_2$O. A 4e$^-$ pathway is desired for the following two reasons: firstly, it brings higher cathode potential and helps increase the overall cell voltage; secondly, less HO$_2^-$ being produced can reduce the attacks on the catalyst and increase the durability.
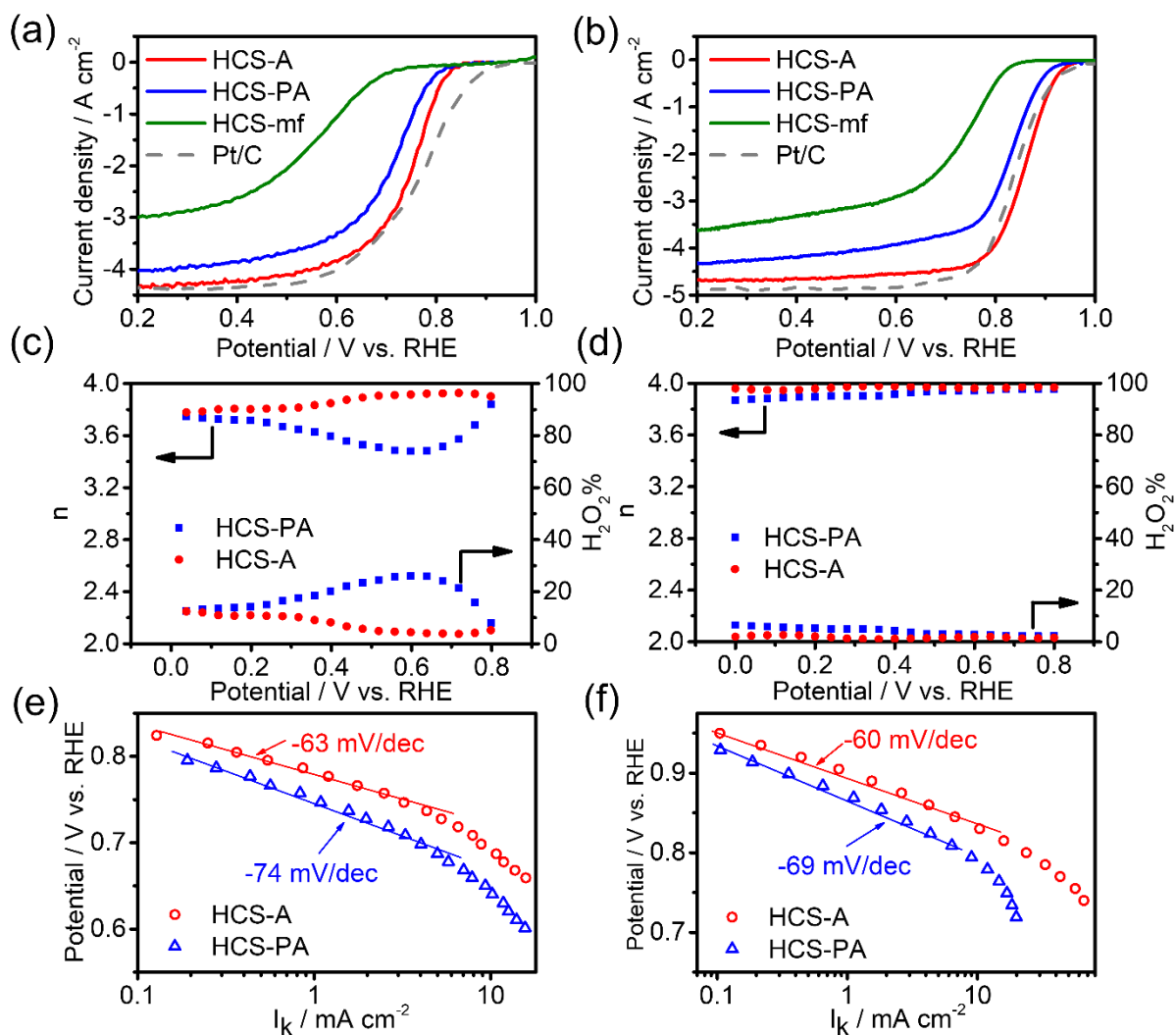
Figure 3- 4. RDE polarization curves of HCS-A, HCS-PA, HCS-mf and Pt/C in a) 0.5 M H_2SO_4 and b) 0.1 M KOH, rotating speed: 900 rpm, scanning rate: 5 mV cm^{-2}. Electron transfer number and peroxide species yield calculated for HCS-A and HCS-PA in c) 0.5 M H_2SO_4 and d) 0.1 M KOH. Tafel plots calculated for HCS-A and HCS-PA in e) 0.5 M H_2SO_4 and f) 0.1 M KOH.

As discussed previously, ATP was uniformly distributed on the HCS surface, thus HCS-A has more homogeneously distributed active sites on its surface than HCS-PA. Additionally, HCS-A has a larger surface area, which allows for more accessible active sites. Therefore, even though HCS-A and HCS-PA show similarities in composition, the polarization curves start to differentiate in the kinetic region. Tafel slopes for HCS-A and HCS-PA in both media are plotted to elucidate

the reaction kinetics for ORR (Figure 3-4 (e), (f)). A lower Tafel slope is desirable to drive a larger catalytic current density at a lower overpotential for a catalyst. As shown in the figures, Tafel slopes for HCS-A in acid and base are 63 mV/dec and 60 mV/dec, respectively. Comparing to the state of the art N-Fe-CNT/CNP catalyst reported in alkaline medium by Chung et al (-79 mV/dec),[133] HCS-A shows a lower Tafel slope in alkaline (-60 mV/dec), which means a faster reaction was obtained by HCS-A. As for HCS-PA, it has higher slopes (-74 mV/dec in 0.5 M H_2SO_4 and -69 mV/dec in 0.1M KOH) than HCS-A in both media, indicating a lower reaction rate than HCS-A in the kinetic region.
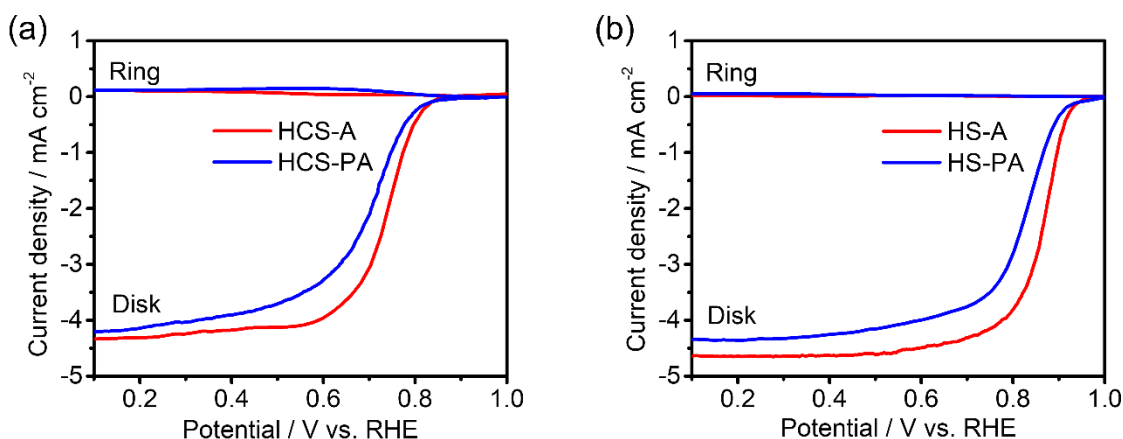
Figure 3- 5. RRDE polarization curves on disk and ring in a) 0.5 M H_2SO_4 and b) 0.1M KOH.

The studies in both acid and base offer us an opportunity to study the activity differences caused by the pH value. It was found that both of the two catalysts we prepared show higher activities in the base than in acid, which is commonly observed for non-precious metal catalysts. It has also been reported by hundreds of other papers that non-precious metal catalysts have higher activities in alkaline than in acid. Despite the high activities that have been reported many times in alkaline media, the origin of the activity difference caused by pH value remains unclear. From the results of the RRDE testing we know that the majority of O_2 molecules were reduced to H_2O through a 4 electron pathway in both media, which means reactions 3 and 4 dominate in both acid

and base, respectively. The standard electrode potential for reaction 3 and 4 are 1.229 V and 0.401 V vs. standard hydrogen electrode (SHE), respectively. If the reference electrode is transferred to a reversible hydrogen electrode (RHE), the standard electrode potential for reaction 3 is still 1.229 V since the effective concentration of H^+ is 1 mol L^{-1}. Meanwhile, the standard electrode potential for reaction 4 is $0.401 + 0.05916*pH$, in which the pH value for 1 mol L^{-1} OH^- is 14 and the standard electrode potential for reaction 4 can be calculated to be 1.229 V as well. Since thermodynamical reaction 3 and 4 give the same electrode potential, the activity difference between acid and base should not come from thermodynamics. A possible explanation forms the view of kinetics is that, in acidic medium, the protons in acid interact with the lone-pair electrons of the doped nitrogen atoms, which could hinder the charge transfer to the adsorbed oxygen.[134] As a result, the energy barrier for oxygen to gets electrons becomes higher and the reaction gets more sluggish than in alkaline medium.

3.3.3 Cycling durability and methanol tolerance study

As HCS-A demonstrated optimal ORR activities in both media, it was selected for durability, methanol tolerance, and full cell tests. To examine the durability of HCS-A, accelerated degradation testing (ADT) in the potential range of 0.6-1.0 V at a scan rate of 50 mV s^{-1} was performed for 10 thousand and 20 thousand cycles in acidic medium and alkaline medium, respectively. Figure 3-6 (a) shows the LSV curves for HCS-A before and after durability testing in acidic medium, demonstrating 34 mV downshift in half-wave potential with no notable change on the mass transport limiting current. LSV curves for HCS-A before and after durability testing in the alkaline medium is shown in Figure 3-6 (b). HCS-A only dropped 2 mV on its half-wave potential after 20000 cycles, which is, to our knowledge, one of the lowest activity loss (after 20000 durability cycles) reported so far.
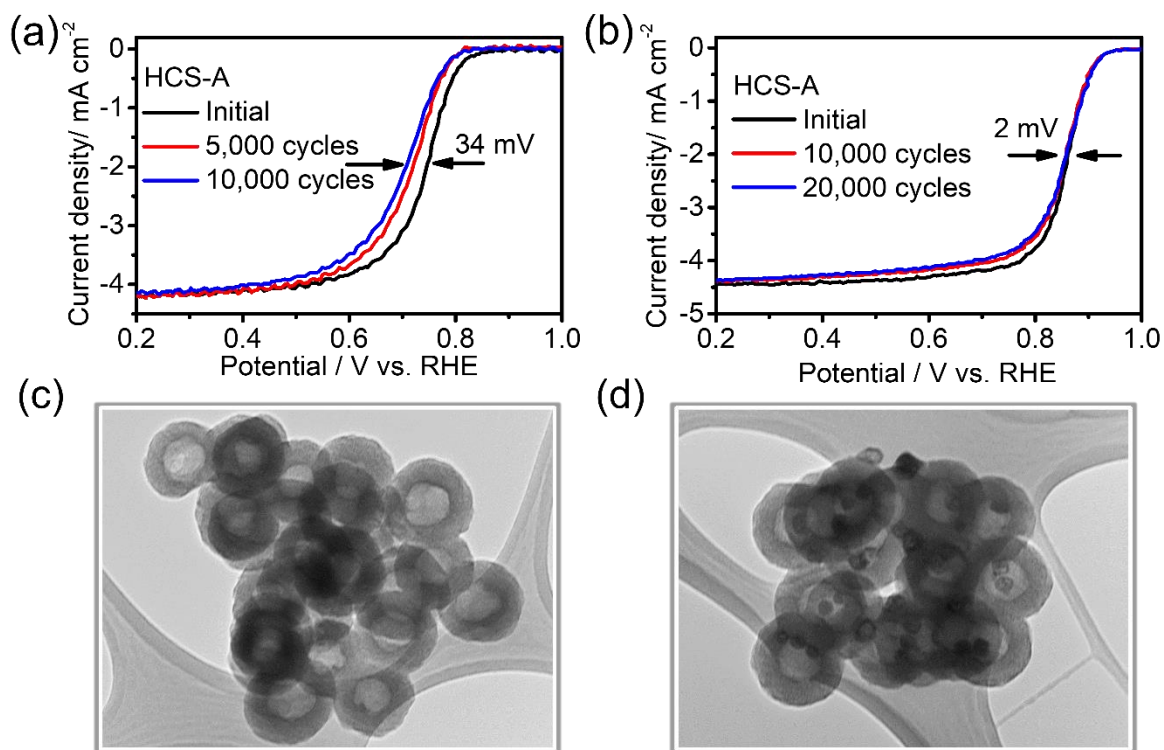
Figure 3- 6. LSV curves for HCS-A before and after cycling durability test in a) 0.5 M H_2SO_4 and b) 0.1 M KOH. TEM images of HCS-A after ADT in c) 0.5 M H_2SO_4, and d) 0.1 M KOH. Scale bar: 100 nm.

The sample after durability testing was collected from the electrode to study its morphological transformation. The TEM images for HCS-A after ADT in both acidic and alkaline media was shown in Figure 3-6 (c) and (d). It was discovered that HCS-A was able to preserve the hollow spherical structure in both media, which is reasonable since carbon was found to be relatively stable under the oxidation potential of 1.0 V vs. RHE. However, HCS-A after ADT in acid medium does not retain the iron particles that were decorated on its surface. The iron particles can synergistically catalyze the oxygen reduction process; such dissolution of iron particles in the acidic medium could be one of the main reasons for HCS-A activity degradation in acid. Another reason which could have caused the catalyst's activity to decline is the protonation of the nitrogen atom in the active sites.

The protonation introduces subsequent anion adsorption on the protonated nitrogen and leads to the ultimate deactivation of the active sites.[135] Also, as detected by RRDE, HCS-A has an H_2O_2 yield of 5% in the acidic medium. The H_2O_2 formed by the incomplete reduction of O_2 could result in the formation of hydroxyl free radicals ($\cdot OH$) under the promotion of Fe^{2+} following the reaction:[136-138]

$$Fe^{2+} + H_2O_2 + H^+ = Fe^{3+} + \cdot OH + H_2O \quad (7)$$
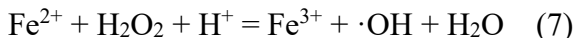
Both H_2O_2 and $\cdot OH$ were able to attack active sites and caused activity loss. Unlike in acidic medium, HCS-A after ADT in alkaline medium does not show considerable differences in morphology compared to the original material. The outstanding durability that HCS-A shows in the alkaline medium in contrast to the relatively poor durability in acidic medium can be attributed to three reasons. Firstly, the iron particles were more stable under alkaline conditions and were well preserved during the test. Secondly, protonation of active sites was greatly inhibited due to the lack of protons in the alkaline electrolyte. At last, H_2O_2 yield was much lower in alkaline, and its transformation to $\cdot OH$ was even less likely to take place without H^+.

It is well known that Pt-based catalyst can be poisoned by methanol, hindering its application in the cathode of direct methanol fuel cells (DMFCs). That is because platinum has a propensity to adsorb methanol and oxidize it to carbon monoxide (CO), in which the oxidation process simultaneously takes place with oxygen reduction,[139] thus reducing the cell voltage. Moreover, the CO by-product can poison the catalyst by occupying the Pt surface. In this work, we further studied the methanol tolerance ability of HCS-A by chronoamperometric measurements. As observed in Figure 3-7 (a) for the acidic medium, the ORR current at 0.6 V vs. RHE does not show much difference after methanol was added to the electrolyte at 2000 s, to a resulting methanol concentration of 3 M. In contrast, commercial Pt/C catalyst shows significant

activity drop as its ORR current has endured a current loss of ca. 60% after methanol was added to the solution. In the alkaline medium (Figure 3-7 (b)), after methanol was added to the electrolyte, Pt/C shows dramatic current drop to a value around zero and slowly recover to ca. 40% of its original current. On the other hand, HCS-A maintained its current and was barely influenced by the methanol.
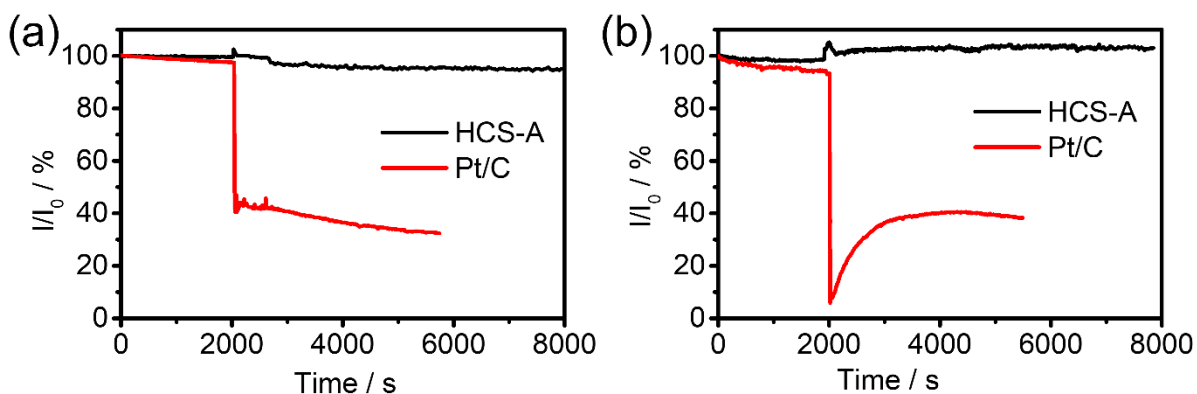
Figure 3- 7. Chronoamperometric responses for the HCS-A catalyst and commercial TKK 46.6 wt% Pt/C catalyst obtained at 0.6 V vs. RHE in a) 0.5 M H_2SO_4 and b) 0.1 M KOH with the addition of methanol (resulting concentration of 3 M) at 2000 s.

3.3.4 PEM fuel cell and zinc-air battery test

To further verify the ORR activity for HCS-A, fuel cell tests were performed in a single cell using a condition-controlled fuel cell test station (Scribner 850e). A set of membrane electrode assembly (MEA, top left), single-cell (top right) and testing system (bottom) used in our work are shown in Figure 3-8 (a) to exemplify the experiments. The schematic in Figure 3-8 (b) illustrates the fuel cell working mechanism with HCS-A as the cathode catalyst. A maximum fuel cell power density of 500 mW cm^{-2} was obtained in a single cell test (Figure 3-8 (c)), which is quite a decent performance for non-precious metal catalyst supported PEM fuel cells. For the testing in alkaline medium, a home-made zinc-air battery was designed to test the ORR activity of HCS-A. Figure 3-

8 (d) shows the gas diffusion layer sprayed with a layer of HCS-A (top figure) and the assembled zinc-air battery cell (bottom figures). The zinc-air working mechanism with HCS-A as the cathode
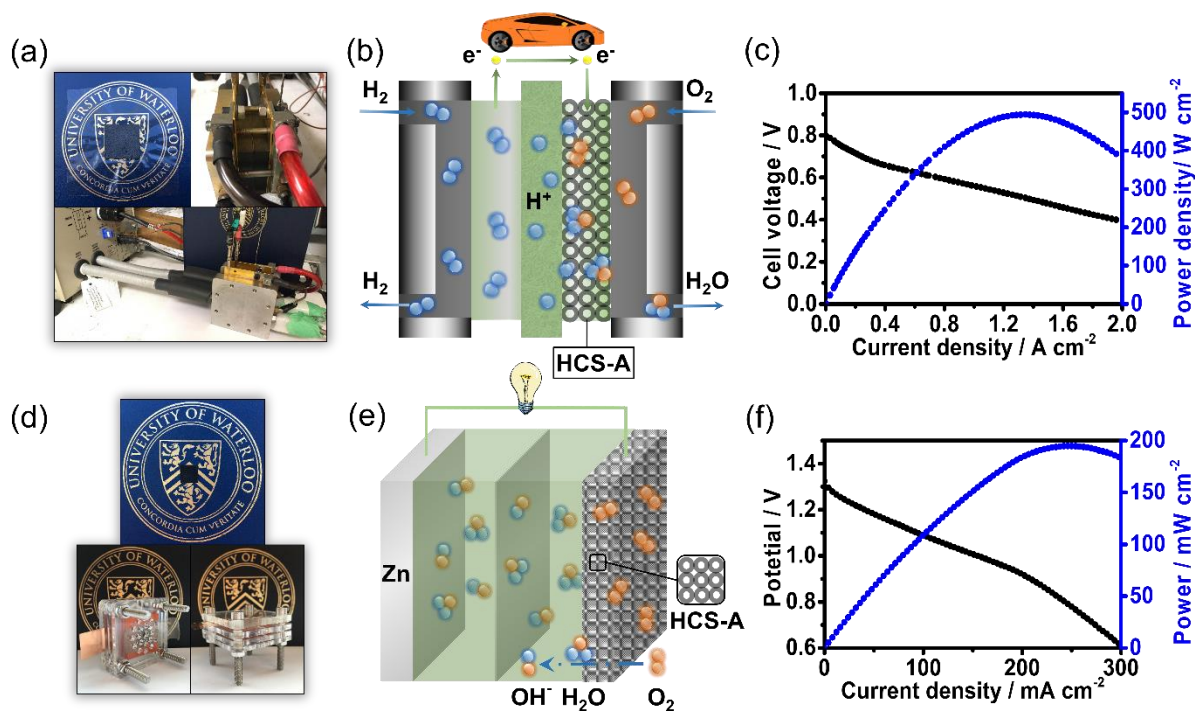
Figure 3- 8. Photograph of a) fuel cell and d) homemade zinc-air battery. Schematic illustration of b) fuel cell and e) zinc-air battery. Cell voltage and power density plots with HCS-A cathode for c) H_2-O_2 fuel cells and f) zinc-air battery in ambient air.

catalyst is illustrated in Figure 3-8 (e). In our experiment, to simulate a real operating condition, the zinc-air battery was tested in ambient air with no O_2 pre-bubbling or continuous O_2 flow. The battery reached a maximum discharge power density of 195 mW cm^{-2} (Figure 3-8 (f)), which is among the best zinc-air performances obtained in ambient air to date.

3.4 Conclusion

In this paper, we have designed an ultra-high surface area hollow carbon sphere (HCS). With this HCS as the carbon support, two types of heteroatom doped catalyst HCS-PA and HCS-A were prepared with aminothiophenol and poly-aminothiophenol, respectively, as the doping

agent. It was manifested that both of these, monomer and polymer, acting as heteroatom doping precursors, were able to increase ORR activity. However, the monomer, aminothiophenol, could be a better choice to obtain favorable morphology and surface area retention of the ultra-high surface area spherical supporting material. With the obtained unique embellished hollow sphere structure and high surface area, HCS-A showed remarkable ORR activity in both acidic and alkaline media. In addition to outstanding ORR activity, HCS-A also demonstrated excellent durability with negligible degradation after 20000 cycles in alkaline medium. PEM fuel cell test with HCS-A as a cathode catalyst reached a peak power density of 500 mW cm^{-2}. In a zinc-air battery test, the discharging power density of HCS-A reached a maximum of 195 mW cm^{-2} in ambient air, which is one of the best zinc-air performances reported in ambient conditions. Our study not only reports a catalyst with high activity but more importantly validates a strategy to maintain the structural advantages from a favorable supporting material.

Chapter 4 Commercial-Scale Synthesis of Dual Nitrogen Doping PGM-free Catalyst for PEM Fuel cells

4.1 Introduction

In chapter three we applied nitrogen and sulfur co-doping precursor and prepared the PGM-free catalyst with ultra-high surface area carbon support. Even though we were able to achieve decent half-cell activity, zinc-air battery performance, and fuel cell performance, there is still a long way to go for the HCS-A catalyst to compete with the state of art catalysts in acidic medium. The HCS-A catalyst, even though has a high surface area, is not well graphitized and some of the inside surfaces of the hollow sphere can not be utilized. Since the goal of our research is to prepare the state of art PGM-free catalyst for PEM fuel cells, the catalyst has to show activity that is high enough to be comparable to the best catalysts that have ever been reported, especially in acidic medium.

There are plenty of methodologies that have been reported to prepare PGM-free catalysts in the past decades, and many varieties of precursors (iron and nitrogen) have been used. In order to obtain the catalyst with high ORR activity, the precursors must be carefully selected. Iron, despite its side effect as an essential part of Fenton reagent, has been well known to be the best transition metal in terms of the activity. The selection of nitrogen precursor is more challenging because the choices are much more than transition metal precursors. Nitrogen-containing organic materials are the most often used nitrogen precursor. A rough method to decide if the nitrogen precursor can be a good candidate is to look at the nitrogen/carbon ratio of the molecular. Generally, the more nitrogen-rich (high N/C ratio) the precursor is, the more effective nitrogen doping can be achieved. In the extreme case, NH_3 is a effective nitrogen doping agent for PGM-

free catalyst synthesis, where there is no carbon in the molecule.[140-142] However, NH_3 is generally used as a post-treatment nitrogen doping agent as carbon is also necessary for a catalyst. Besides the N/C ratio, it is also critical that the nitrogen precursor must be able to be carbonized instead of evaporating; otherwise, it will be exhausted rather than composing the active sites. Polyaniline has been used as the nitrogen precursor in many publications and proved to be one of the best candidates to synthesize highly active catalysts.[143-145] Because of the abundant benzene rings within the structure, polyaniline is likely to get graphitized after heat treatment and result in high conductivity. It is also nitrogen-rich, with an N/C ratio of 1/6. In this chapter, we selected polyaniline as the nitrogen precursor and the iron chloride as the transition metal precursor.

In addition to the primary nitrogen precursor, a secondary nitrogen precursor is added into the mixture right after aniline polymerization. Fu et al. used polyaniline and phenanthroline as dual nitrogen sources and obtained an abundance of 3D porous graphene-like structures.[38] The unique structure could host a high population of reactant-accessible active sites for the ORR and facilitate mass transport as well. Leonard and coworkers used cyanamide, melamine, urea, and nicarbazin as the secondary nitrogen precursors, and demonstrated that the intrinsic activity of active site and the utilization of the active site compensate each other.[40] The additional doping of nitrogen not only increases the population of active sites but also enhances the intrinsic activity of each site. Here we selected urea as the secondary nitrogen precursor because it has a nitrogen/carbon ratio of 1:1 which is beneficial for nitrogen doping. The primary nitrogen precursor polyaniline will be partially graphitized and partially decomposed during the pyrolysis. Meanwhile the urea also decomposes to create micropores and release ammonia to enhance the nitrogen doping in the catalyst.[146-148] When there is more nitrogen doping in the catalyst, there are more sites to hold iron atoms to form the ORR active sites.[149-151] In this chapter, we also selected a well established and

relatively simple method for the synthesis process so that the catalyst can be easily prepared in large scale.

4.2 Materials and methods

4.2.1 Catalyst synthesis

The PAU catalyst was synthesized according to the following steps: Step 1, prepare a ca. 2 M HCl solution by adding 50 mL of concentrated HCl to 200 mL of DDI water. Step 2, Pipette 3 mL of aniline into the 250 mL HCl solution and continuously stir throughout the entire process. Step 3, add 5.0 g urea and 5.0 g $FeCl_3$ into the above solution, Step 4, add 5.0 g ammonium persulfate (APS) as an oxidant to polymerize the aniline in the above solution. Continue rigorously stirring at room temperature for at least 3 hours to allow full polymerization of the aniline. Step 5, Pipette 400 mg of the HNO_3, treated KJ300 suspension slowly into the polyaniline mixture. Maintain stirring of the solution for 48 hours as rigorously as possible at room temperature. Step 6, After 48 hours of constant stirring, the liquid from the mixture is removed by evaporation by heating the solution to ca. 70 °C. Step 7, Collect the solid material and grind it into powder. Step 8, Heat-treat the catalyst sample at 200 °C for 1 hour in Ar atmosphere and grind it again until the powder is as fine as possible. Step 9, the subsequent heat-treatment for the resulting powder is performed at 1000 °C in Ar atmosphere for 1 hour. Step 10, the sample was taken from the furnace and subsequently leached in 300 mL 0.5 M H_2SO_4 at 80 - 90 °C for 8 hours. Filter and wash the samples with DDI until neutral and dry in a vacuum oven at 80°C overnight. Step 11, the dried sample was then heated again at 1000 °C in an inert atmosphere for 1 hour to further improve the ORR activity and to remove surface functional groups.

For the synthesis of the PA catalyst, 5.0g urea was not added. For the synthesis of SU-PA and SU-PAU catalysts, the same procedure with PA and PAU was applied, but with a larger amount of raw materials.

4.2.2 Electrochemical measurements

RDE and RRDE measurements were performed using a CHI Electrochemical Station (Model 750b) in a standard three-electrode cell. For RDE, a 5.0 mm diameter glassy carbon disk (disk geometric area 0.196 cm^2) was used. The RRDE has an extra Pt electrode with an inner diameter and outer diameter of 6.5 mm and 7.5 mm (ring geometric area 0.110 cm^2). To avoid any potential contamination of the catalyst by Pt, all experiments were carried out with a graphite rod as a counter electrode. Reversible hydrogen electrode was used as the reference electrode. The catalyst ink was prepared by adding 5 mg of the catalyst to 1 ml isopropanol and ultrasonically blending for 30 min. 20 μl of the ink and 3 μl of 0.25 wt.% Nafion solution was applied to the 0.196 cm^2 disk in sequence, resulting in a catalyst loading of ca. 0.5 mg cm^{-2}. RDE polarization plots were recorded in both O_2-saturated and N_2-saturated electrolytes at a scan rate of 5 mV s^{-1}.

4.2.3 Physicochemical characterization

A MiniFlex 600 Rigaku Diffractometer with Cu Kα irradiation ($\lambda = 1.5406$ Å) was used to record XRD patterns. Raman spectra were collected by WiTEC alpha300R with a 532 nm solid laser as an excitation source. Brunauer-Emmett-Teller (BET) surface area was measured by the nitrogen adsorption and desorption technique through a Micromeritics ASAP 2010M system. X-ray photoelectron spectroscopy (XPS) was performed with a Thermal Scientific K-alpha XPS spectrometer to collect the elemental composition of the catalyst materials.

4.2.4 Half catalyst coated membrane (CCM) preparation

Step 1, prepare the ink using a weight ratio of catalyst: isopropanol : water: Nafion(5 wt.%) of 1: 12: 12: 11. For loading of 4 mg cm^{-2}, prepare ink using ca. 40 mg catalyst. If using different wt.% Nafion solutions, adjust this amount accordingly. Step 2, sonicate the ink for at least 1 hour and let it sit overnight. The next day, sonicate for one more hour before painting the catalyst ink onto the membrane. Step 3, place a dried membrane on a sheet of Teflon mesh sitting on the room temperature vacuum table. Place a 5 cm^2 square (2.23 cm $\times$ 2.23 cm) Teflon sheet (the gasket material) on the center of the membrane. Step 4, lay down the Teflon cover to achieve complete suction with the vacuum. There should be a square slightly larger than 5 cm^2 cut into this Teflon cover. Step 5, using Teflon coated fiberglass tape, tape the cover sheet to the exposed areas of the membrane, and then remove the 5 cm^2 Teflon sheet square template, exposing the 5 cm^2 area of the membrane to be painted. Step 6, heat the vacuum table to 80 °C. Once it reaches the temperature, painting can begin. Step 7, paint the prepared catalyst ink onto the exposed area of the membrane, using smooth strokes across. Vary directions to achieve the coating as uniform as possible over the entire area. Step 8, after painting all of the ink, allow the catalyst coated membrane to dry for ca. 1-2 hours. Step 9, after completely dry, turn off the heat and remove the tape holding the membrane to the Teflon sheet cover.

4.2.5 Membrane electrode assembly (MEA) assembly

Step 1, cut a piece of commercial anode GDE into a 5 cm^2 square. Place it on top of the bottom Teflon sheet (catalyst facing upwards). Place a dried membrane on top. Change gloves after handling the Pt anode to avoid contamination. Step 2, take the catalyst coated membrane (catalyst facing up) and place it on top of the anode and membrane prepared in the previous step. Align the anode and painted catalyst. Step 3, place a commercial gas diffusion layer (BC 25) on

top of the painted catalyst. Step 4, Place the Teflon sheet/rubber/sheet/metal plate on top. MEA hot pressing will be done between two metal plates, two pieces of orange rubber sheets, and two Teflon sheets, in a sandwich-like configuration. Step 5, press at 120 °C for 5 minutes, using a pressure of 600 pounds for a 5 cm^2 MEA. For higher areas, increase the pressure proportionally. Step 6, after pressing, take the entire sandwich and place it under a weight and allow it to cool.

4.3 Result and discussion

4.3.1 Half-cell activity tests

It has been discussed in chapter 3, that the secondary sulfur doping improves the activity of PGM-free catalysts. Besides sulfur, other heteroatoms such as boron and phosphorus have been applied as primary or secondary doping atom to obtain PGM-free catalyst.[152-155] However, nitrogen is still the best primary doping heteroatom for PGM-free catalyst so far. Consider that nitrogen has been proved as the best choice for heteroatom doping, we tried to still use nitrogen as the secondary doping atom in addition to the primary nitrogen doping. It has also been reported by other literature that secondary nitrogen doping enhances the PGM-free catalyst activity. In addition to high activity, the catalyst should be easy to scale up and cost-effective as well. In this regard, we have selected urea as a cheap and nitrogen-rich doping agent for secondary nitrogen doping. Urea has one of the highest nitrogen to carbon ratio (1:1) among the nitrogen precursors. The high nitrogen to carbon ratio is beneficial for effective nitrogen doping because, for a given amount of precursor, a higher N/C ratio provides more nitrogen.

In Figure 4-1 (a) we can easily observe that the sample with secondary nitrogen doping by urea (PAU) shows higher activity than the one without secondary doping (PA). The half-wave (at 2 mA cm^{-2}) potential of PAU increased by 22 mV as compared to PA. To make highly active ORR

catalysts, the samples have to go through graphitization, nitrogen doping, micropore formation, iron-nitrogen coordination bond formation, et. al. These processes cannot take place at low temperatures because they are thermodynamically unfavorable at low temperatures. High-temperature supplies high energy to overcome the energy barriers and allow the demanded changes in the catalyst to take place. The effects of heat treatment temperature have been intensively studied in the literature.[156-158]
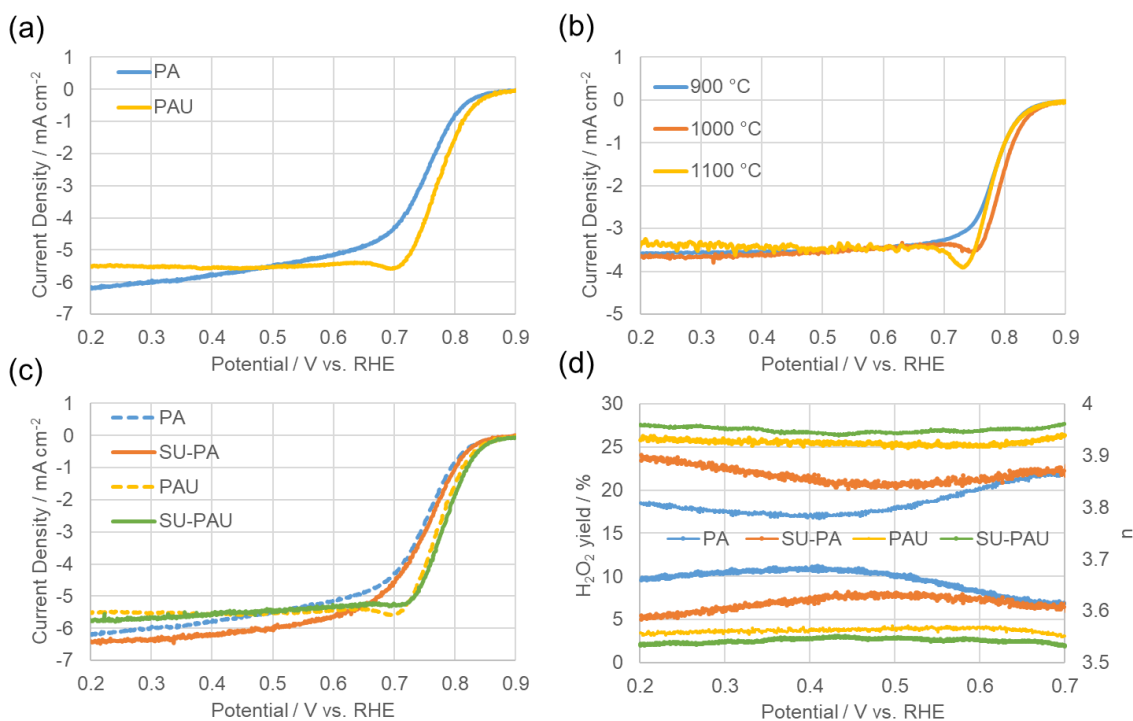
Figure 4- 1. Half-cell linear sweep voltammetry test of (a) PA and PAU, (b) PAU heat-treated by different temperatures, (c) PA, SU-PA, PAU, and SU-PAU. (d) Electron transfer number and H_2O_2 yield of PA, SU-PA, PAU, and SU-PAU. Sweep rate: 10 mV s^{-1}, Electrolyte: 0.1M HClO$_4$, Rotating speed: 1600rpm for (a), (c), and (d); 900 rpm for (b).

Generally, if the temperature is too low, the carbon graphitization won't be sufficient, and the active sites won't be effectively formed. On the other hand, if the temperature is too high, the active sites can be decomposed because the nitrogen-carbon bonds can be broken when the temperature is high enough. For PGM-free catalyst prepared by different methods, the optimal

temperature can be altered accordingly. Here, we are not going to do much in-depth study on how the temperature may affect the active sites and activity. Instead, we have made a simple activity comparison to find the best temperature for PAU. The results are shown in Figure 4-1 (b), which we can see 1000 °C is the optimal heat treatment temperature for PAU.
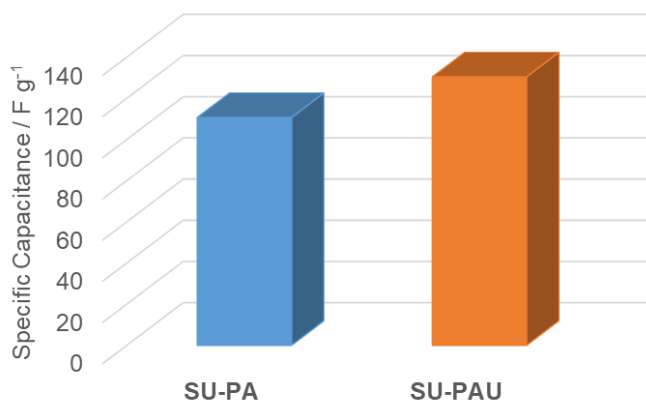
Figure 4- 2. The specific double-layer capacitance of SU-PA and SU-PAU.

In this work, we aimed to fulfill large-scale catalyst synthesis without any diminishing in the ORR activity. After successfully enlarge the scale of each batch from 100-milligram level to 10-gram level, we have testified the activity of the scaled-up catalyst. It is found in Figure 4-1 (c) that the scaled-up counterparts of PA and PAU, namely SU-PA and SU-PAU, both show higher ORR activity than PA and PAU. Half-cell testing results show that rather than diminish the ORR activity, scale-up improved the activity for both primary doped and secondary doped catalyst instead. We also performed the rotating ring disk electrode (RRDE) test in half-cell to study the catalytic selectivity of the catalysts. Figure 4-1 (d) shows the H_2O_2 yield and electron transfer number of PA, SU-PA, PAU, and SU-PAU. It is shown both secondary nitrogen doping and scale-up has a positive effect on the catalytic selectivity. In both ways, the catalysts have more preference on the 4-electron transfer full reduction to water than 2-electron transfer partial reduction to H_2O_2. Expectably, the selectivity results are consistent with the activities shown in Figure 4-1 (c) and (d).

There remains a puzzle of how secondary doping improves the ORR activity of the PGM-free catalysts. When we did CV curves of the catalysts in the nitrogen atmosphere, it is observed that SU-PAU has higher double-layer capacitance (DLC) than SU-PA (Figure 4-2). Since both of these catalysts are iron and nitrogen-doped carbon material in their chemical property, the difference in DLC should come from their electrochemical accessible surface area. This reason can be true because if SU-PAU has more surface area for electrochemical reactions, that means it can provide more active. For further verification, we increased the SU-PA loading by 25% to 1.25 mg cm^{-2} and tested the ORR activity. In Figure 4-3 (a) it can be seen that SU-PA with increased loading is showing slightly higher DLC than SU-PAU. In contrast with the DLC, SU-PA doesn't show much improvement in the ORR activity. By physically increasing the catalyst loading of SU-PA, to make the SLC comparable to SU-PAU doesn't improve its ORR activity comparable to SU-PAU.
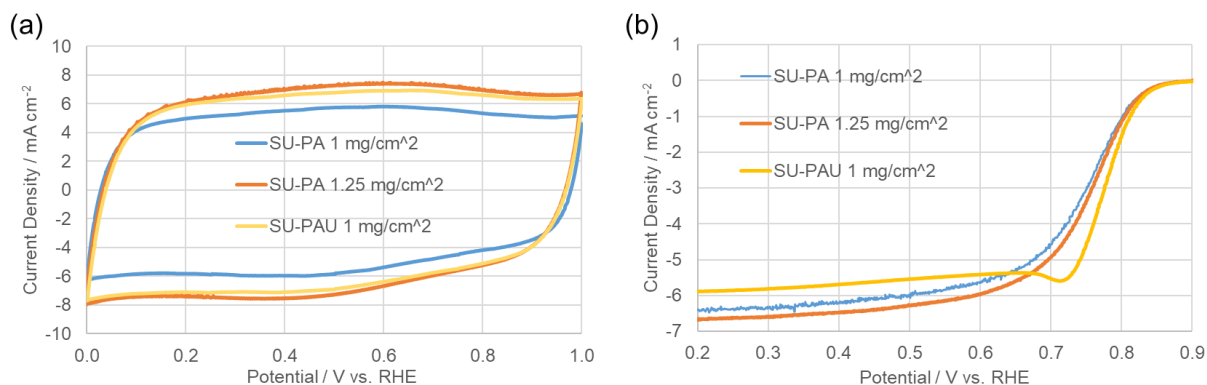
Figure 4- 3. CV curve of SU-PA at 1 mg cm^{-2}, SU-PA at 1.25 mg cm^{-2} and SU-PAU at 1 mg cm^{-2}, in the nitrogen atmosphere. Sweep rate: 50 mV S^{-1}. (b) LSV curve of SU-PA at 1 mg cm^{-2}, SU-PA at 1.25 mg cm^{-2} and SU-PAU at 1 mg cm^{-2}, in the oxygen atmosphere. Sweep rate: 50 mV S^{-1}. Rotating speed: 1600 rpm.

4.3.2 Physico-chemical measurements

To get a better understanding of how the secondary nitrogen doping improves ORR activity, it is necessary to get more in-depth information from other characterizations. Since

successful scale-up has been achieved, we targeted SU-PA and SU-PAU as the focus of our study. X-ray Powder Diffraction (XRD) shows similar diffraction patterns for SU-PA and SU-PAU, which are both typical graphitized carbon material (Figure 4-4 (a)). No sharp peaks can be observed for either PA or PAU, suggesting a fairly effective washing out of crystalline metallic species. In previous research, Nathaniel et al. have reported repeating acid washing and pyrolysis steps to fully wash out the metallic impurities.[40] In this research, we found that several times of acid washing after first pyrolysis step were adequate to remove the metallic impurities.
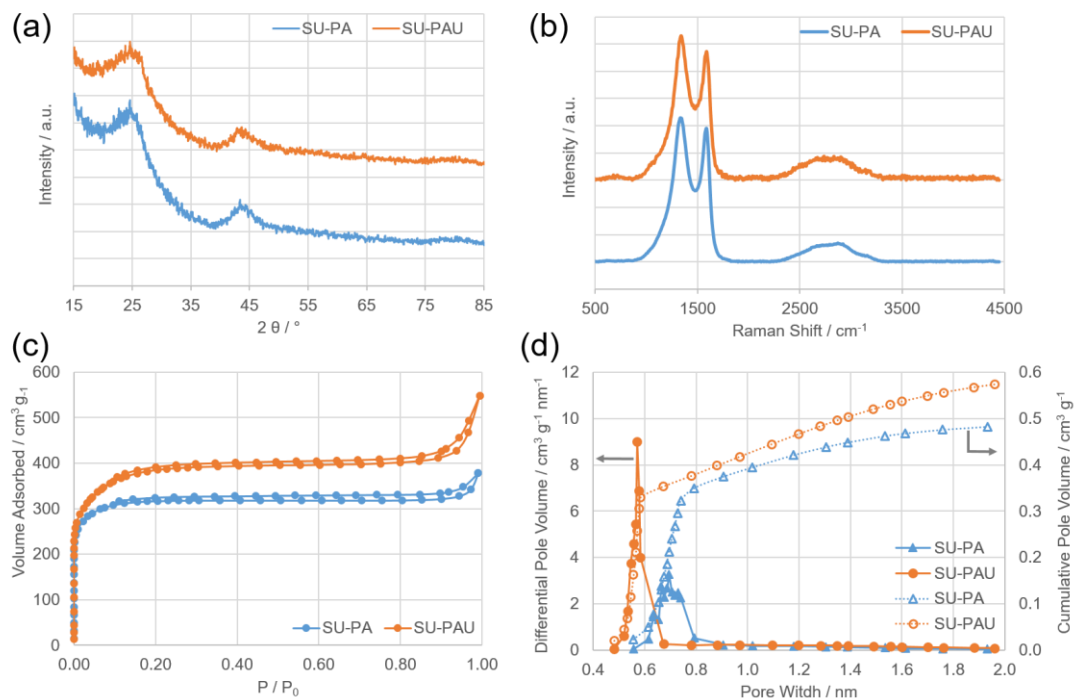
Figure 4- 4. (a) X-ray diffraction (XRD) pattern, (b) Raman spectra, (c) Nitrogen adsorption and desorption isotherms, and (d) pore size distribution of SU-PA and SU-PAU.

Raman spectroscopy was performed to study graphitization information of SU-PA and SU-PAU, as shown in Figure 4-4 (b). Similar Raman patterns show the similarity in their graphitization and defects, which is reasonable because both of them were originated from iron and polyaniline, and have gone through the same treatment processes. However, SU-PAU shows a slightly higher

I_g/I_d ratio compared to SU-PA, indicating a higher degree of defects. Increased defects can be one of the reasons that contribute to higher ORR activity.[159-161] During the heat treatment process, urea decomposes at high temperature and becomes NH_3 and HNCO, both of which can act as nitrogen doping agents to create more defects to the carbon material.[162-165]

As a secondary nitrogen precursor, urea not only creates defects but also creates micro poles. Nitrogen adsorption and desorption curve are displayed in Figure 4-4 (c).Sharp increases at P/P_0 close to zero implies large contents of micro poles for both SU-PA and SU-PAU. Comparing to SU-PA, SU-PAU has a higher adsorption volume in total, and that means it has a higher specific surface area than SU-PA. The surface area calculated with the application of the multipoint Brunauer-Emmett-Teller (BET) model for SU-PA and SU-PAU is 963 m^2/g and 1147 m^2/g, respectively. The pore size distribution was calculated based on Horvath-Kawazoe (H-K) method as shown in Figure 4-4 (d). SU-PA shows a narrow pore size distribution between 0.6 and 0.8 nm, with a peak maximum at around 0.7 nm. SU-PAU is found to possess smaller pore sizes, distributed in the range of 0.5-0.7 nm with a peak maximum at 0.6 nm. Narrower pores of SU-PAU suggest that urea has helped to create micropores during the pyrolysis, which can be based on either/all of the following three mechanisms: 1. Urea took up some spaces in the material before pyrolysis, and the spaces become micro pores after urea decomposition; 2. The decomposition products in the gas phase escape from inside of the material to outside and create micro pore paths, which is similar to a dough leavening process; 3. The decomposition products, NH_3 and HCNO, etch the carbon framework and introduce pores. Still, more works need to be done in the future if the reason/reasons dominating need to be sorted out, but it can be concluded from the nitrogen adsorption-desorption results that adding urea contributes to creating micropores. As has been intensively studied (more discussion. ref here), the micropore is very important for PGM-free ORR

catalysts to hold the active sites, improved microporosity of SU-PAU can be another reason contributing to its ORR activity.
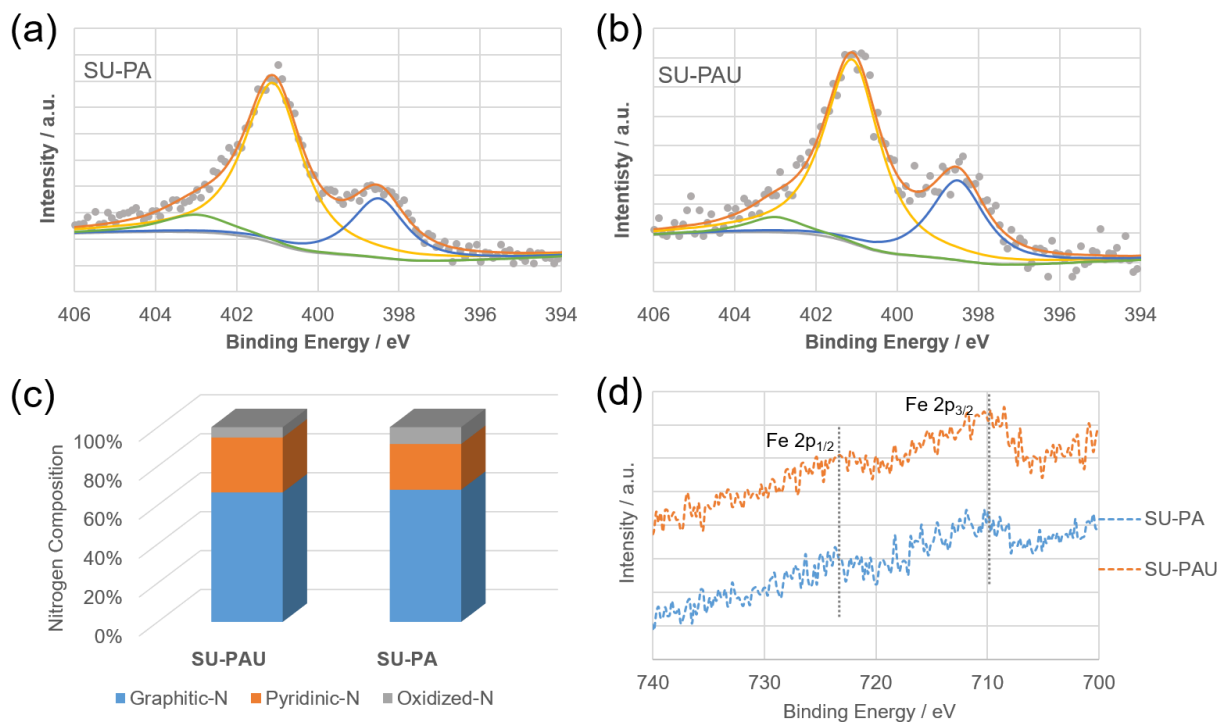
Figure 4- 5. XPS N 1s spectra of (a) SU-PA and(b) SU-PAU. (c) Nitrogen species composition of SU-PA and SU-PAU. (d) Fe 2p spectra of SU-PA and SU-PAU.

Nitrogen species are studied by x-ray photoelectron spectroscopy (XPS) to understand how the secondary doping agent may affect the active sites. Similar N 1s patterns can be observed for SU-PA and SU-PAU, with a prominent peak at around 401 eV and a weaker one at around 398.5 Ev (Figure 4-5 (a) and (b)). Some works have reported that Me-N_X (Me = metal) bond can be deconvoluted at a peak position centered at ca. 399 eV. In this work, a reasonable peak deconvolution can only fit in three types of nitrogen: pyridinic nitrogen (~398.5 eV), graphitic nitrogen (~401eV) and oxidized nitrogen (~403 eV). Still, Fe-N_X bond is believed to exist in both SU-PA and SU-PAU, since the ORR activity is much higher than that can be reached solely by metal-free sites in acidic medium. However, the nitrogen bonds with iron are overlapping with

other types of nitrogen, thus cannot be separated. Based on previous researches, Fe-N$_X$ peak is likely to overlap with pyridinic type because the bond energy between these two types is very close. The reason behind this is that iron in the active center is believed to bond with pyridinic nitrogen (Fe-N$_{pyridinic}$).[166-168] In this case, the nitrogen is still pyridinic type, but the electron energy in N 1s orbital is slightly higher than its routine state, because of the excitation of the electrons by iron.[169] Other than bonds with pyridinic nitrogen, iron is still possible to bond with graphitic nitrogen which has rarely been reported.[170] In the latter case, N 1s peak in Fe-N$_{graphitic}$ bond is possible to locate at slightly higher than 401 eV and overlaps with graphitic nitrogen. Iron 2p patterns of SU-PA and SU-PAU has been tested but not deconvoluted due to the low iron content and high noise to signal ratio (Figure 4-5 (d)). Despite the noise, a stronger iron peak still can be observed for SU-PAU, indicating higher iron content in SU-PAU than in SU-PA. As we know, XPS is a technique that is only capable of detecting the surface (< 10 nm) of carbon material.[171] Since both SU-PAU and SU-PA have been completely acid washed to remove surface iron granules, the remaining iron at the surface should mainly come from the Fe-Nx sites. As a result, we know by adding urea iron doping for SU-PAU can be enhanced, and the content of Fe-Nx bonds increases. There is an interesting finding that urea increased the iron content of SU-PAU by doubling it but only increased nitrogen content very little. A reasonable explanation is urea enhanced iron doping by providing a nitrogen-rich environment at the early stage of pyrolysis. However, accompany the temperature reaching high (1000 °C) and holding for a long time, extra nitrogen will be decomposed, and total nitrogen content has a ceiling (ref here).

4.3.3 Single-cell performance

The purpose of developing the PGM-free ORR catalyst is to put them into real applications. We have incorporated the catalysts into the cathode catalyst layer of 5 cm^2 MEAs. The MEA

performance is shown in Figure 4-6, from which it can be observed that SU-PAU has the best single-cell performance, followed by PAU. Observing that both SU-PAU and SU-PA have better performance than PAU and PA, respectively, it can be concluded that the secondary nitrogen doping benefits the catalyst in its fuel cell performance. The fuel cell performance is also consistent with the electrochemical activities that were measured in half cells that the catalysts follow the same order in fuel cell performances and half-cell activities. At the low current density region where kinetic loss dominates, SU-PAU shows less voltage loss than PAU, followed by SU-PA and PA. As the current density becomes higher and the polarization curves reach to ohmic loss region, the performance gaps between these samples increase. Since it was discussed previously that the secondary doping increases specific area, SU-PAU and PAU should both have a higher contact area with the ionomer thus less ohmic resistance. For this reason, SU-PAU and PAU showed much less voltage drop at the ohmic loss region. SU-PAU shows evidence of mass transport issues at the high current density region, which can be solved through the optimization of catalyst layer design. We will have more work to be done on the catalyst layer design in the next chapter.
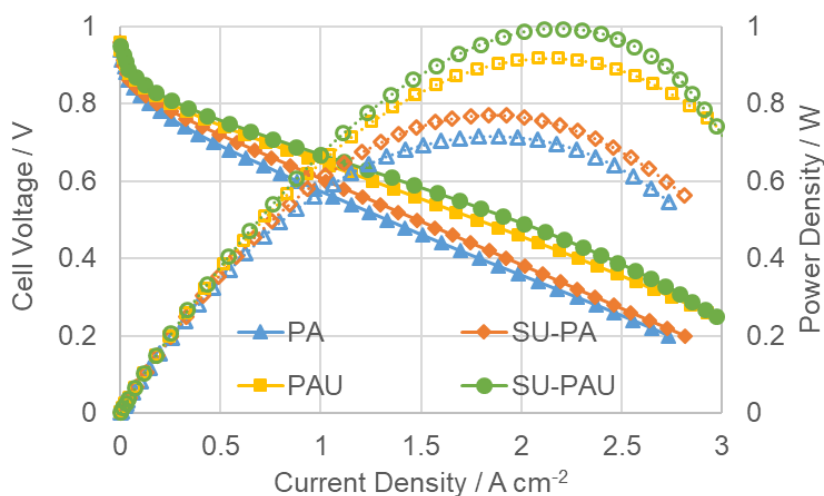
Figure 4- 6. H_2-O_2 fuel cell performance of PA, SU-PA, PAU, and SU-PAU. Backpressure: 1.5 Bar for both anode and cathode.

4.4 Conclusions

In this work, we have synthesized highly active PGM-free ORR catalysts by secondary nitrogen doping and successfully scaled up the catalyst without diminishing the activity. Half-cell electrochemical testing proved that the secondary nitrogen doping increased both ORR activity and selectivity. Increasing the catalyst loading didn't bring much improvement in the ORR activity of the primary doped catalyst (SU-PA). Even though by increasing the loading, SU-PA has comparable DLC with SU-PAU, its ORR activity is still inferior, indicating the benefits of secondary doping can't be achieved by simply increasing the accessible electrochemical area. Raman spectra show that secondary nitrogen doping increased the defect level of the catalyst. Nitrogen adsorption-desorption isothermal curve and pore distribution tell us the secondary nitrogen doping increased the specific surface area and created more micropores within the catalyst. XPS results proved that the secondary nitrogen doping removed some of the oxidized nitrogen species and enhanced the formation of iron-nitrogen coordination in the active sites. Because of the reasons mentioned above, secondary nitrogen doping not only shows higher ORR activity in half-cell testing but also proved its advanced performance in fuel cell testing. We have achieved a peak power density of 1 W cm^{-2} on a single-cell with SU-PAU as the cathode catalyst.

Chapter 5 Systematic Study of Fuel Cell Testing Parameters and MEA Design Optimization

5.1 Introduction

Upon successful large-scale-synthesis of the highly active catalyst SU-PAU and receiving excellent performance in the small-size MEA under hydrogen-oxygen condition, it is worthwhile to move forward to larger size MEA test under hydrogen-air condition. Aiming at achieving the best performance, the study of different operating parameters and optimization of catalyst layer/MEA design becomes important. As we have discussed in chapter one that there are different stages of losses in the polarization curve of a PEM fuel cell, and those losses can be affected by a lot of factors from both the MEA design and the operating conditions. It is crucial to minimize losses by working on these two factors. Before that, the operation mechanism of the fuel cell must be clear. In a typical fuel cell, there are three pipelines that supply fuel, oxidant, and coolant, respectively. In order to get a high quality of the distributions of those three supplements, the bipolar plates and MEA both must be well designed. Bipolar plate design is beyond the scope of this study, and we will be focusing on the MEA. Take the example of cathode, after the oxidant, namely air, being well distributed by the flow channels on the bipolar plates, it has to diffuse through the gas diffusion layer (GDL) to get better distribution. After pathing through the GDL, the oxidant comes to the cathode catalyst layer (CCL), where the oxygen reduction reaction (ORR) takes place. However, ORR doesn't happen right away at the boundary between GDL and CCL, because there are other two reactants required for the ORR, protons, and electrons. Electrons come from the bipolar plates and the GDL, which both must be made of materials with high electron conductivity. The high electron conductivity ensures a fast supplication of electrons, which usually

is not a problem at the GDL and CCL boundary. The protons come from the anode, which is originated from hydrogen oxidation, follow by transferring through the proton exchange membrane to the CCL. If the protons want to get from the membrane/CCL boundary to the CCL/GDL boundary, they have to travel through the entire CCL, which is very difficult especially for a thick CCL when PGM-free catalyst is applied. Instead, both the oxidants and the electrons travel through CCL to the CCL/membrane boundary to join the protons and produce pure water as the product.

In order for the above-mentioned process to go on smoothly, the oxidant gas, electrons, protons, and water must be well managed and balanced. The electrons shouldn't be blocked by any material with poor conductivity; the catalyst layer and catalyst should be porous for the oxidant gas to transfer through; The protons transport should be efficient within both membrane and CCL; Water that is produced by the oxygen reduction reaction should be successfully removed to avoid flooding in the CCL. In this chapter, we have tested the fuel cell under different operation conditions to study how operating temperature, RH, pressure, oxygen concentration, and oxygen stoichiometry affects the performance. Design parameters such as catalyst loading, ionomer content, ionomer type, and membrane type were also studied to see their effects on the performance, as well as optimize the MEA design.

5.2 Material and Methods

5.2.1 Material synthesis

The SU-PAU catalyst was synthesized according to the following steps: Step 1, prepare a ca. 2 M HCl solution by adding 0.5 L of concentrated HCl to 2 L of DDI water. Step 2, Pipette 30 mL of aniline into the 2.5 L HCl solution and continuously stir throughout the entire process. Step

3, add 50 g urea and 50 g FeCl$_3$ into the above solution. Step 4, add 50 g ammonium persulfate (APS) as an oxidant to polymerize the aniline in the above solution. Continue rigorously stirring at room temperature for at least 3 hours to allow full polymerization of the aniline. Step 5, Pipette 4 g of the HNO$_3$, treated KJ300 suspension slowly into the polyaniline mixture. Maintain stirring of the solution for 48 hours as rigorously as possible at room temperature. Step 6, After 48 hours of constant stirring, the liquid from the mixture is removed by evaporation by heating the solution to ca. 70 °C. Step 7, collect the solid material and ball mill it into powder. Step 8, Heat-treat the catalyst sample at 200 °C for 1 hour in Ar atmosphere and ball mill it again until the powder is as fine as possible. Step 9, the subsequent heat-treatment for the resulting powder is performed at 1000 °C in Ar atmosphere for 1 hour. Step 10, the sample was taken from the furnace and subsequently leached in 300 mL 0.5 M H$_2$SO$_4$ at 80 - 90 °C for 8 hours. Filter and wash the samples with DDI until neutral and dry in a vacuum oven at 80°C overnight. Step 11, the dried sample was then heated again at 1000 °C in an inert atmosphere for 1 hour to further improve the ORR activity and to remove surface functional groups.

5.2.2 Half catalyst coated membrane (CCM) preparation

Step 1, prepare the ink using a weight ratio of catalyst: isopropanol : water: Nafion (5 wt.%) of 1: 12: 12: 11. For loading of 3 mg cm^{-2}, prepare ink using ca. 250 mg catalyst. If using different wt.% Nafion solutions, adjust this amount accordingly. Step 2, sonicate the ink for at least 1 hour and let it sit overnight. The next day, sonicate for one more hour before painting the catalyst ink onto the membrane. Step 3, place a membrane with a protective layer on a hotplate, facing the side with protective layer to the hotplate. Place a 50 cm^2 square (9.4 cm × 5.4 cm) Teflon sheet on the center of the membrane. Step 4, use Teflon coated fiberglass tape to tape the cover sheet to the exposed areas of the membrane, and then remove the 50 cm^2 Teflon sheet square template,

exposing the 50 cm^2 area of the membrane to be painted. Step 5, heat the vacuum table up to 80 °C. Once it reaches the temperature, painting can begin. Step 6, paint the prepared catalyst ink onto the exposed area of the membrane, using smooth strokes across. Vary directions to achieve the coating as uniform as possible over the entire area. Step 7, after painting all of the ink, allow the catalyst coated membrane to dry for ca. 1-2 hours. Step 8, after completely dry, turn off the heat and remove the tape holding the membrane to the hotplate.

5.2.3 Membrane electrode assembly (MEA) assembly

Step 1, peel of the protection cover of the membrane and decal anode catalyst to the same side of the protection cover, which is the opposite side of the cathode catalyst layer (CCL). The anode catalyst layer should be larger than 50 cm^{-2} and fully covers the backside of the CCL to ensure full utilization of the 50 cm^{-2} areas. Step 2, place the gasket frame on the vacuum plate and put the cathode GDL on the frame. The microporous layer (MPL) on the cathode GDL should face up. Step 3, Align the CCM to the cathode GDL and keep the cathode catalyst to the cathode GDL. Step 4, Align the anode GDL to the anode side of CCM and keep the MPL facing the anode catalyst layer on the membrane. Step 5, place the other piece of gasket frame and seal the edges of the MEA.

5.3 Result and Discussion

5.3.1 Testing parameter discussion

Unlike the oxygen reduction reaction in half-cell testing, fuel cell testing is much more complicated and is affected by several different parameters in the testing process. In the half cell, the proton can move in the acidic aqueous electrolyte with low resistance. In a PEM fuel cell, protons have to move through a solid proton exchange membrane. The membrane has a

tetrafluoroethylene (PTFE) backbone, with side chains with sulfonate groups. When hydrated, there will be nano-scale water channels inside the membrane, surrounded by the sulfonate groups.[172-174] Due to the proton conducting mechanism, hydration level greatly impacts the proton conductivity of a membrane and further influence the overall fuel cell performance.[175-177] Besides the hydration level, the operating temperature, pressure, oxygen concentration, and oxidant stoichiometry can affect the oxygen reduction process.[43, 44, 46, 178-184] In this section, we will study how these factors impact fuel cell performance.

1. Operating temperature

The operating temperature not only has an impact on the proton conductivity in the membrane and catalyst layer; it also affects the cell voltage because the Gibbs free energy change varies with the temperature.

$$\mathrm{d}G = -S\,\mathrm{d}T + V\,\mathrm{d}P \qquad\qquad (5.1)$$

which can be derived to

$$(\mathrm{d}G/\,\mathrm{d}T)_P = -S \qquad\qquad (5.2)$$

For molar reaction, the reaction becomes

$$(\mathrm{d}(\Delta\hat{g}/\,\mathrm{d}T))_P = -\Delta\hat{s} \qquad\qquad (5.3)$$

It is also known that

$$\Delta\hat{g} = -nFE \qquad\qquad (5.4)$$

A combination of equation 5.3 and 5.4 gives the relationship between cell voltage and temperature:

$$(dE/\ dT))_P = \Delta\hat{s}/(nF) \qquad\qquad (5.5)$$

Because $\Delta\hat{s}$ is negative for the hydrogen fuel cell reaction, the cell voltage has a negative correlation with the temperature. If we only consider the cell voltage, it would be concluded that the fuel cell should be operated under lower temperatures. However, decrease the temperature may cause drops in both reaction kinetics and the proton conductivity.[185-188] We have tested the fuel cell at different temperatures. Because the vapor pressure of water at different temperatures, the backpressure was set at different values to keep oxidant partial pressure the same. In Figure 5-1(a) it can be seen the overall fuel cell performance is better at higher temperatures. The polarization curves of 60 °C, 70 °C and 80 °C overlaps at the kinetic region, and start to differentiate at the ohmic region. In Figure 5-1 (b) we can see cell voltage at 60 °C is the highest, and 80 °C is the lowest. As we just discussed, according to the thermodynamics of the fuel cells, cell voltage is negatively correlated with the temperature.
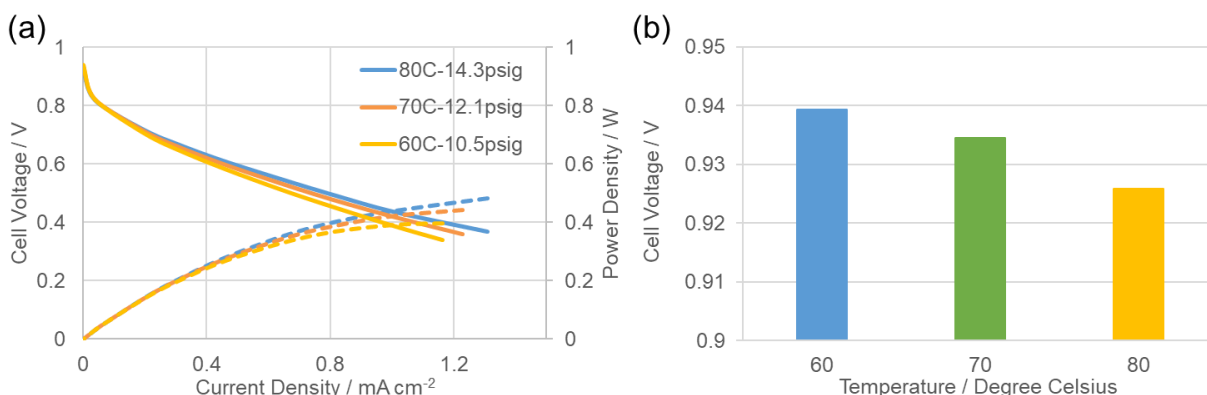
Figure 5- 1. (a) Polarization curves and power density curves obtained at 60 °C, 70 °C, and 80 °C. (b) The open-cell voltages obtained at 60 °C, 70 °C, and 80 °C.

From the figure, we can see the fuel cell performances are a combined result of different factors. The cell voltage is clearly affected by the operation temperature; however, the kinetics

doesn't seem to show much difference. Overall, for the three different temperatures that we tested, fuel cell performances are mostly affected by the ohmic loss, which should come from the proton transport resistance that is affected by temperature.

2. Relative humidity

The hydration level is a key factor that affects the proton mobility in both the membrane and the catalyst layer. When the fuel cell is operated under low relative humidity (RH) condition, water channels in the membrane and catalyst layer shrink and make proton transport more difficult.[189-192] When the fuel cell is operated under high RH, water may condense at some part of the MEA or even gas flow channels. Water condensation can cause severe flooding issue in a PEM fuel cell and causes fuel cell performance to drop significantly.[193-195] Flooding issue is usually more challenging at a high current density region than at a low current density region because more water is produced by the fuel cell reaction at high current densities.
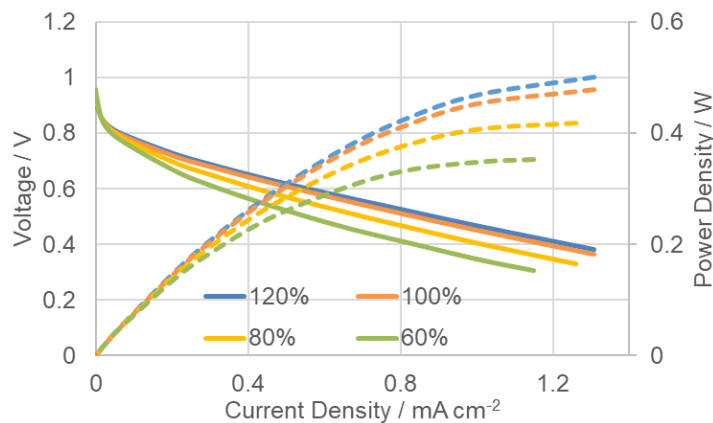
Figure 5- 2. Polarization curves and power density curves obtained at 60%, 80%, 100% and 120% relative humidity.

We have tested the fuel cell under different RH conditions to reach different hydration levels of the membrane and ionomer in the catalyst layer (Figure 5-2). It is found that the fuel cell performance keeps increase with the increment of the RH. With a lower RH of 60%, the peak

power density drops by 1/3 compared to that of 100% RH. The results testify that with low hydration levels, the poor proton transportability dramatically harmed the fuel cell performance. However, at a higher hydration level at 120% RH, no evidence of flooding can be observed even at high current density region. The highly porous structure of the secondary nitrogen-doped catalyst should have benefits in the water management of the MEA.

3. Pressure

The gas pressure also affects the cell voltage because the Gibbs free energy change varies with the pressure.

$$dG = -S\,dT + V\,dP \qquad (5.6)$$

which can be derived to

$$(dG/\,dP)_T = V \qquad (5.7)$$

For molar reaction, the reaction becomes

$$(d(\Delta\hat{g}/\,dP))_T = -\Delta v \qquad (5.8)$$

It is also known that

$$\Delta\hat{g} = -nFE \qquad (5.9)$$

A combination of equation 5.3 and 5.4 gives the relationship between cell voltage and pressure:

$$(dE/\,dP))_T = -\Delta v/(nF) \qquad (5.10)$$

In the hydrogen fuel cell, the H_2 and O_2 react to become H_2O (l), and the volume change is negative. According to 5.10, if Δv is negative, the cell voltage increases with the pressure. We

have tested the fuel cell under 0.5 bar, 1 bar, and 1.5 bar backpressure (Figure 5-3). At the kinetic region, the polarization curves start to show differences between the three pressures. Fuel cells show higher performance in the kinetic region at high pressure than low pressure, mainly because of the lifted pressure increases reactant concentration at the triple-phase boundaries (TPBs). In the ohmic region, high pressure also shows less ohmic loss than low pressure, likely because high pressure introduces higher hydration levels of the membrane and improves the membrane
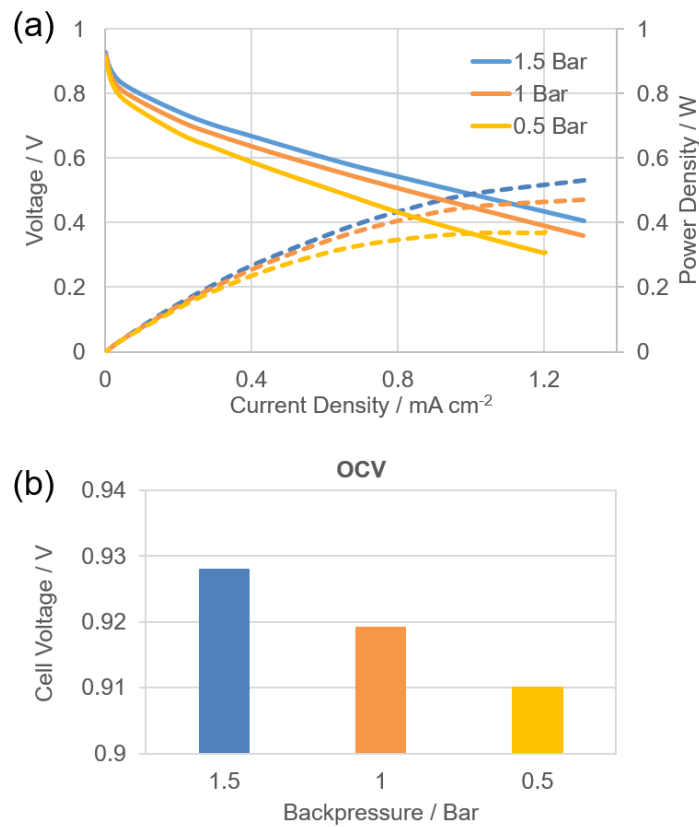
Figure 5- 3. (a) H_2-Air polarization curves and power density curves; (b) The open-cell voltages obtained at 0.5 Bar, 1 Bar, and 1.5 Bar. Temperature: 80 °C, RH: 100%.

conductivity.

4. O_2 concentration

In the PEM fuel cell vehicles, ambient air is used as the oxidant rather than pure oxygen. Generally, there is an additional accessory, air compressor, added to the fuel cell system to supply compressed air to the fuel cell cathode. Theoretically, there is 21% O_2 in the ambient air supplied to the fuel cell. However, it is only true for the inlet gas flow that O_2 concentration is 21%. After the long journey in the gas flow channels, part of the oxygen is consumed while nitrogen remains untouched, resulting in lower oxygen concentration in the outlet gas flow.[196-198] Just like temperature, RH and pressure that we discussed, the oxygen concentration in the oxidant also has a significant impact on the fuel cell performance. During the operation of fuel cells, the gas pressure is generally controlled at a certain pressure. Since the total pressure is fixed at a certain value, when the oxygen concentration varies, the partial pressure of oxygen varies as well. As we discussed in the last section, the changing in pressure affects cell voltage by tuning both the reaction thermodynamics and kinetics. We have tested the fuel cell performance with air (21% O_2)
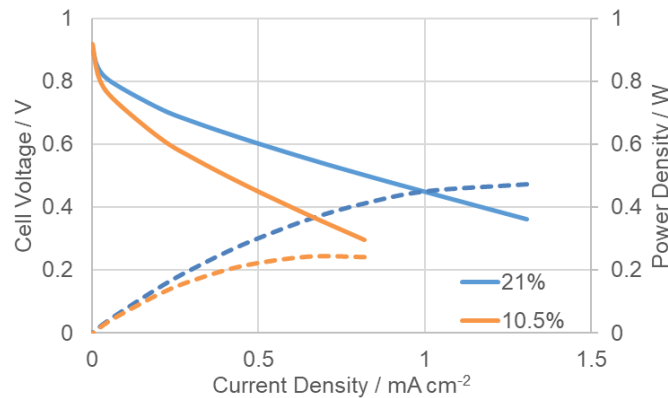
Figure 5- 4. Polarization curves and power density curves obtained with 21% O_2 and 10.5% O_2. Temperature: 80 °C, RH: 100%, backpressure: 1 bar.

and 10.5% O_2 (mixed with N_2) as the oxidant at the cathode. Figure 5-4 shows the polarization curve obtained by ambient air and 10.5 % O_2. Compared to ambient air, the polarization curve obtained by 10.5 % O_2 shows much higher voltage loss in both the kinetic region and ohmic region.

5. Oxidant stoichiometry

When we run the fuel cells, the hydrogen and oxygen are always sufficiently supplied to ensure enough fuel and oxidant for reactions. Oxidant stoichiometry is used to quantify the amount of oxidant that is supplied to the fuel cell. If the fuel cell is operating at a constant current density of 1.5 A cm^{-2}. The electricity that is involved in the reaction per minute can be calculated as 1.5 A·cm^{-2} × 50 cm^2 × 60 s/min = 4500 C/minute, which is (4500 C/minute) / (96485 C/mole) = 0.0466 mole electrons per minute. We know that each O_2 molecule takes 4 electrons in the reaction, which means 0.0466/4 = 0.0117 mole of O_2 is consumed per minute. Consider that only 21% oxygen is contained in the air, 0.0117/0.21 = 0.0557 mole of air is needed per minute. Assume that the fuel cell is operated at 80°C, 1 bar back pressure, we can calculate the volume of air that is needed per minute according to the ideal gas law PV = nRT, as V = nRT/P = 0.0557mole × 8.314 m^3·Pa·K^{-1}·mol^{-1} × 353.15 K / 100000 Pa = 0.0008177 m^3 = 0.817 L. The stoichiometry number can be calculated based on the airflow rate of 0.817 L/minute. If we supply air at a flow rate of
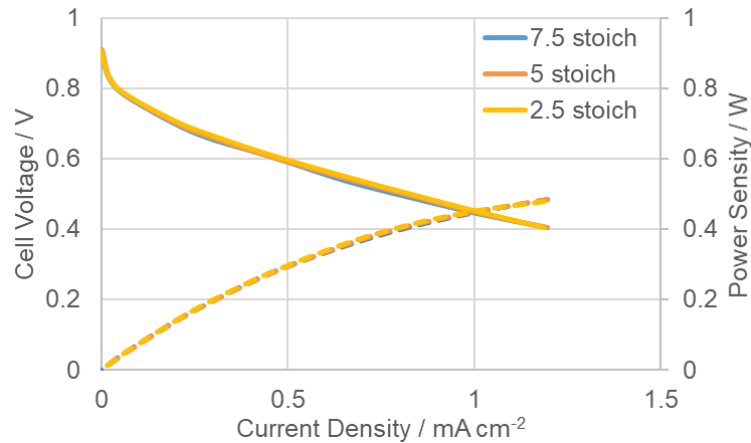

Figure 5- 5. Hydrogen-air polarization curves and power density curves obtained at 2.5, 5 and 7.5 stoichiometry. Temperature: 80 °C, RH: 100%, backpressure: 1 bar.

0.817 L/minute, that gives the stoichiometry value of 1. If we supply air at a flow rate of 1.634 L/minute, the stoichiometry increase to 2.

Even though the fuel cell doesn't necessarily operate at a constant current density, as long as the fuel cell is supplied with a fixed gas flow rate, the stoichiometry should be calculated based on a fixed current. However, the fuel cell can be operated at a constant stoichiometry as well, so the gas flow rate is tuned according to the real-time current. Since the test station we use is not able to run at constant stoichiometry, we have tested the fuel cell at constant flows. The stoichiometry is calculated based on a current density of 1.5 A·cm^{-2}. Chung et al. have reported performance loss after decreasing the stoichiometry from 9.5 to 2.5,[65] which is reasonable because the reduction in oxidant supply should have some negative effect on performance. We have tested our MEA at 2.5, 5 and 7.5 stoichiometry, and found no observable difference between the performances (Figure 5-5). The results show that the MEA performance is stable against stoichiometry changes. The low requirement of stoichiometry is beneficial for future applications of the MEA into larger equipment because it will save energy by using less compressed air.

5.3.2 Design parameter discussion

1. Catalyst loading

The mechanism that catalyst loading affects MEA performance in the fuel cell is similar to how catalyst loading affects half-cell activity. Firstly, increasing the catalyst loading can provide more active sites for the reaction to take place, thus improving the catalytic activity of the catalyst layer. Secondly, by adding the catalyst loading, the catalyst layer will be thicker and allows more ORR intermediates to be fully reduced to water, in that manner the overall ORR selectivity is improved.[199-201] However, adding catalyst that impacts, but also negative ones. The reaction behavior is more complicated in the MEA than in a half-cell. As we have discussed previously that in the half-cell, oxygen transport is not a big concern because the rotating disk electrode is capable of accelerating the oxygen transport process. In the MEA, if the catalyst layer is too thick, oxygen

may have difficulty to reach the membrane/catalyst layer interface, where the majority of the reaction takes place. Another issue that the thick catalyst layer can block water transport as well. The PEM fuel cells are operated under 100 °C in most applications, water is generated at the cathode side of the membrane in the liquid phase. If the water through, the catalyst layer will be flooded and causes a severe drop in the performance.
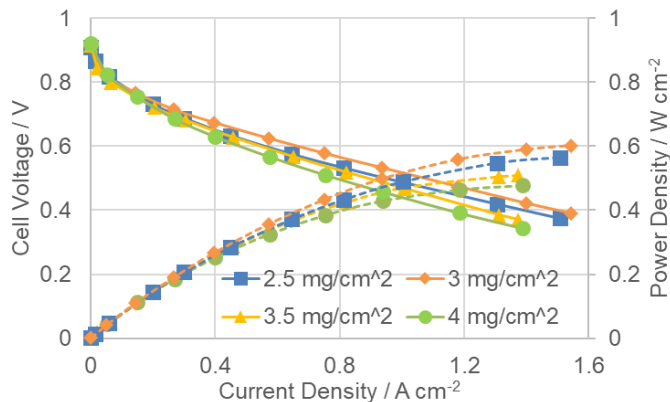
Figure 5- 6. Hydrogen-air polarization curves and power density curves obtained at the catalyst loading of 2.5 mg/cm^2, 3 mg/cm^2, 3.5 mg/cm^2 and 4 mg/cm^2. Ionomer content: 35%, temperature: 80 °C, RH: 100%, backpressure: 1 bar.

Banham et al. have reported the catalyst loading of 4 mg cm^{-2} to reach the highest performance with 35% ionomer loading.[23] In our work, 4 mg cm^{-2} loading was firstly tested and lower loadings have been tried after. It was found 3 mg cm^{-2} is the optimal catalyst loading for the SU-PAU catalyst. The high porosity of SU-PAU can bring more active sites but will cause thicker catalyst layer, hence lower catalyst loading is preferred compared to the loading reported by Banham and coworkers. In Figure 5-6 we still can see that 4 mg cm^{-2} loading show higher performance at the kinetic region, but the voltage loss becomes more rapid at higher current densities compared to the lower loading ones. In the first chapter, we have discussed the reasons to cause fuel cell voltage loss, and the performance is a combined result of these reasons. Here the 3 mg cm^{-2} has the best combination of all the losses, which shows the best performance among the

four loadings. A good sign for all these loadings is that there is no evidence of flooding even for the high loading, allowing us to do more optimization on the ionomer loadings.

2. ionomer loading

As we can tell from the MEA performance obtained by catalyst loading study that the poor proton conductivity can cause rapid voltage loss in the ohmic loss region. It is also observed there was no evidence of flooding even at high catalyst loading. It is worthy to try increasing the ionomer content to improve the proton conductivity in the catalyst layer. By increasing the ionomer loading, it is possible to improve the voltage loss introduced by proton transport resistance. It is also possible to enhance the kinetic activity because higher ionomer content can increase the electrochemical accessible area of the catalysts.[202] However, increasing ionomer content may lead to mass transport issues as well, because the ionomer will fill up the pores of the catalysts and block the oxygen and water transport paths.[203-205] Moreover, because the ionomer is more hydrophilic than the carbon-based catalyst, water generated from the reaction is more difficult to be removed from the catalyst layer and causes flooding.

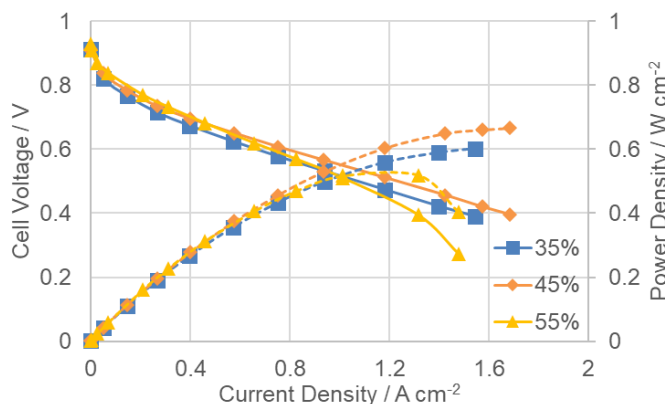**Figure 5- 7.** Hydrogen-air polarization curves and power density curves obtained with the ionomer content of 35%, 45%, and 55%. Catalyst loading: 3 mg/cm^2, temperature: 80 °C, RH: 100%, backpressure: 1 bar.

In Figure 5-7 we have increased the ionomer loading from 35% to 45 and 55%. Comparing to 35% ionomer content, 45% has less kinetic loss and ohmic loss, resulting in 60 mW higher peak power density. If the ionomer loading gets further increased to 55%, we can still observe a slight improvement in the kinetic region, but the performance suffers from flooding issues at higher current densities. The polarization curve shows a dramatic drop after the current density reaches 1.2 mA cm^{-2} because of the flooding. In the work reported before,[23] 35% is the optimal ionomer content, which doesn't work as the optimal ionomer content for SU-PAU. It should due to the high surface area of SU-PAU, which needs more ionomer to cover the surface of the catalyst.

3. The equivalent weight of the ionomer

Besides modifying the ionomer content, another way to reduce the ionic resistance in the catalyst layer is to change the ionomer type. The ionomer has sulfonate groups to carry protons, and those protons are free to move from one site to another to fulfill the proton transport within the catalyst layer. The abundance of protons in the catalyst layer is of great importance to the proton conductivity, which can be evaluated by the equivalent weight (EW).[206-208] The EW of an ionomer is the weight of the polymer required to provide one mole of exchangeable protons. From this definition, we know a low EW means the ionomer has a high content of exchangeable protons. The ionomer we used for the MEAs been studied has an EW of 1100, which is a commonly used ionomer in many other works.[209-212] For the purpose of further improving the ionomer conductivity, here we tried another ionomer with a lower EW of 700. The kinetic region of the polarization curves are quite close to each other as shown in Figure 5-8 (a).

However, the EW700 polarization curve shows severe flooding issues, mainly due to the high proton content and high hydrophilicity. The oxygen reduction happens on the TPB and produces water, which is difficult to be removed if the hydrophilicity of the ionomer is too high.

When the operation RH is reduced to 80%, the flooding issue gets better but still can not be fully eliminated. It is also noticed that the polarization curve of EW700 drops much faster than EW1100 in the ohmic loss region, which may be caused by either flooding or ionic resistance. We have tested the cathode catalyst layer (CCL) resistance at different RH, as shown in Figure 5-8 (b). Just as expected, the CCL ionic resistances of EW700 are much lower than that of EW1100 at different RH, from which we know that the voltage drop at the ohmic loss region comes from flooding as well.
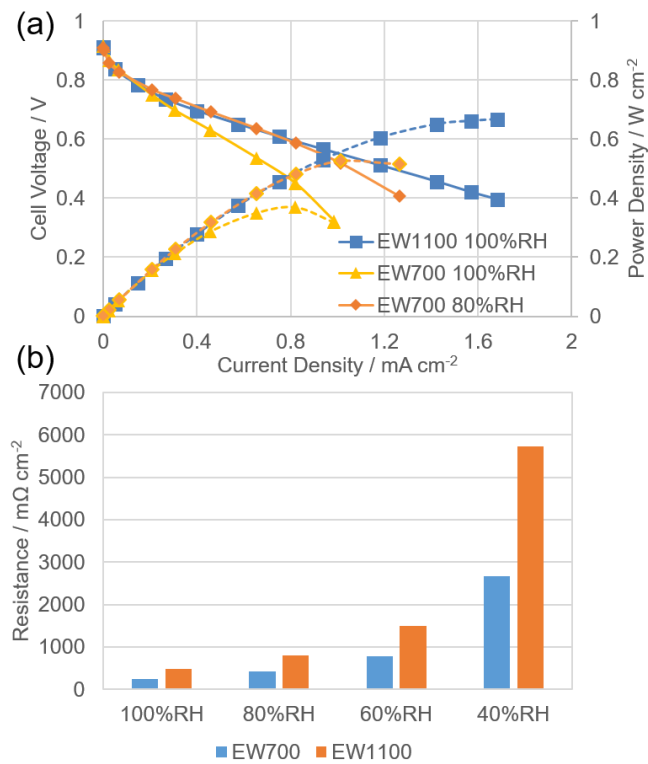
Figure 5- 8. (a) Hydrogen-air polarization curves and power density curves obtained with the EW1100 ionomer at 100%RH, EW700 ionomer at 100%RH, and EW700 ionomer at 80%RH, Catalyst loading: 3 mg/cm^2, temperature: 80 °C, backpressure: 1 bar. (b) Ionic resistance of the cathode catalyst layer prepared by EW1100 ionomer and EW700 ionomer, acquired at different RH.

4. Membrane thickness

By changing the ionomer content and ionomer type, we know it is possible to reduce the proton transport resistance in the catalyst layer by adding an adequate amount of ionomer. Is there any optimization we can conduct to reduce proton transport resistance in the membrane as well? It is possible to achieve this goal through the optimization of the membrane.[42, 213-215] Since the synthesis of the membrane is without the scope of this research, we just applied commercially available membranes in our MEA. Proton exchange membrane with two different thicknesses (15 μm and 25 μm) was selected and the results are shown in Figure 5-9. The MEA prepared with 15 μm membrane clearly shows less voltage loss in the ohmic loss region, indicating lower membrane resistance. It is possible that with the development of membrane in the future, MEA performance can be further improved by simply using thinner membranes or other membranes with higher proton conductivity.
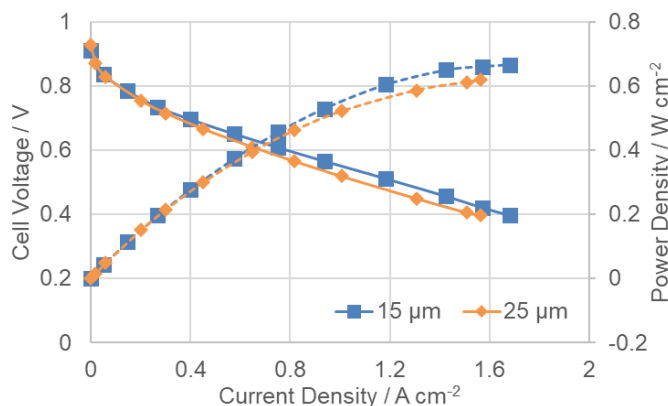
Figure 5- 9. Hydrogen-air polarization curves and power density curves obtained with the membrane thickness of 15 μm and 25 μm. Catalyst loading: 3 mg/cm^2, temperature: 80 °C, RH: 100%, backpressure: 1 bar.

5.3.3 MEA degradation study

Catalyst stability has always been a critical challenge for the PGM-free catalyst even in the half-cell. In a fuel cell, the working environment becomes harsher for the catalyst, for example, both the temperature and pressure are usually higher in a full cell, and the catalyst layer uniformity

usually gets worse for a larger area. Besides catalyst, the MEA has other components which may decay as well. The degradation of any component can somehow affect the overall performance. We have placed the MEA under steady-state stability test for 50 hours by holding the current density at 0.5 A cm^{-2} to see the stability of the MEA under operation condition. From Figure 5-10 (a) we can see that the cell voltage dropped around 100 mV after 50 hours of operation. Figure 5-10 (b) shows the polarization curves that were recorded before and after the stability test. The end of test (EOT) polarization curve shows a significant drop comparing to the beginning of test polarization curve. This drop is reasonable because the PGM-free catalyst is known to be poor for stability, which is one of the biggest challenges faced by PGM-free catalyst.[216-218] Figure 5-10 (b) tells us that the origination of the voltage degradation comes from the low current density region. Firstly, there is a mixed potential decrement of 40 mV between EOT and BOT (beginning of test), indicated by the OCVs (Figure 5-10 (c)). The kinetic voltage loss of EOT polarization curve is also more prominent comparing to that of the BOT polarization curve as well. At the high current densities in ohmic loss region, EOT and BOT polarization curves are nearly in parallel, which means they suffer from similar proton transport losses from the membrane and catalyst layer. We used Electrochemical Impedance Spectroscopy (EIS) to test the resistance of the fuel cell and found that the high-frequency resistance (HFR) of BOT and EOT are quite closed to each other (Figure 5-10 (d)). The cathode catalyst layer (CCL) ionic resistances are also similar between BOT and EOT. In fact, the EOT resistances are even slightly lower, probably because the membrane and ionomer are more hydrated after envolving in the reaction for a while. The MEA may have a better combination of all the components after been pressurized for a longer time.
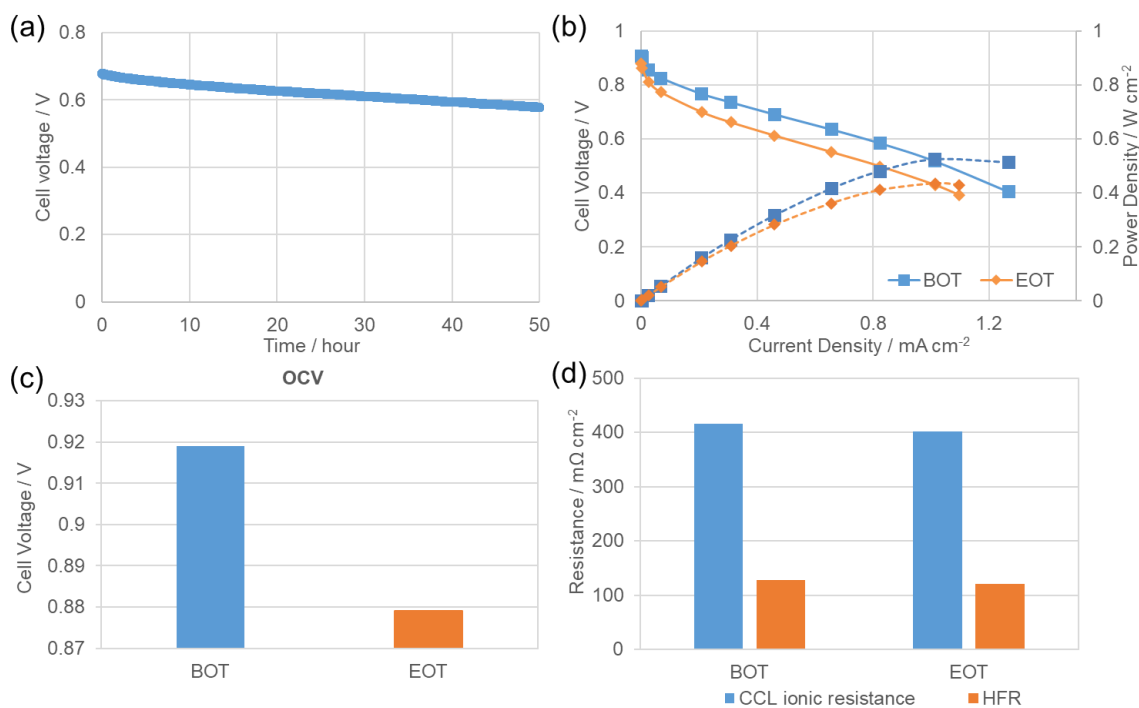
Figure 5- 10. (a) Steady-state voltage curve by holding the current density at 0.5 A/cm^2. (b) Polarization curves at 5psig, (c) OCVs and (d) CCL ionic resistance and HFR of the MEA obtained at BOT and EOT.

5.4 Conclusions

In this chapter, we have tested the MEAs using the PGM-free catalyst as the cathode catalyst layer and studied a variety of factors that may have an impact on fuel cell performance. The testing parameters are firstly studied, including operating temperature, relative humidity, pressure, oxygen concentration, and oxidant stoichiometry. Except for the oxidant stoichiometry, tuning the other four parameters had great impacts on the fuel cell performance. By knowing how these parameters affect the performance, we will have a better idea of how to set up the testing conditions in future testings. It was noted that low oxidant stoichiometry didn't show a negative impact on the performance, telling that the MEA can be operated with low oxidant supply without sacrificing the power output. Different design parameters including catalyst loading, ionomer content,

96

ionomer EW, and membrane thickness were also studied to understand how they can affect the PEM fuel cell performance. We have optimized the catalyst loading and found out 3 mg cm^{-2} to be the best loading for SU-PAU catalyst. The ionomer content was optimized as well and 45% was found to be the optimal ionomer loading for our design. We also tried different ionomer with low equivalent weight (EW700), aimed at improving the ionic conductivity, but severe flooding issue was observed and the performance was low compared to EW1100. A thicker membrane was tested as the last design parameter study, and lower performance was obtained, which was within the expectation. Through the membrane thickness study, even though the performance was not improved, we know that it is possible to get better performance with thinner membranes or other membranes with higher proton conductivity. The MEA degradation was lastly studied by steady-state durability test. After 50 hours of current holding at 0.5 A cm^{-2}, the MEA shows a peak power density drop of 17%. From the polarization curve and resistances data, it is known that the degradation mostly came from the kinetic region, which is due to the activity loss of the catalyst.

Chapter 6 Conclusions and Perspective

6.1 Conclusions

Aiming at the development of highly active PGM-free catalyst and MEA, different strategies were performed for catalyst synthesis. Systematic studies have been performed to understand how these strategies may influence the catalyst activity. MEA performance has also been studied and optimized based on both testing parameters and MEA design. From the catalyst level to the catalyst layer and MEA level, we have done solid works step by step to achieve better and better half-cell activity and fuel cell performance. Moving forward to the real application of the catalysts, the catalyst synthesis has been scaled-up to commercial-scale from laboratory-scale. MEA testings were performed based on 50 cm^2 MEAs rather than 5 cm^2 MEAs which is most commonly used in the publications.

In chapter three, ultra-high surface area nitrogen-doped hollow carbon spheres (HCS) were successfully prepared as the carbon support. Two types of heteroatom doped catalyst HCS-PA and HCS-A were prepared with aminothiophenol and poly-aminothiophenol, respectively, as the doping agent. It was manifested that both of these, monomer and polymer, acting as heteroatom doping precursors, were able to increase ORR activity. However, the monomer, aminothiophenol, could be a better choice to obtain favorable morphology and surface area retention of the ultra-high surface area spherical supporting material. With the obtained unique embellished hollow sphere structure and high surface area, HCS-A showed remarkable ORR activity in both acidic and alkaline media. In addition to outstanding ORR activity, HCS-A also demonstrated excellent durability with negligible degradation after 20000 cycles in alkaline medium. PEM fuel cell test with HCS-A as a cathode catalyst reached a peak power density of 500 mW cm^{-2}. In a zinc-air

battery test, the discharging power density of HCS-A reached a maximum of 195 mW cm^{-2} in ambient air, which is one of the best zinc-air performances reported in ambient conditions. Our study not only reports a catalyst with high activity but more importantly validates a strategy to maintain the structural advantages from a favorable supporting material.

In chapter four, we have synthesized a highly active PGM-free ORR catalyst by secondary nitrogen doping and successfully scaled up the catalyst without diminishing the activity. Half-cell electrochemical testing proved that the secondary nitrogen doping increased both ORR activity and selectivity. Increasing the catalyst loading didn't bring much improvement in the ORR activity of the primary doped catalyst (SU-PA). Even though by increasing the loading, SU-PA has comparable DLC with SU-PAU, its ORR activity is still inferior, indicating the benefits of secondary doping can't be achieved by simply increasing the accessible electrochemical area. Raman spectra show that secondary nitrogen doping increased the defect level of the catalyst. Nitrogen adsorption-desorption isothermal curve and pore distribution tell us the secondary nitrogen doping increased the specific surface area and created more micropores within the catalyst. XPS results proved that the secondary nitrogen doping removed some of the oxidized nitrogen species and enhanced the formation of iron-nitrogen coordination in the active sites. Because of the reasons mentioned above, secondary nitrogen doping not only shows higher ORR activity in half-cell testing but also proved its advanced performance in fuel cell testing. We have achieved a peak power density of 1 W cm^{-2} on a single-cell with SU-PAU as the cathode catalyst.

In chapter five, we have tested the MEAs using the PGM-free catalyst as the cathode catalyst layer and studied a variety of factors that may have an impact on fuel cell performance. The testing parameters are firstly studied, including operating temperature, relative humidity, pressure, oxygen concentration, and oxidant stoichiometry. Except for the oxidant stoichiometry, tuning the other

four parameters had great impacts on the fuel cell performance. By knowing how these parameters affect the performance, we will have a better idea of how to set up the testing conditions in future testings. It was noted that low oxidant stoichiometry didn't show negative impact on the performance, telling that the MEA can be operated with low oxidant supply without sacrificing the power output. Different design parameters including catalyst loading, ionomer content, ionomer EW, and membrane thickness were also studied to understand how they can affect the PEM fuel cell performance. We have optimized the catalyst loading and found out 3 mg cm^{-2} to be the best loading for SU-PAU catalyst. The ionomer content was optimized as well and 45% was found to be the optimal ionomer loading for our design. We also tried different ionomer with low equivalent weight (EW700), aimed at improving the ionic conductivity, but severe flooding issue was observed and the performance was low compared to EW1100. A thicker membrane was tested as the last design parameter study, and lower performance was obtained, which was within the expectation. Through the membrane thickness study, even though the performance was not improved, we know that it is possible to get better performance with thinner membranes or other membranes with higher proton conductivity. The MEA degradation was lastly studied by steady-state durability test. After 50 hours of current holding at 0.5 A cm^{-2}, the MEA shows a peak power density drop of 17%. From the polarization curve and resistances data, it is known that the degradation mostly came from the kinetic region, which is due to the activity loss of the catalyst. The activity loss of the catalyst suggests the intrinsic activity loss of the PGM-free catalyst needs to be addressed in future work.

In summary, we have tried different strategies for PGM-free catalyst synthesis and successfully obtained highly active catalysts through those strategies. Effective structure retention and secondary nitrogen doping were proved to be beneficial to catalyst activity in chapter 3 and

chapter 4, respectively. We were also able to scale up the PGM-free catalyst for larger MEA preparation, without any diminishment of the half-cell activity or MEA performance. We continued on testing parameter study and MEA design study to promote the catalyst performance in a PEM fuel cell. After going through the systematic study and optimization, we have greatly improved the MEA performance and gained an in-depth understanding of electron transport, proton transport, oxygen transport, and water management within the MEA.

6.2 Perspective

Many countries over the world have set up targets to reduce or even eliminate internal combustion engine vehicles in the near future. Automobile companies such as Volkswagen Group and Daimler have made forward-looking end-of-life projections for their internal combustion engines and replace them with electrified vehicles. The world's biggest automobile company, Toyota, has proposed its vision of a sustainable society based on the use of diverse energy sources including fossil fuels, electricity and hydrogen infrastructures (Figure 6-1).[219] As the simplest element and the most plentiful element in the universe, hydrogen has drawn a lot of attention as an energy carrier and fuel source. However, compared to fossil fuels such as coal, crude oil, and natural gas, hydrogen energy is still at its early stage of applications, and has a great potential to be applied in many fields. The World Energy Council set out a conclusion in February 2019, that effectively applying hydrogen could deliver up to 30 percent of the Europe 2050 climate targets. Comparing to fossil fuels, hydrogen fuel has several advantages: High fuel efficiency, energy conversion efficiency can reach up to 60%-70% for a hydrogen fuel cell compared to 30%-35% for conventional combustion methods; Zero carbon emission, hydrogen can be made by renewable energy such as nuclear, wind, solar, et al. (carbon-free), or from fossil fuels with the CO_2 by-product captured and stored (carbon-neutral); Regenerative, hydrogen can be easily regenerated

from water by other forms of energy, such as electrical energy (electrolysis), thermal energy (thermochemical water splitting), and solar energy (photoelectrolysis). By utilizing hydrogen as the fuel, fuel cell electric vehicle (FCEV), fuel cell buses, fuel cell trains, and other fuel cell-powered transportation methods can perfectly fit into the "hydrogen grid", making zero-emission transportation possible in the future "hydrogen society".
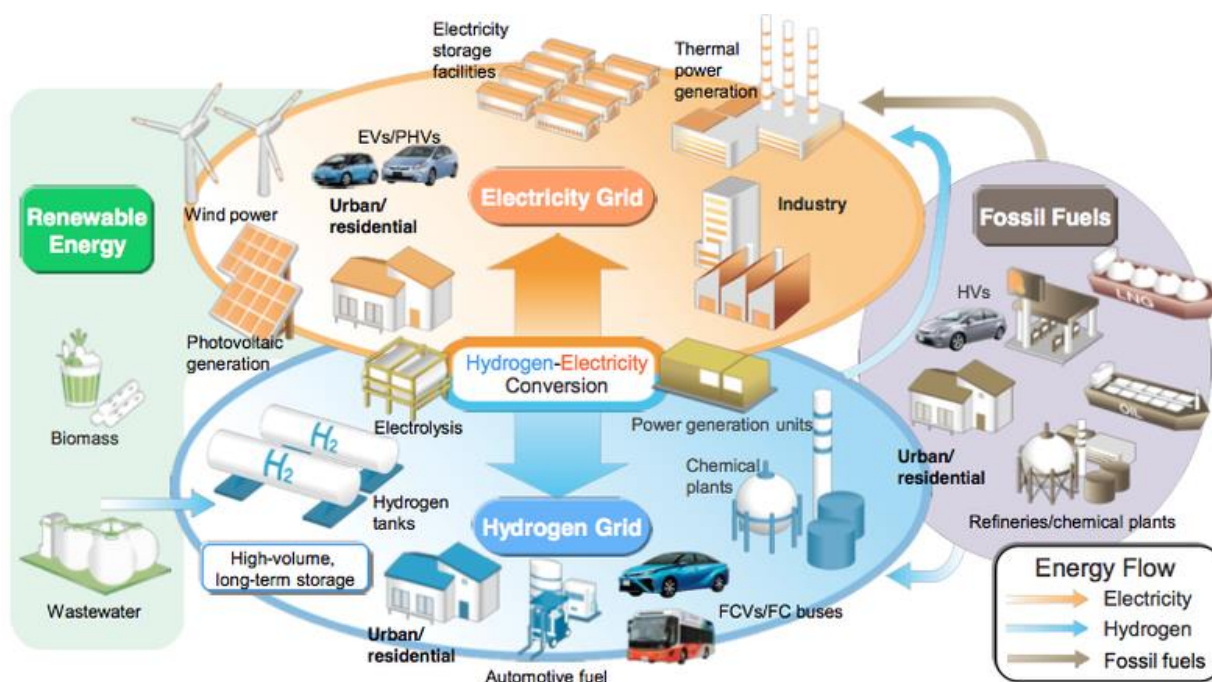
Figure 6- 1. Toyota's vision of a sustainable society, with electricity and hydrogen infrastructures. Source: Toyota.

However, before the successful commercialization of PEM fuel cells in transportation applications, the hydrogen refueling infrastructure must be well developed, and the cost of PEM fuel cells needs to be competitive with the internal combustion engine (ICE). By using low platinum loading catalysts, or PGM-free catalysts, the cost of PEM fuel cells can be greatly reduced as catalyst cost takes up nearly half of the total stack cost, as predicted by DOE, based on the production scale of 500,000 systems per year. If the production scale increases, the catalyst

will occupy a higher percentage of the total cost because the platinum price most likely will increase when demand is high. Consider that the electrification of the transportation applications is unstoppable, actions must be taken to support the wide application of PEM fuel cells in transportation applications. From the perspective of lowering the catalyst cost, the following actions are helpful: 1. Optimization of the CCL design to reduce catalyst loading; 2. Improve the utilization of platinum by developing advanced catalyst structures, platinum alloys, and other methods; 3. Develop Pt and PGM-free hybrid catalysts to reduce Pt loading; 4. Develop highly active and durable PGM-free catalysts. In terms of utilizing the PGM-free catalysts into automotive applications, there still are great challenges. First of all, PGM-free catalyst beginning of life (BOL) performance needs improvement to be comparable with Pt-bases catalyst. Secondly, the stability and durability of the PGM-free catalyst also need to be significantly enhanced to meet the requirement for automotive applications. Thirdly, the ORR mechanism and performance degradation mechanism should be studied well in order to improve catalyst performance and lifetime. Lastly, the catalyst synthesis process should be easy for large scale manufacture, and cost-effective.

References

1.   International Energy Outlook 2017
2.   https://rainforests.mongabay.com/energy/energy.
3.   S. Shafiee and E. Topal, Energy policy 37 (2009) 181-189.
4.   B. Thinnes, Hydrocarbon Processing 91 (2012) 9-10.
5.   M. L. Perry and T. F. Fuller, Journal of the electrochemical society 149 (2002) S59-S67.
6.   B. C. Steele and A. Heinzel, in *Materials For Sustainable Energy: A Collection of Peer-Reviewed Research and Review Articles from Nature Publishing Group*, World Scientific, 2011, pp. 224-231.
7.   A. Choudhury, H. Chandra and A. Arora, Renewable and Sustainable Energy Reviews 20 (2013) 430-442.
8.   J.-H. Wee, Renewable and sustainable energy reviews 11 (2007) 1720-1738.
9.   J. Zhang, *PEM fuel cell electrocatalysts and catalyst layers: fundamentals and applications*, Springer Science & Business Media, 2008.
10.   A. de Frank Bruijn and G. J. Janssen, Fuel Cells and Hydrogen Production: A Volume in the Encyclopedia of Sustainability Science and Technology, Second Edition (2019) 195-234.
11.   N. G. Moreno, M. C. Molina, D. Gervasio and J. F. P. Robles, Renewable and Sustainable Energy Reviews 52 (2015) 897-906.
12.   M. Çögenli, S. Mukerjee and A. B. Yurtcan, Fuel Cells 15 (2015) 288-297.
13.   C. D. Cooper, J. J. Burk, C. P. Taylor and S. K. Buratto, Journal of Applied Electrochemistry 47 (2017) 699-709.
14.   A. Kongkanand, N. P. Subramanian, Y. Yu, Z. Liu, H. Igarashi and D. A. Muller, ACS Catalysis 6 (2016) 1578-1583.
15.   S. Sui, X. Wang, X. Zhou, Y. Su, S. Riffat and C.-j. Liu, Journal of Materials Chemistry A 5 (2017) 1808-1825.
16.   C. W. Bezerra, L. Zhang, K. Lee, H. Liu, A. L. Marques, E. P. Marques, H. Wang and J. Zhang, Electrochimica Acta 53 (2008) 4937-4951.
17.   J. Wu, X. Z. Yuan, J. J. Martin, H. Wang, J. Zhang, J. Shen, S. Wu and W. Merida, Journal of Power Sources 184 (2008) 104-119.
18.   L. Zhang, J. Zhang, D. P. Wilkinson and H. Wang, Journal of Power Sources 156 (2006) 171-182.
19.   B. Millington, V. Whipple and B. G. Pollet, Journal of Power Sources 196 (2011) 8500-8508.
20.   A. Schenk, C. Grimmer, M. Perchthaler, S. Weinberger, B. Pichler, C. Heinzl, C. Scheu, F.-A. Mautner, B. Bitschnau and V. Hacker, Journal of power sources 266 (2014) 313-322.
21.   S. T. Thompson, A. R. Wilson, P. Zelenay, D. J. Myers, K. L. More, K. Neyerlin and D. Papageorgopoulos, Solid State Ionics 319 (2018) 68-76.
22.   G. Wu, Frontiers in Energy 11 (2017) 286-298.
23.   D. Banham, T. Kishimoto, Y. Zhou, T. Sato, K. Bai, J.-i. Ozaki, Y. Imashiro and S. Ye, Science advances 4 (2018) eaar7180.
24.   R. Jasinski, Nature 201 (1964) 1212-1213.
25.   Y. Nie, L. Li and Z. Wei, Chemical Society Reviews 44 (2015) 2168-2201.

26. E. Proietti, F. Jaouen, M. Lefèvre, N. Larouche, J. Tian, J. Herranz and J.-P. Dodelet, Nature communications 2 (2011) 416.

27. C. Fabjan, G. Frithum and H. Hartl, Berichte der Bunsengesellschaft für physikalische Chemie 94 (1990) 937-941.

28. S. Gupta, D. Tryk, I. Bae, W. Aldred and E. Yeager, Journal of applied electrochemistry 19 (1989) 19-27.

29. D. Ohms, S. Herzog, R. Franke, V. Neumann, K. Wiesener, S. Gamburcev, A. Kaisheva and I. Iliev, Journal of power sources 38 (1992) 327-334.

30. M. M. Hossen, K. Artyushkova, P. Atanassov and A. Serov, Journal of Power Sources 375 (2018) 214-221.

31. T. Palaniselvam, B. P. Biswal, R. Banerjee and S. Kurungot, Chemistry–A European Journal 19 (2013) 9335-9342.

32. M. Shao, Q. Chang, J.-P. Dodelet and R. Chenitz, Chemical reviews 116 (2016) 3594-3657.

33. Z. Zhang, J. Sun, M. Dou, J. Ji and F. Wang, ACS applied materials & interfaces 9 (2017) 16236-16242.

34. R. Li, Z. Wei and X. Gou, Acs Catalysis 5 (2015) 4133-4142.

35. S.-A. Wohlgemuth, R. J. White, M.-G. Willinger, M.-M. Titirici and M. Antonietti, Green Chemistry 14 (2012) 1515-1523.

36. L. Yang, S. Jiang, Y. Zhao, L. Zhu, S. Chen, X. Wang, Q. Wu, J. Ma, Y. Ma and Z. Hu, Angewandte Chemie International Edition 50 (2011) 7132-7135.

37. D.-S. Yang, D. Bhattacharjya, S. Inamdar, J. Park and J.-S. Yu, Journal of the American Chemical Society 134 (2012) 16127-16130.

38. X. Fu, P. Zamani, J. Y. Choi, F. M. Hassan, G. Jiang, D. C. Higgins, Y. Zhang, M. A. Hoque and Z. Chen, Advanced Materials 29 (2017) 1604456.

39. X. Fu, N. Li, B. Ren, G. Jiang, Y. Liu, F. M. Hassan, D. Su, J. Zhu, L. Yang and Z. Bai, Advanced Energy Materials 9 (2019) 1803737.

40. N. D. Leonard, S. Wagner, F. Luo, J. Steinberg, W. Ju, N. Weidler, H. Wang, U. I. Kramm and P. Strasser, ACS Catalysis 8 (2018) 1640-1647.

41. J. Marie, R. Chenitz, M. Chatenet, S. Berthon-Fabry, N. Cornet and P. Achard, Journal of Power Sources 190 (2009) 423-434.

42. H. Sun, H. Liu and L.-j. Guo, Journal of Power Sources 143 (2005) 125-135.

43. J. Zhang, Y. Tang, C. Song, X. Cheng, J. Zhang and H. Wang, Electrochimica Acta 52 (2007) 5095-5101.

44. J. Zhang, Y. Tang, C. Song, Z. Xia, H. Li, H. Wang and J. Zhang, Electrochimica Acta 53 (2008) 5315-5321.

45. Y. Sone, P. Ekdunge and D. Simonsson, Journal of the Electrochemical Society 143 (1996) 1254-1259.

46. J. Zhang, Y. Tang, C. Song, J. Zhang and H. Wang, Journal of power sources 163 (2006) 532-537.

47. F. Harnisch, S. Wirth and U. Schröder, Electrochemistry Communications 11 (2009) 2253-2256.

48. D. Banham and S. Ye, ACS Energy Letters 2 (2017) 629-638.

49. R. Cao, R. Thapa, H. Kim, X. Xu, M. G. Kim, Q. Li, N. Park, M. Liu and J. Cho, Nature communications 4 (2013) 2076.

50. Y. Jiang, Y. Lu, X. Lv, D. Han, Q. Zhang, L. Niu and W. Chen, Acs Catalysis 3 (2013) 1263-1271.
51. W. Li, A. Yu, D. C. Higgins, B. G. Llanos and Z. Chen, Journal of the American Chemical Society 132 (2010) 17056-17058.
52. C. Zhang, R. Hao, H. Yin, F. Liu and Y. Hou, Nanoscale 4 (2012) 7326-7329.
53. Y. Ma and P. B. Balbuena, Chemical physics letters 440 (2007) 130-133.
54. K. D. Miner, A. Mukherjee, Y. G. Gao, E. L. Null, I. D. Petrik, X. Zhao, N. Yeung, H. Robinson and Y. Lu, Angewandte Chemie International Edition 51 (2012) 5589-5592.
55. L. Que Jr and W. B. Tolman, Nature 455 (2008) 333.
56. L. Dos Santos, V. Climent, C. F. Blanford and F. A. Armstrong, Physical Chemistry Chemical Physics 12 (2010) 13962-13974.
57. M. Lai and A. Bergel, Journal of Electroanalytical Chemistry 494 (2000) 30-40.
58. N. Mano, V. Soukharev and A. Heller, The Journal of Physical Chemistry B 110 (2006) 11180-11187.
59. Z. Chen, D. Higgins, A. Yu, L. Zhang and J. Zhang, Energy & Environmental Science 4 (2011) 3167-3192.
60. M. Lefèvre, J. Dodelet and P. Bertrand, The Journal of Physical Chemistry B 106 (2002) 8705-8713.
61. H. A. Gasteiger and N. M. Marković, science 324 (2009) 48-49.
62. M. Lefèvre, E. Proietti, F. Jaouen and J.-P. Dodelet, science 324 (2009) 71-74.
63. U. I. Kramm, J. Herranz, N. Larouche, T. M. Arruda, M. Lefevre, F. Jaouen, P. Bogdanoff, S. Fiechter, I. Abs-Wurmbach and S. Mukerjee, Physical Chemistry Chemical Physics 14 (2012) 11673-11688.
64. C. E. Szakacs, M. Lefèvre, U. I. Kramm, J.-P. Dodelet and F. Vidal, Physical Chemistry Chemical Physics 16 (2014) 13654-13661.
65. H. T. Chung, D. A. Cullen, D. Higgins, B. T. Sneed, E. F. Holby, K. L. More and P. Zelenay, Science 357 (2017) 479-484.
66. D. Deng, L. Yu, X. Chen, G. Wang, L. Jin, X. Pan, J. Deng, G. Sun and X. Bao, Angewandte Chemie International Edition 52 (2013) 371-375.
67. U. Tylus, Q. Jia, K. Strickland, N. Ramaswamy, A. Serov, P. Atanassov and S. Mukerjee, The Journal of Physical Chemistry C 118 (2014) 8999-9008.
68. Y. Hu, J. O. Jensen, W. Zhang, L. N. Cleemann, W. Xing, N. J. Bjerrum and Q. Li, Angewandte Chemie International Edition 53 (2014) 3675-3679.
69. J. Wang, Z. Huang, W. Liu, C. Chang, H. Tang, Z. Li, W. Chen, C. Jia, T. Yao, S. Wei, Y. Wu and Y. Li, Journal of the American Chemical Society 139 (2017) 17281-17284.
70. J. Herranz, F. Jaouen, M. Lefèvre, U. I. Kramm, E. Proietti, J.-P. Dodelet, P. Bogdanoff, S. Fiechter, I. Abs-Wurmbach and P. Bertrand, The Journal of Physical Chemistry C 115 (2011) 16087-16097.
71. R. Chenitz, U. I. Kramm, M. Lefèvre, V. Glibin, G. Zhang, S. Sun and J.-P. Dodelet, Energy & Environmental Science 11 (2018) 365-382.
72. C. H. Choi, H.-K. Lim, M. W. Chung, G. Chon, N. R. Sahraie, A. Altin, M.-T. Sougrati, L. Stievano, H. S. Oh and E. S. Park, Energy & Environmental Science 11 (2018) 3176-3182.
73. G. Liu, X. Li and B. Popov, ECS Transactions 25 (2009) 1251-1259.
74. R. Borup, J. Meyers, B. Pivovar, Y. S. Kim, R. Mukundan, N. Garland, D. Myers, M. Wilson, F. Garzon and D. Wood, Chemical reviews 107 (2007) 3904-3951.

75. M. Cai, M. S. Ruthkosky, B. Merzougui, S. Swathirajan, M. P. Balogh and S. H. Oh, Journal of Power Sources 160 (2006) 977-986.
76. M. F. Mathias, R. Makharia, H. A. Gasteiger, J. J. Conley, T. J. Fuller, C. J. Gittleman, S. S. Kocha, D. P. Miller, C. K. Mittelsteadt and T. Xie, Interface-Electrochemical Society 14 (2005) 24-36.
77. D. E. Curtin, R. D. Lousenberg, T. J. Henry, P. C. Tangeman and M. E. Tisack, Journal of power Sources 131 (2004) 41-48.
78. S. Hommura, K. Kawahara and T. Shimodaira, Polym. Prep. Jpn 54 (2005) 4517-4518.
79. H. Schulenburg, S. Stankov, V. Schünemann, J. Radnik, I. Dorbandt, S. Fiechter, P. Bogdanoff and H. Tributsch, The Journal of Physical Chemistry B 107 (2003) 9034-9041.
80. N. Ramaswamy, U. Tylus, Q. Jia and S. Mukerjee, Journal of the American Chemical Society 135 (2013) 15443-15449.
81. M. Lefèvre and J.-P. Dodelet, Electrochimica Acta 48 (2003) 2749-2760.
82. A. Van Der Putten, A. Elzing, W. Visscher and E. Barendrecht, Journal of electroanalytical chemistry and interfacial electrochemistry 205 (1986) 233-244.
83. J. Wang, Z. Huang, W. Liu, C. Chang, H. Tang, Z. Li, W. Chen, C. Jia, T. Yao and S. Wei, Journal of the American Chemical Society 139 (2017) 17281-17284.
84. H. Zhang, S. Hwang, M. Wang, Z. Feng, S. Karakalos, L. Luo, Z. Qiao, X. Xie, C. Wang and D. Su, Journal of the American Chemical Society 139 (2017) 14143-14149.
85. Q. Fan and S. Le, *Journal*, 2003.
86. T.-H. Huang, H.-L. Shen, T.-C. Jao, F.-B. Weng and A. Su, international journal of hydrogen energy 37 (2012) 13872-13879.
87. X. Leimin, L. Shijun, Y. Lijun and L. Zhenxing, Fuel Cells 9 (2009) 101-105.
88. A. Therdthianwong, P. Ekdharmasuit and S. Therdthianwong, Energy & Fuels 24 (2010) 1191-1196.
89. J. I. Goldstein, D. E. Newbury, J. R. Michael, N. W. Ritchie, J. H. J. Scott and D. C. Joy, *Scanning electron microscopy and X-ray microanalysis*, Springer, 2017.
90. https://bio.libretexts.org/Bookshelves/Microbiology/Book%3A_Microbiology_(Bruslind)/02%3A_Microscopes.
91. D. B. Williams and C. B. Carter, in *Transmission electron microscopy*, Springer, 1996, pp. 3-17.
92. L. Reimer, *Transmission electron microscopy: physics of image formation and microanalysis*, Springer, 2013.
93. B. E. Warren, *X-ray Diffraction*, Courier Corporation, 1990.
94. P. Ehrhart, Journal of nuclear materials 216 (1994) 170-198.
95. H. Konno, in *Materials Science and Engineering of Carbon*, Elsevier, 2016, pp. 153-171.
96. Y. Bing, H. Liu, L. Zhang, D. Ghosh and J. Zhang, Chemical Society Reviews 39 (2010) 2184-2202.
97. W. R. W. Daud, R. Rosli, E. Majlan, S. Hamid, R. Mohamed and T. Husaini, Renewable Energy 113 (2017) 620-638.
98. A. de Frank Bruijn and G. J. Janssen, in *Fuel Cells*, Springer, 2013, pp. 249-303.
99. J. W. Choi and D. Aurbach, Nature Reviews Materials 1 (2016) 16013.
100. S. W. Kim, D. H. Seo, X. Ma, G. Ceder and K. Kang, Advanced Energy Materials 2 (2012) 710-721.

101. H. Wu and Y. Cui, Nano today 7 (2012) 414-429.
102. Z. Chen, A. Yu, D. Higgins, H. Li, H. Wang and Z. Chen, Nano letters 12 (2012) 1946-1952.
103. W. G. Hardin, D. A. Slanac, X. Wang, S. Dai, K. P. Johnston and K. J. Stevenson, The journal of physical chemistry letters 4 (2013) 1254-1259.
104. D. U. Lee, P. Xu, Z. P. Cano, A. G. Kashkooli, M. G. Park and Z. Chen, Journal of Materials Chemistry A 4 (2016) 7107-7134.
105. L. Ma, H. Zhuang, Y. Lu, S. S. Moganty, R. G. Hennig and L. A. Archer, Advanced Energy Materials 4 (2014) 1400390.
106. S. Wei, L. Ma, K. E. Hendrickson, Z. Tu and L. A. Archer, Journal of the American Chemical Society 137 (2015) 12143-12152.
107. G. Xu, B. Ding, L. Shen, P. Nie, J. Han and X. Zhang, Journal of Materials Chemistry A 1 (2013) 4490-4496.
108. B. Huskinson, M. P. Marshak, C. Suh, S. Er, M. R. Gerhardt, C. J. Galvin, X. Chen, A. Aspuru-Guzik, R. G. Gordon and M. J. Aziz, Nature 505 (2014) 195.
109. T. Janoschka, N. Martin, U. Martin, C. Friebe, S. Morgenstern, H. Hiller, M. D. Hager and U. S. Schubert, Nature 527 (2015) 78.
110. J. Zhang, G. Jiang, P. Xu, A. G. Kashkooli, M. Mousavi, A. Yu and Z. Chen, Energy & Environmental Science 11 (2018) 2010-2015.
111. D. Guo, R. Shibuya, C. Akiba, S. Saji, T. Kondo and J. Nakamura, Science 351 (2016) 361-365.
112. J. Zhang, Z. Zhao, Z. Xia and L. Dai, Nature nanotechnology 10 (2015) 444.
113. L. Dai, Y. Xue, L. Qu, H.-J. Choi and J.-B. Baek, Chemical reviews 115 (2015) 4823-4892.
114. U. I. Koslowski, I. Abs-Wurmbach, S. Fiechter and P. Bogdanoff, The Journal of Physical Chemistry C 112 (2008) 15356-15366.
115. J. Tian, A. Morozan, M. T. Sougrati, M. Lefèvre, R. Chenitz, J. P. Dodelet, D. Jones and F. Jaouen, Angewandte Chemie International Edition 52 (2013) 6867-6870.
116. P. H. Matter, L. Zhang and U. S. Ozkan, Journal of Catalysis 239 (2006) 83-96.
117. L. Qu, Y. Liu, J.-B. Baek and L. Dai, ACS nano 4 (2010) 1321-1326.
118. R. Jasinski, Journal of the Electrochemical Society 112 (1965) 526-528.
119. M.-Q. Wang, W.-H. Yang, H.-H. Wang, C. Chen, Z.-Y. Zhou and S.-G. Sun, Acs Catalysis 4 (2014) 3928-3936.
120. Y. Ye, H. Li, F. Cai, C. Yan, R. Si, S. Miao, Y. Li, G. Wang and X. Bao, ACS Catalysis 7 (2017) 7638-7646.
121. Y. Zhao, K. Watanabe and K. Hashimoto, Journal of the American Chemical Society 134 (2012) 19528-19531.
122. S. Gao, L. Li, K. Geng, X. Wei and S. Zhang, Nano Energy 16 (2015) 408-418.
123. Z. Lu, J. Wang, S. Huang, Y. Hou, Y. Li, Y. Zhao, S. Mu, J. Zhang and Y. Zhao, Nano Energy 42 (2017) 334-340.
124. J. Liang, Y. Jiao, M. Jaroniec and S. Z. Qiao, Angewandte Chemie International Edition 51 (2012) 11496-11500.
125. S. Ikeda, S. Ishino, T. Harada, N. Okamoto, T. Sakata, H. Mori, S. Kuwabata, T. Torimoto and M. Matsumura, Angewandte Chemie International Edition 45 (2006) 7063-7066.

126.   C. Zhou, J. Han, G. Song and R. Guo, Journal of Polymer Science Part A: Polymer Chemistry 46 (2008) 3563-3572.
127.   M. Sevilla and R. Mokaya, Energy & Environmental Science 7 (2014) 1250-1280.
128.   C. Zhang, R. Hao, H. Liao and Y. Hou, Nano Energy 2 (2013) 88-97.
129.   Z. Wang, Y. Dong, H. Li, Z. Zhao, H. B. Wu, C. Hao, S. Liu, J. Qiu and X. W. D. Lou, Nature communications 5 (2014) 5002.
130.   P. Ganesan, M. Prabu, J. Sanetuntikul and S. Shanmugam, ACS catalysis 5 (2015) 3625-3637.
131.   M. Ferrandon, A. J. Kropf, D. J. Myers, K. Artyushkova, U. Kramm, P. Bogdanoff, G. Wu, C. M. Johnston and P. Zelenay, The Journal of Physical Chemistry C 116 (2012) 16001-16013.
132.   L. Lin, Q. Zhu and A.-W. Xu, Journal of the American Chemical Society 136 (2014) 11027-11033.
133.   H. T. Chung, J. H. Won and P. Zelenay, Nature communications 4 (2013) 1922.
134.   K. Wan, Z.-p. Yu, X.-h. Li, M.-y. Liu, G. Yang, J.-h. Piao and Z.-x. Liang, ACS Catalysis 5 (2015) 4325-4332.
135.   J. Herranz, F. Jaouen, M. Lefèvre, U. I. Kramm, E. Proietti, J.-P. Dodelet, P. Bogdanoff, S. Fiechter, I. Abs-Wurmbach, P. Bertrand, T. M. Arruda and S. Mukerjee, The Journal of Physical Chemistry C 115 (2011) 16087-16097.
136.   A. C. Fernandes and E. A. Ticianelli, Journal of Power Sources 193 (2009) 547-554.
137.   H. Li, K. Tsay, H. Wang, J. Shen, S. Wu, J. Zhang, N. Jia, S. Wessel, R. Abouatallah, N. Joos and J. Schrooten, Journal of Power Sources 195 (2010) 8089-8093.
138.   G. Zhang, R. Chenitz, M. Lefèvre, S. Sun and J.-P. Dodelet, Nano Energy 29 (2016) 111-125.
139.   E. Antolini, T. Lopes and E. R. Gonzalez, Journal of Alloys and Compounds 461 (2008) 253-262.
140.   X. Wang, J. S. Lee, Q. Zhu, J. Liu, Y. Wang and S. Dai, Chemistry of Materials 22 (2010) 2178-2180.
141.   V. J. Watson, C. Nieto Delgado and B. E. Logan, Journal of Power Sources 242 (2013) 756-761.
142.   U. I. Kramm, I. Herrmann-Geppert, P. Bogdanoff and S. Fiechter, The Journal of Physical Chemistry C 115 (2011) 23417-23427.
143.   H. Deng, Q. Li, J. Liu and F. Wang, Carbon 112 (2017) 219-229.
144.   N. Gavrilov, I. A. Pašti, M. Mitrić, J. Travas-Sejdić, G. Ćirić-Marjanović and S. V. Mentus, Journal of Power Sources 220 (2012) 306-316.
145.   G. Wu, K. L. More, C. M. Johnston and P. Zelenay, Science 332 (2011) 443.
146.   Z. Lin, G. Waller, Y. Liu, M. Liu and C.-P. Wong, Advanced Energy Materials 2 (2012) 884-888.
147.   S. Wakeland, R. Martinez, J. K. Grey and C. C. Luhrs, Carbon 48 (2010) 3463-3470.
148.   S. D. Yim, S. J. Kim, J. H. Baik, I. S. Nam, Y. S. Mok, J.-H. Lee, B. K. Cho and S. H. Oh, Industrial & Engineering Chemistry Research 43 (2004) 4856-4863.
149.   R. Cao, R. Thapa, H. Kim, X. Xu, M. Gyu Kim, Q. Li, N. Park, M. Liu and J. Cho, Nature Communications 4 (2013) 2076.
150.   Y. Chen, S. Ji, Y. Wang, J. Dong, W. Chen, Z. Li, R. Shen, L. Zheng, Z. Zhuang, D. Wang and Y. Li, Angewandte Chemie International Edition 56 (2017) 6937-6941.

151. X. Cui, S. Yang, X. Yan, J. Leng, S. Shuang, P. M. Ajayan and Z. Zhang, Advanced Functional Materials 26 (2016) 5708-5717.
152. C. H. Choi, S. H. Park and S. I. Woo, ACS Nano 6 (2012) 7084-7091.
153. C. H. Choi, S. H. Park and S. I. Woo, Journal of Materials Chemistry 22 (2012) 12107-12115.
154. S. Wang , E. Iyyamperumal , A. Roy, Y. Xue, D. Yu and L. Dai, Angewandte Chemie International Edition 50 (2011) 11756-11760.
155. C. Zhang, N. Mahmood, H. Yin, F. Liu and Y. Hou, Advanced Materials 25 (2013) 4932-4937.
156. H. T. Chung, C. M. Johnston, K. Artyushkova, M. Ferrandon, D. J. Myers and P. Zelenay, Electrochemistry Communications 12 (2010) 1792-1795.
157. G. Liu, X. Li, P. Ganesan and B. N. Popov, Electrochimica Acta 55 (2010) 2853-2858.
158. B. Wang, Journal of Power Sources 152 (2005) 1-15.
159. G.-L. Chai, Z. Hou, D.-J. Shu, T. Ikeda and K. Terakura, Journal of the American Chemical Society 136 (2014) 13629-13640.
160. C. Tang and Q. Zhang, Advanced Materials 29 (2017) 1604103.
161. H. Zhao, C. Sun, Z. Jin, D.-W. Wang, X. Yan, Z. Chen, G. Zhu and X. Yao, Journal of Materials Chemistry A 3 (2015) 11736-11739.
162. B. J. Kim, D. U. Lee, J. Wu, D. Higgins, A. Yu and Z. Chen, The Journal of Physical Chemistry C 117 (2013) 26501-26508.
163. T. C. Nagaiah, S. Kundu, M. Bron, M. Muhler and W. Schuhmann, Electrochemistry Communications 12 (2010) 338-341.
164. L. T. Soo, K. S. Loh, A. B. Mohamad, W. R. W. Daud and W. Y. Wong, Journal of Alloys and Compounds 677 (2016) 112-120.
165. J. Wang, R. Ma, Y. Zhou and Q. Liu, Journal of Materials Chemistry A 3 (2015) 12836-12844.
166. X. Cui, S. Yang, X. Yan, J. Leng, S. Shuang, P. M. Ajayan and Z. Zhang, Advanced Functional Materials 26 (2016) 5708-5717.
167. P.-A. Pascone, D. Berk and J.-L. Meunier, Catalysis today 211 (2013) 162-167.
168. S. Yasuda, A. Furuya, Y. Uchibori, J. Kim and K. Murakoshi, Advanced Functional Materials 26 (2016) 738-744.
169. Q. Dong, X. Zhuang, Z. Li, B. Li, B. Fang, C. Yang, H. Xie, F. Zhang and X. Feng, Journal of Materials Chemistry A 3 (2015) 7767-7772.
170. C. He, J. J. Zhang and P. K. Shen, Journal of Materials Chemistry A 2 (2014) 3231-3236.
171. Y. Li, L. Yuan, Z. Li, Y. Qi, C. Wu, J. Liu and Y. Huang, RSC Advances 5 (2015) 44160-44164.
172. S. Banerjee and D. E. Curtin, Journal of fluorine chemistry 125 (2004) 1211-1216.
173. C. Heitner-Wirguin, Journal of membrane Science 120 (1996) 1-33.
174. J. A. Kerres, Journal of Membrane Science 185 (2001) 3-27.
175. M. Saito, K. Hayamizu and T. Okada, The Journal of Physical Chemistry B 109 (2005) 3112-3119.
176. K. Kreuer, Journal of membrane science 185 (2001) 29-39.
177. D. Wu, S. J. Paddison, J. A. Elliott and S. J. Hamrock, Langmuir 26 (2010) 14308-14315.
178. J. Ge, A. Higier and H. Liu, Journal of Power Sources 159 (2006) 922-927.
179. V. A. Sethuraman, J. W. Weidner, A. T. Haug, S. Motupally and L. V. Protsailo, Journal of The Electrochemical Society 155 (2008) B50-B57.

180. M. Boillot, C. Bonnet, N. Jatroudakis, P. Carre, S. Didierjean and F. Lapicque, Fuel Cells 6 (2006) 31-37.
181. D. Natarajan and T. Van Nguyen, Journal of power sources 115 (2003) 66-80.
182. L. Wang, A. Husar, T. Zhou and H. Liu, International journal of hydrogen energy 28 (2003) 1263-1272.
183. S. Kim, S. Shimpalee and J. Van Zee, Journal of Power Sources 135 (2004) 110-121.
184. S. Qu, X. Li, M. Hou, Z. Shao and B. Yi, Journal of Power Sources 185 (2008) 302-310.
185. Y. Shan and S.-Y. Choe, Journal of power sources 145 (2005) 30-39.
186. Y. Shan and S.-Y. Choe, Journal of Power Sources 158 (2006) 274-286.
187. Z. Belkhiri, M. Zeroual, H. B. Moussa and B. Zitouni, Revue des Energies Renouvelables 14 (2011) 121-130.
188. D. N. Ozen, B. Timurkutluk and K. Altinisik, Renewable and Sustainable Energy Reviews 59 (2016) 1298-1306.
189. K. D. Kreuer, M. Schuster, B. Obliers, O. Diat, U. Traub, A. Fuchs, U. Klock, S. J. Paddison and J. Maier, Journal of Power Sources 178 (2008) 499-509.
190. A. M. Pivovar and B. S. Pivovar, The Journal of Physical Chemistry B 109 (2005) 785-793.
191. E. Aleksandrova, R. Hiesgen, D. Eberhard, K. A. Friedrich, T. Kaz and E. Roduner, ChemPhysChem 8 (2007) 519-522.
192. N. Djilali, Energy 32 (2007) 269-280.
193. H. Li, Y. Tang, Z. Wang, Z. Shi, S. Wu, D. Song, J. Zhang, K. Fatih, J. Zhang, H. Wang, Z. Liu, R. Abouatallah and A. Mazza, Journal of Power Sources 178 (2008) 103-117.
194. Z. Qi and A. Kaufman, Journal of Power Sources 109 (2002) 38-46.
195. J. Baschuk and X. Li, Journal of power sources 86 (2000) 181-196.
196. F. Barbir, H. Gorgun and X. Wang, Journal of Power Sources 141 (2005) 96-101.
197. S. Shimpalee, S. Greenway and J. Van Zee, Journal of Power Sources 160 (2006) 398-406.
198. J. Scholta, G. Escher, W. Zhang, L. Küppers, L. Jörissen and W. Lehnert, Journal of Power Sources 155 (2006) 66-71.
199. G. Zhang, Q. Wei, X. Yang, A. C. Tavares and S. Sun, Applied Catalysis B: Environmental 206 (2017) 115-126.
200. A. Bonakdarpour, M. Lefevre, R. Yang, F. Jaouen, T. Dahn, J.-P. Dodelet and J. Dahn, Electrochemical and Solid-State Letters 11 (2008) B105-B108.
201. W. Wong, W. R. W. Daud, A. B. Mohamad, A. A. H. Kadhum, K. S. Loh, E. Majlan and K. L. Lim, Electrochimica Acta 129 (2014) 47-54.
202. D. Lee and S. Hwang, International Journal of Hydrogen Energy 33 (2008) 2790-2794.
203. G. Sasikumar, J. Ihm and H. Ryu, Electrochimica Acta 50 (2004) 601-605.
204. D. S. Hwang, C. H. Park, S. C. Yi and Y. M. Lee, International Journal of Hydrogen Energy 36 (2011) 9876-9885.
205. A. Suzuki, U. Sen, T. Hattori, R. Miura, R. Nagumo, H. Tsuboi, N. Hatakeyama, A. Endou, H. Takaba and M. C. Williams, International Journal of Hydrogen Energy 36 (2011) 2221-2229.
206. Y. Liu, C. Ji, W. Gu, D. R. Baker, J. Jorne and H. A. Gasteiger, Journal of The Electrochemical Society 157 (2010) B1154-B1162.
207. M. S. Schaberg, J. E. Abulu, G. M. Haugen, M. A. Emery, S. J. O'Conner, P. N. Xiong and S. Hamrock, ECS Transactions 33 (2010) 627-633.

208. Y. Liu, C. Ji, D. Baker, W. Gu, J. Jorne and H. Gasteiger, ECS Transactions 16 (2008) 1775-1786.
209. J. Sumner, S. Creager, J. Ma and D. DesMarteau, Journal of the Electrochemical Society 145 (1998) 107-110.
210. S.-Y. Ahn, Y.-C. Lee, H. Y. Ha, S.-A. Hong and I.-H. Oh, Electrochimica Acta 50 (2004) 673-676.
211. H. Gasteiger and S. Yan, Journal of power sources 127 (2004) 162-171.
212. I. Gatto, A. Stassi, V. Baglio, A. Carbone, E. Passalacqua, A. Aricò, M. Schuster and B. Bauer, Electrochimica Acta 165 (2015) 450-455.
213. M. N. Tsampas, A. Pikos, S. Brosda, A. Katsaounis and C. G. Vayenas, Electrochimica Acta 51 (2006) 2743-2755.
214. H. Wu, P. Berg and X. Li, Journal of Power Sources 165 (2007) 232-243.
215. A. Bazylak, International journal of hydrogen energy 34 (2009) 3845-3857.
216. D. Banham, S. Ye, K. Pei, J.-i. Ozaki, T. Kishimoto and Y. Imashiro, Journal of Power Sources 285 (2015) 334-348.
217. C. W. Bezerra, L. Zhang, H. Liu, K. Lee, A. L. Marques, E. P. Marques, H. Wang and J. Zhang, Journal of Power Sources 173 (2007) 891-908.
218. J. Shui, M. Wang, F. Du and L. Dai, Science advances 1 (2015) e1400129.
219. https://www.greencarcongress.com/2014/06/20140625-fcv.html.